MOLECULAR ROTORS: APPLICATIONS FOR MEASURING CELLULAR PHYSICAL PROPERTIES

by

CHARLES MCRAE WHITE

(Under the Direction of William S. Kisaalita)

ABSTRACT

This study has been carried out to explore the potential cell culture applications for molecular rotors, a family of fluorescent molecules with the ability to undergo intramolecular rotation upon photoexcitation. The relationship between intramolecular rotation and fluorescence quantum yield is proportional to environmental free volume, which can be related to viscosity. New insights into the biomechanical properties of cells, which includes plasma membrane viscosity, are revealing the importance of these properties and how they relate to cell state and disease. *Membrane viscosity* describes the ease of movement within the phospholipid bilayer, and directly influences physiological properties such as membrane-bound enzyme activity, carrier-mediated transport, and membrane-bound receptor binding. Many methods exist that directly or indirectly report membrane physical properties, but these methods are time-consuming and of limited spatial resolution. Molecular rotors are ideally suited for characterizing membrane viscosity because of their excellent spatial and temporal response. We have synthesized and characterized a ratiometric family of molecular rotors for this purpose. Human fibroblast cells are grown on polyacrylamide gels to induce changes in cell mechanics, which is verified by atomic force microscopy. Molecular rotors are applied to explore the relationship between cell stiffness and membrane viscosity. Another objective was to establish molecular rotors as a tool for measuring membrane viscosity in cells grown as 3D cultures. We design and fabricate a custom 3D culture platform for this purpose. To optimize these efforts, we have customized a Nikon PCM 2000 confocal microscope system for the purpose of imaging the ratiometric molecular rotor emission.

INDEX WORDS: Cell Culture, Fluorescence Imaging, Molecular Rotors, Membrane Viscosity, Confocal Microscopy

MOLECULAR ROTORS: APPLICATIONS FOR MEASURING CELLULAR PHYSICAL PROPERTIES

by

CHARLES MCRAE WHITE

B.S., Rose-Hulman Institute of Technology, 2013

A Dissertation Submitted to the Graduate Faculty of The University of Georgia in Partial Fulfillment of the Requirements for the Degree

DOCTOR OF PHILOSOPHY

Athens, Georgia

2020

MOLECULAR ROTORS: APPLICATIONS FOR MEASURING CELLULAR PHYSICAL PROPERTIES

by

CHARLES MCRAE WHITE

Major Professor:	William Kisaalita
Committee:	Eric Freeman Mark Haidekker Hitesh Handa

Electronic Version Approved:

Ron Walcott
Interim Dean of the Graduate School
The University of Georgia
May 2020

DEDICATION

To Rachel, my wife, and Chuck and Jeanne, my parents, who have always encouraged me to pursue my interests. They have provided endless support and inspiration throughout this journey.

ACKNOWLEDGEMENTS

First, I owe thanks to my advisor, Dr. William Kisaalita, for his invaluable guidance, patience and generosity. He serves as an amazing role model for not only my graduate studies and professional development, but everyday life. His passion for being a mentor and teacher, his commitment to helping others, and his dedication to family and friends has been nothing short of inspirational. I consider myself lucky to have him as a mentor and friend.

I would like to acknowledge Dr. Eric Freeman, Dr. Mark Haidekker, and Dr. Hitesh Handa for serving in my dissertation committee. Their guidance and support have been essential to my professional development and the completion of my work.

Special thanks to Dr. Cheryl Gomillion and Jamie Barber for their incredible generosity, without which my research would not have been possible.

To Dr. Amish Asthana, Dr. Kenneth Ndyabawe, and Megan Douglass; thank you for your collaboration and friendship. From late nights to packing up and moving the lab, it was always a pleasure talking and working with you.

Finally, to my family and friends, thank you for your love and support, and to my wife Rachel, for her endless optimism and encouragement.

TABLE OF CONTENTS

Page

CHAPTER

LIST OF FIGURES

LIST OF TABLES

CHAPTER 1

INTRODUCTION AND OBJECTIVES

It is now well-established that by mimicking the *in vivo* microenvironment of cells, three-dimensional (3D) platforms support more physiologically relevant cell cultures when compared to cells grown on flat, two-dimensional (2D) substrates [1], which make them ideal for many applications, such as live cell assays used in drug discovery. One relevant example are cultured SH-SY5Y neuroblastoma cells, where voltage-gated calcium channel activation via high potassium depolarization yields a smaller intracellular calcium transient signal in comparison to 2D cultures of the same line [2, 3]. Although numerous studies have shown that a more physiologically relevant cell culture provides more physiologically relevant drug responses, 2D cell culture, either on glass or polystyrene, remains the gold standard for the pharmaceutical industry. It has been hypothesized that the microenvironmental factors that influence cells on all levels can be put into four groups [4, 5], one group being biophysical cues from neighboring cells and the surrounding cellular matrix.

Mechanotransduction, the process through which cells convert mechanical stimuli into biochemical responses, can be both an active and/or passive process. Cells use their adhesive and contractile molecular machinery to transmit forces to their surroundings, then transduce those forces to biochemical signals. As a result, the biomechanical properties of cells, which play an intricate role in determining biological function [6-8], change to maintain a mechanical equilibrium with the microenvironment [9]. Thus, the biomechanical properties of cells, and the influence the biophysical microenvironment has on these properties, has become an important topic for cell culture research.

Numerous methods have been developed to measure cell biomechanical properties, but these approaches have important limitations. Namely, these methods either require contact with the cell of interest or lack appropriate resolution in 3D applications. In the context of SH-SY5Y cells expressing different calcium signal profiles in 2D culture versus 3D, it was hypothesized that the cell membrane is stretched more tautly in a monolayer (2D) culture when compared to 3D [2, 3]. Building on past research in developing fluorescent molecular rotors, we propose using these nanoviscometer probes to “fill the gap” where other methods to measure cell biomechanical properties fail. The following specific objectives have been conceptualized to achieve this goal.

Objective One: This objective presents a custom 3D culture platform developed for the purpose of testing whether molecular rotors can be used to measure membrane viscosity in 3D cultures. Such a tool may provide information about cell biomechanical properties where other methods fail.

Objective Two: Use a model cell line, MRC-5 human lung fibroblasts, and polyacrylamide gels as a substrate to study the effects of different biophysical cues on membrane stretch, which will be related to changes in cell stiffness as measured by atomic force microscopy (AFM). Molecular rotors will be applied to cells growing on various polyacrylamide substrates and the fluorescence will be imaged using confocal microscopy. Image analysis will be performed using the Crystal Image software.

Objective Three: Conceptualize and implement modifications that enable confocal fluorescence imaging of dyes excitable by UV and visible light wavelengths. UV excitation will make viscosity imaging with UV excitable dual-emission ratiometric molecular rotors possible.

References:

1. Pampaloni, F., E.G. Reynaud, and E.H. Stelzer, The third dimension bridges the gap between cell culture and live tissue. Nature reviews Molecular cell biology, 2007. 8(10): p. 839-845.

2. Lai, Y., K. Cheng, and W. Kisaalita, Three dimensional neuronal cell cultures more accurately model voltage gated calcium channel functionality in freshly dissected nerve tissue. PLoS One, 2012. 7(9): p. e45074.

3. Wu, Z.Z., et al., Responsiveness of voltage-gated calcium channels in SH-SY5Y human neuroblastoma cells on quasi-three-dimensional micropatterns formed with poly (l-lactic acid). Int J Nanomedicine, 2013. 8: p. 93-107.

4. Asthana, A. and W.S. Kisaalita, Microtissue size and hypoxia in HTS with 3D cultures. Drug Discov Today, 2012. 17(15-16): p. 810-7.

5. Asthana, A. and W.S. Kisaalita, Is time an extra dimension in 3D cell culture? Drug discovery today, 2016. 21(3): p. 395-399.

6. Petridou, N.I., Z. Spiró, and C.-P. Heisenberg, Multiscale force sensing in development. Nature cell biology, 2017. 19(6): p. 581-588.

7. Van Helvert, S., C. Storm, and P. Friedl, Mechanoreciprocity in cell migration. Nature cell biology, 2018. 20(1): p. 8.

8. Mathieu, S. and J.-B. Manneville, Intracellular mechanics: connecting rheology and mechanotransduction. Current opinion in cell biology, 2019. 56: p. 34-44.

9. Solon, J., et al., Fibroblast adaptation and stiffness matching to soft elastic substrates. Biophys J, 2007. 93(12): p. 4453-61.

CHAPTER 2

LITERATURE REVIEW:

RATIOMETRIC NANOVISCOMETERS: APPLICATIONS FOR MEASURING CELLULAR PHYSICAL PROPERTIES IN 3D CULTURES[1]

---

[1] White, C. M., Haidekker, M. A., and Kisaalita, W. S. 2020. *SLAS Technology: Translating Life Sciences Innovation*.
Reprinted here with permission of the publisher.

2.1 Abstract

New insights into the biomechanical properties of cells are revealing the importance of these properties and how they relate to underlying molecular, architectural, and behavioral changes associated with cell-state and disease processes. However, the current understanding of how these in vitro biomechanical properties are associated with in vivo processes has been developed based on traditional monolayer (two-dimensional [2D]) cell culture, which traditionally has not translated well to three-dimensional (3D) cell culture and in vivo function. Many gold standard methods and tools used to observe the biomechanical properties on 2D cell culture cannot be used with 3D cell culture. Fluorescent molecules can respond to external factors almost instantaneously and require relatively low-cost instrumentation. In this review we provide background on fluorescent molecular rotors, which are attractive tools due to the relationship of their emission quantum yield with environmental microviscosity. We make the case for their use in both 2D and 3D cell culture and speculate on their fundamental and practical applications in cell biology.

2.2 Introduction

In 1971 Förster and Hoffmann proposed a theory based on the Debye-Stokes-Einstein microfriction concept that quantitatively explained the relationship between solvent microviscosity and emission quantum yield of dyes with the ability to perform intramolecular rotation [1]. At the same time, Rotkiewicz and Grabowsky proposed the hypothesis that 1,4-dimethylamino benzonitrile (DMABN) fluorescence is due to the existence of twisted intramolecular charge transfer (TICT) states [2], which provides a general model for a family of fluorescent molecules referred to as *molecular rotors*. Recently, these molecules have gained enormous popularity because of their ability to monitor polymerization processes [3], image flow patterns in microfluidic systems [4], and study cell physiology parameters [5, 6]. Implementation of molecular rotors into the plasma membrane of endothelial cells made it possible to demonstrate that increased fluid shear stress (FSS) increases membrane fluidity in the endothelial cell membrane [7]. Based on these observations, it was hypothesized that changes in membrane fluidity are the primary mechanism of mechanotransduction that converts the mechanical stimulus of FSS into the biochemical signals that have been associated with maintaining a specific level of flow or associated shear stress in blood vessels [7].

Recently, three-dimensional (3D) cell culture has gained significant attention, and it is now widely accepted that 3D in vitro platforms support more physiologically relevant cell cultures when compared to cells grown as a monolayer (two-dimensional [2D]) on a more traditional substrate. One relevant example involves SH-SY5Y neuroblastoma cells grown on a 3D platform, where voltage-gated calcium channel (VGCC) activation via high potassium depolarization yields a smaller intracellular calcium transient signal in comparison to 2D cultures of the same line [8, 9]. Kisaalita and colleagues hypothesized that the cell membrane plays a role in those observations as the membrane is thought to be stretched more tautly in a monolayer grown over a rigid 2D platform, opening invaginations in the membrane termed ‘caveolae’ and exposing more VGCCs to the extracellular environment. At the time, the tools to corroborate this hypothesis were not being explored for this application. Many methods exist that directly or indirectly report membrane physical properties, but these methods are time-consuming and of limited spatial resolution. Molecular rotors lend themselves to the notion of *viscosity imaging* because they require relatively simple steady-state fluorescence instrumentation, they report changes in real time, and their spatial resolution is only limited by the optical system.

We set the stage by first presenting molecular rotors and their potential for viscosity sensing at the single cell level. This is important given the current understanding of cell - cell physical microenvironment interaction. We review the state-of-the-art physical property measurement techniques and how these methods fall short in 3D culture settings - a gap molecular rotors are hypothesized to close. Finally, we suggest other potential practical applications of molecular rotors beyond viscosity imaging.

2.3 The physical principle of molecular rotors

Single emission molecular rotors

A typical molecular rotor consists of three subunits: an electron donor unit, an electron-rich spacer unit that is composed of a network of alternating single and double bonds, and an electron acceptor unit (Figure 1A). The spacer unit bring the donor and acceptor units in conjugation, thus facilitating the movement of an electron between the pair upon photoexcitation. Additionally, the spacer unit ensures minimum overlap of the donor and acceptor orbitals. The Jablonski diagram (Figure 1B, C) illustrates the different electronic states of a molecular rotor and the transitions between them. At the ground state (S_0), the molecule adopts a planar (or near planar) conformation, which is the lowest energetic conformation (Figure 1B, C). Upon photoexcitation at wavelength λ_{ex} the dye undergoes intramolecular charge transfer from the electron donor to acceptor unit, where the molecule reaches a planar locally-excited state S_1^{LE}. Due to an excited state charge separation, the molecule rapidly twists around a single σ-bond that connects the donor unit to the acceptor unit and assumes the lowest energy conformation of the excited state S_1^{TICT}.

For some fluorescent molecular rotors, including the most popular and well-explored molecular rotor, 1,4-dimethylamino benzonitrile (DMABN), relaxation from the twisted conformation to the planar ground state can occur through two channels, resulting in dual emission (Figure 1B) [10]. Molecular rotors that exhibit a single emission band λ_{em}^{LE}, such as farnesyl-(2-carboxy-2-cyanovinyl)-julolidine (FCVJ), have a very small $S_1^{TICT} – S_0^{TICT}$ energy gap and relaxation from the TICT conformation occurs without photon loss (from the S_1^{TICT} state to the S_0^{TICT} state) (Figure 1C). This category of molecular rotors attracts special interest because locally-excited (LE) emission is relatively insensitive against solvent polarity [11, 12].

While the reorientation relaxation of molecules in low-viscosity solution follows the Debye-Stokes-Einstein (DSE) hydrodynamic model with a stick boundary condition, Loufty and Arnold observed deviations from the model in medium- and high-viscosity solvents [13]. They accurately described the nonradiative decay rate (i.e., intramolecular rotation) k_R of molecular rotors and its relation to the molecular free-volume of these solvents through a free-volume concept

$$k_R = k_0 * exp\left(-x\,{}^{v_0}\!/_{v_f}\right) \qquad 1$$

where k_0 is the free-rotor reorientation rate, v_0 is the limiting specific volume of the solvent, v_f is the free volume, and x is a constant for the particular probe. In aggregates of macromolecules, which include the phospholipid bilayer, molecular free volume and viscosity are directly related. This relationship was experimentally provided by Doolittle [14] and given as

$$\eta = A * exp\left(B\frac{v_0}{v_f}\right) \qquad 2$$

where A and B are solvent-dependent constants (and B ≈ 1).

In solutions with low viscosity intramolecular rotation is the predominant deexcitation pathway, while intramolecular rotation is impeded in solutions with high viscosity [13, 15]. Furthermore, the fluorescence quantum yield from the planar excited state increases with increasing solvent viscosity [11]. By recognizing that intramolecular rotation and fluorescence emission are competing deactivation pathways (and thus an increase of k_R is associated with a lower quantum yield), substitution of the term ${}^{v_0}/_{v_f}$ with Equation 2 leads to a form very similar to the Förster-Hoffmann equation

$$\phi_F = \phi_0 * \left(\frac{\eta}{\sigma}\right)^x \tag{3}$$

where ϕ_0 is the dye's intrinsic quantum yield, σ is a dye-specific constant, and x depends on both the dye and solvent. This relationship holds over several magnitudes of viscosity.

Stretching of the cellular membrane, by FSS [7] for example, leads to a higher free volume and thus to a lower apparent viscosity. In fact, fluidity (the inverse of viscosity) has been used in the fluid mosaic model of the cell membrane [16] to explain many of the physiological responses of the cell membrane, notably the behavior of membrane-bound proteins. Although amended (e.g., [17, 18]), the fluid mosaic model is still widely accepted. In this respect, we believe that apparent viscosity (and, related, free volume) serves as a suitable proxy for the freedom of motion of individual phospholipids, membrane-bound proteins, and whole membrane partitions, such as lipid rafts. The same freedom of motion clearly applies to membrane-bound molecular rotors, which justifies their use as membrane viscosity sensors.

Molecular rotors with engineered dual emission

It is possible to invert Equation 3 and solve for the viscosity

$$\eta = \sigma \left({}^{\phi_F}/_{\phi_0}\right)^{1/x} \tag{4}$$

but the quantum yield is difficult to obtain. One can use time-resolved spectroscopy where fluorescence quantum yield ϕ_F and measured lifetime τ are directly related through

$$\phi_F = \frac{\tau}{\tau_N} \tag{5}$$

where τ_N is the fluorophore's natural lifetime (i.e., the lifetime where intramolecular rotation is inhibited and nonradiative deexcitation is absent). Lifetime measurements allows for the sequential calculation of a fluorophore's quantum yield and the microviscosity of the environment [19, 20]. However, several molecular rotors have a fluorescence lifetime in the range of 100 ps or less and show a low quantum yield in most solvents. Time-resolved spectroscopy and even fluorescent lifetime imaging (FLIM) depend on expensive equipment, and because the lifetime of many molecular rotors is below the nanosecond range, experiments using lifetime instrumentation can become complex. Steady-state instruments, like microscopes for steady-state fluorescence, are an attractive alternative because they are readily available in most research environments and are simple to use. This was the rationale for the development of self-calibrating dyes that provide an artificial reference [21-23], termed *ratiometric molecular rotors*. Although many TICT molecules exhibit dual emission (e.g., DMABN), the general design of a ratiometric molecular rotor comprises covalent linking of a reference fluorophore and a molecular rotor (Figure 2). The linked fluorophores form a resonance energy transfer (RET) pair which implies: a) the reference fluorophore emission spectrum has a significant overlap with the excitation spectrum of the molecular rotor and b) the two fluorophores are kept below the Förster radius, meaning that most of the reference fluorophore excited-state energy is transferred to the molecular rotor. This behavior is desirable because the reference fluorophore generally has a quantum yield near unity, while a typical molecular rotor shows viscosity-dependent quantum yield. More importantly, the high RET efficiency transfers most of the excited-state energy to the low quantum yield rotor, resulting in relatively balanced emission intensities.

The peak emission intensity I_{Rotor} of a molecular rotor with a low dye concentration c can be approximated as follows

$$I_{Rotor} = I_{ex} * G * c * \phi_F \qquad 6$$

where I_{ex} is the intensity of the excitation light and G is an instrument gain factor that reflects sensitivity, collection efficiency, and signal processing. The same equation is valid for the emission of the reference dye,

$$I_{ref} = I_{ex} * G * c * \phi_{ref} \qquad 7$$

where ϕ_{ref} is the quantum yield of the reference fluorophore where usually $\phi_{ref} \approx 1$. For fluorescence microscopy of thin layers, Equations 6 and 7 become spatially resolved:

$$I_{Rotor}(x,y) = I_{ex}(x,y) * G * \int_z c(x,y,z) * \phi_F(x,y,z)\ dz \qquad 8$$

$$I_{ref}(x,y) = I_{ex}(x,y) * G * \int_z c(x,y,z) * \phi_{ref}(x,y,z)\ dz \qquad 9$$

where inhomogeneous excitation signal $I_{ex}(x,y)$ and inhomogeneous dye distribution $c(x,y,z)$ are assumed, and the fluorescence intensity is acquired by a projection along the excitation signal path z. Since the molecular rotor and the reference dye are covalently linked, the local concentration $c(x,y,z)$ should be the same. Additionally, the instrument-dependent factors $I_{ex}(x,y)$ and G as well as the concentration cancel out, leaving a ratio R of steady-state rotor and reference emission of

$$R = \frac{I_{Rotor}}{I_{ref}} = \frac{\phi_F}{\phi_{ref}} = \frac{\phi_0}{\phi_{ref}} * \left(\frac{\eta}{\sigma}\right)^x \qquad 10$$

Equation 10 has two implications. First, assuming a known and constant reference dye quantum yield ϕ_{ref} the ratiometric intensity gives access to the molecular rotor's quantum yield, which is otherwise only obtainable with expensive lifetime equipment. Second, Equation 10 can be solved for viscosity η [23], and the ratiometric intensity R allows direct computation of viscosity where $x, \sigma,$ and ϕ_0 can be considered calibration constants and can be obtained from model solvents.

To keep the emission spectra of these dual emission molecular rotors as simple as possible, a molecular rotor with a single emission band is preferred. This allows the ratio R to produce a concentration-independent self-calibrating measurement of the environmental microviscosity.

Molecular rotors as viscosity sensors

Molecular rotors have been used to quantitatively determine phospholipid microviscosity [12], and observe temperature-dependent viscosity changes of phospholipid bilayers and their sol-gel transition [24, 25]. In addition, molecular rotors have already been used in cell culture to elucidate the influence of FSS on endothelial cell membranes [7]. In the context of Kisaalita and colleagues' main hypothesis that SH-SY5Y neuroblastoma cells exhibit physiologically abnormal membrane stretch when cultured on glass (2D) [8, 9], membrane stretching and the increase in free volume are quite intuitive, which links stretching back to the free volume discussion around Eq. 3. The recent development of ratiometric nanoviscometers also presents new opportunities for studying the effects of a cell's microenvironment on membrane stretch. Using membrane viscosity as a proxy for membrane stretch, with the proposed ratiometric molecular rotors, it will be possible to not only explain the calcium signal difference between 2D and 3D neuroblastoma cultures but will for the first time enable the examination of the membrane viscosity of a cell embedded in a 3D microtissue.

2.4 Cell - cell physical microenvironment interaction

It is well established that cells continuously "sense" the mechanical properties of their environment. Normal physiological functions, including morphogenesis [26], tissue remodeling [27, 28], and differentiation [29, 30] are driven in part by the biophysical microenvironment. Cells use their adhesive and contractile molecular machinery to transmit forces to their surroundings, then transduce those forces to biochemical signals. Fibroblasts have been shown to adapt their internal stiffness to match that of their substrate for a stiffness range spanning that of soft tissues (between 800 Pa and 4 kPa) before reaching a saturation limit (>10 kPa), with an increasing cell stiffness strongly correlating to increased cell area [31]. This suggests that within the stiffness range in which native fibroblasts reside, a cell can quantitatively adapt and match its mechanical environment. Similarly, epithelial cells grown on compliant substrates were less spread and contained irregular ruffles on the ventricle surface [32]. These observations point to two different states of cell adhesion and spreading: stiff substrates result in remodeling of the actin cytoskeleton into stress fibers and increased cell area, and soft substrates on which the cell does not spread out and stress fibers do not exist. Alternatively, motor neurons derived from mouse spinal cords adopt extensive neurite branches on soft but not stiff substrates [33], while some cell types cannot grow on soft (<50 Pa) substrates [32, 34-36]. It is clear that not all adherent cell types respond to biophysical cues from the cellular microenvironment in the same manner.

Although the regulation of focal adhesions and the cytoskeleton has garnered a lot of attention, the plasma membrane is far from a passive participant in mechanotransduction. In addition to maintaining a specific level of blood flow and associated shear stress [7], changes in membrane viscosity and activation of flow-sensitive ion channels facilitate vascular endothelial wound closure under FSS [37]. Membrane viscosity (or membrane fluidity, which is its reciprocal) describes the ease of movement within the phospholipid bilayer, and directly influences physiological properties such as membrane-bound enzyme activity, carrier-mediated transport, and membrane-bound receptor binding [38]. Diffusion rate of molecules and therefore the reaction rates of diffusion-controlled processes are also affected by membrane viscosity. The rate of mass transport of reagents within and across the domains in heterogenous systems like the lipid bilayer are often determined by diffusion-controlled processes, and many complex intracellular processes rely on diffusion as a rate limiting step. In this sense, the dynamic state of the lipid bilayer is akin to other characteristic properties, such as gene and protein expression, which are used to phenotype cell populations.

An open question arising from this collection of observations is how substrate stiffness affects membrane viscosity. Although flattening of membrane ruffles in response to the application of linear strain has been demonstrated [39-41], a link between membrane viscosity and the observable changes in cell area because of tactile sensing of substrate stiffness, has not been conclusively established. Intuition tells us that when cell area increases in response to a stiff substrate, the plasma membrane adopts a physiologically abnormal stretched or “taut” condition (Figure 3). However, lipid bilayers are known to rupture with a relative area increase of 3-5%, with endocytosis [42], exocytosis [43, 44], and unfolding of caveolae [40, 41] being observed experimentally with changes in cell area and believed to relieve membrane tension in order to prevent rupture. Whether physiologically irrelevant substrate stiffness results in membrane viscosity differences when compared to the same cell type grown on a compliant substrate with a stiffness in the range of normal physiologically relevant tissue remains to be seen. If the response to FSS is any indication, cell phenomena that involves perturbation of the plasma membrane, including changes in cell shape and area in response to substrate stiffness, could also affect membrane viscosity. However, as pointed out in the Introduction, current methods to directly or indirectly report membrane physical properties are time-consuming and of little spatial resolution. Below, we summarize the state-of-the-art techniques available.

2.5 Measuring membrane physical properties

Atomic force microscopy (AFM) is currently the gold standard to measure the mechanical properties of cells with a resolution down to nanometer scales. However, differences in assumptions and constitutive models as well as experimental setups such as cantilever characteristics and probe settings [45] make a direct quantitative comparison across studies using AFM infeasible. Probing individual cells is time-consuming and measuring live cells can be problematic if the ability to control environmental parameters (i.e., temperature and %CO2) isn't available. AFM, along with optical tweezers and micropipette aspiration, are invasive techniques limited to surface topologies and are not a direct method for probing membrane viscosity; rather, these techniques measure the "deformability" by applying nanoindentation, shear stresses, and pressure gradients that may elicit an unintended cellular response. The result is the sum of the force needed to deform the membrane (in-plane membrane tension) and the force needed to deform membrane-to-cytoskeleton attachments and membrane proteins. While AFM is typically used to test cells adhered to a surface, micropipette aspiration usually measures cells in suspension. Therefore, cytoskeletal differences associated with adherence or suspension significantly influence the measured properties; adhered cells measured by AFM appear to be less viscous than those in suspension measured by micropipette aspiration [46].

Non-invasive elastography techniques like fluorescence recovery after photobleaching (FRAP) overcome this issue by indirectly reporting membrane viscosity through diffusivity of a fluorophore; however, these techniques are time-consuming and of limited spatial resolution. Depending on instrumentation, a FRAP image may take up to 30 minutes including a 6 to 9-minute photobleaching process [47] during which dye will begin migrating into the irradiated spot, creating a zone of reduced dye concentration around the bleached zone which reduces dye recovery. While molecular rotors report free volume in the immediate surroundings, FRAP reports diffusivity over a relatively large area (e.g., 30µm in the case of [47]).

The notion of viscosity imaging lends itself as a possible alternative method. Molecular rotors require relatively simple steady-state fluorescence instrumentation, report changes in real time, and their spatial resolution is only limited by the optical system. Similar to non-invasive elastography techniques, molecular rotors don't deform the plasma membrane. The result is a direct measurement of membrane microviscosity, which can be reported in viscosity units (mPa * s) [23]. The changes of membrane microviscosity can then be interpreted with respect to the testing parameters, such as substrate stiffness and FSS. If membrane microviscosity can be used as a proxy for membrane stretch it should not only be possible to establish a relationship between membrane microviscosity and the cell stiffness as measured by AFM, but also to establish a relationship between membrane microviscosity and substrate stiffness.

2.6 Adding a third dimension

It has become widely accepted that three-dimensional (3D) platforms support more physiologically relevant cell culture when compared to cells grown on a simple 2D substrate, because 3D platforms better resemble the natural microenvironment of the cells [48, 49]. As one example, human hepatocarcinoma (HepG2) cells cultured in alginate hydrogels better match in vivo tissue samples with respect to morphology, gene expression, and metabolic activity [50]. Hepatocytes are widely used in high-throughput drug screening (HTS) platforms for drug discovery, and evidence points to a more physiologically relevant cell culture providing more physiologically relevant drug responses. 'Physiologically more relevant' claims are often made if the phenotypic characteristics attributed to the culture platform are different between 2D cell culture and cells grown on a platform that provides a loosely defined 3D architecture. Apart from the 3D matrix adhesion [51] as a possible ‘biomarker’ for the three-dimensionality of a cell culture, research in cell biology has not provided a foundation on which these ‘physiologically more relevant’ claims could be validated. Lai and colleagues make the case for cytokines to be the chemical cues monitored to determine the physiological relevance of a platform [52], but the variability and role of cytokine concentrations in 3D cultures are not well understood. In the absence of a ‘biomarker’ of three-dimensionality (i.e., a quantifiable entity) the optimum composition of the 3D microenvironment will remain elusive. As such, a consensus for the ‘three-dimensionality’ of a cell culture should be established.

The microenvironmental factors (MEFs) that support the formation of physiologically relevant 3D cultures (microtissues) have been defined as the following: (i) chemical or biochemical composition, (ii) spatial cues (geometric 3D), (iii) temporal cues, and (iv) substrate biophysical properties [53, 54]. Many different 3D cell culture platforms provide different combinations of MEFs but elicit similar functional and/or structural responses from various cell lines. In fact, many of these cell culture platforms are commercially available and are advertised as “3D”. For instance, HepG2 cells cultivated in Matrigel (Corning Matrigel Growth Factor Reduced Basement Membrane Matrix), collagen sandwich (Corning Collagen I), and Alvetex® (porous polystyrene scaffolds) formed structural bile canaliculi networks, a characteristic associated with hepatocytes in vivo [55]. Interestingly, these platforms have been described in literature as “3D” but are very different in nature. The collagen sandwich consists mostly of one protein element while Matrigel is a mixture of laminin, collagen, fibronectin, and numerous other components. Unlike hydrogels, synthetic polymers like polystyrene have Young’s moduli above the physiological range of native liver tissue and provide a rigid pore structure, preventing tissue growth past the size of the pores. To complicate things further, Luckert *et al.* [55] suggest the comparable metabolic activity of 2D and 3D HepG2 cells might be a consequence of the duration of cultivation, not the result of 3D culture as previously reported [56]. Based on the evidence from literature, we should ask the following questions. What is the minimum level of exogenous MEFs that engender an in vitro tissue model that best emulates the desired in vivo structural and/or function features, and what is the optimum composition of the culture platform to promote this? A precise emulation of in vivo conditions might be necessary for many regenerative medicine applications. In turn, evidence suggests it might not be necessary in the field of drug discovery [55, 56]. Conflicting reports on the importance of providing a 3D architecture for hepatocyte cultures used as a liver model for toxicity studies, and their associated metabolic activity, bring to light the potential redundancy in MEFs for certain applications. Identification and elimination of redundant MEFs may make cell culture platforms more predictive, compatible and affordable for research as well as HTS instrumentation.

The widely-accepted consensus is that in order to achieve in vivo-like microtissues in vitro, the stiffness of a 3D culture platform should be within the physiological range of the native tissue of interest. This consensus is based on cellular responses to 2D substrates, as described in section 3, and studying single cells embedded in a 3D matrix. However, the behavior of isolated cells grown on a 2D substrate or within a 3D matrix might differ from the behavior of an individual cell within a tissue. Maintaining cell-cell adhesion is crucial for tissue morphogenesis and homeostasis, while perturbation of the keratin-desmosome complex, to name just one example, severely compromises cell and tissue integrity [57, 58]. Furthermore, Doyle *et al.* [59] suggest that the average stiffness of a 3D collagen gel obtained using bulk rheological measurements doesn’t indicate the local differences in fiber stiffness a cell may “sense” at the fiber/cell adhesion scale. A better understanding of how the stiffness of various 3D culture platforms affect microtissues growing within the platform could provide valuable insight into potential redundancy of substrate biophysical MEFs.

While single endothelial cells "sense" the pliability of their substrate and respond with cytoskeleton remodeling and morphology changes, an endothelial cell monolayer grown to confluency has indistinguishable morphologies on both pliable and rigid surfaces [60]. A possible explanation for the lack of morphological changes mentioned above comes from the 'cell-on-cell' hypothesis [29], where cell-to-cell contacts appear to influence the cellular response to the mechanical properties of the environment. For example, when cultured on stiff substrates, myotubes form stress fibers and strong focal adhesions, suggesting a state of isometric contraction; on soft substrates, actomyosin appears scattered. Both cellular responses are consistent with other 2D mechanotransduction observations discussed in section 3. Moreover, when a gel matching relaxed muscle bundles ($E \approx 10$kPa) is used as a substrate, definitive actomyosin striations are observed. The 'cell-on-cell' hypothesis comes into the picture when myotubes are cultured on top of an initial myotube monolayer. While the lower myotube monolayer attaches strongly to glass and form numerous stress fibers, the upper myotubes differentiate to the more physiological state, with prominent actomyosin striations and cell elasticity in the range of normal muscle tissue [29]. Similarly, a basal layer of astrocytes cultured on glass seems to impart a pliable brain-like environment for branching of neurons to grow [61]. These observations suggest that these cell-to-cell contacts provide a soft "barrier" between the cell being studied and the substrate, which lends credibility to the concept that physiologically relevant microtissues can be cultured on substrates that have a physiologically abnormal stiffness.

The hypothesis provided by Kisaalita and colleagues to explain differences in high potassium depolarization-induced calcium entry for SH-SY5Y neuroblastoma cells grown on 2D substrates or as 3D microtissues is interesting in the context of the cell-on-cell hypothesis. In these experiments the same substrate materials (poly (l-lactic acid), polystyrene) were used for both 2D and 3D models; therefore, the difference between the two platforms was the geometric space available for cell growth and the resulting difference in cell interactions. Differences in cell spreading, in terms of neuroblast projection areas and perimeters, and VGCC response indicate a change in cell membrane stretch when grown on 2D substrates versus 3D. Although 3D cell culture is currently a hot research topic, there is a real lack of information regarding the biomechanical properties and mechanotransduction behavior of cells grown in a cohesive, 3D microtissue. This is mainly due to limitations in techniques for studying mechanical properties of cells in 3D cultures. Although identifying and measuring a single cell grown on a 2D substrate with the current gold standards, such as AFM and micropipette aspiration, is rather straight forward, the same cannot be said for identifying and measuring a cell that is a part of a 3D tissue. One major challenge of using fluorescent dye methods such as FRAP with 3D cell cultures is that you can’t reach the center of a cell cluster with a photobleaching pulse. Another is diffusion of the dye to the core of the sample. The advantage of using ratiometric nanoviscometers over other fluorescent dyes is that these dual emission dyes are self-calibrating, making homogenous dye concentration irrelevant (see Section 2.2). Confocal imaging systems have several features that result in improved lateral and axial resolution over other fluorescence instruments, allowing the user to image a very thin z-section of a 3D specimen. With these probes, it will be possible to not only explain the calcium signal difference between 2D and 3D preparation but also enable the examination of the influence of 3D platform stiffness on microtissues as the distance of the cell location from the platform surface increases. If the influence is limited to only the layer of cells adjacent to the platform surface, 3D platform stiffness becomes less pertinent to the physiological relevance of the resulting microtissue. In this case, the biophysical microenvironmental factor could be considered a redundancy for certain in vitro 3D culture applications. If cells in the interior of the microtissue are affected, this strengthens the argument to develop/use materials that are consistent with in vivo microenvironmental stiffness.

2.7 Concluding remarks

The focus of this review has been on the application of fluorescent molecular rotors to basic 2D and more complex 3D cell culture for studying the effects of biophysical signals on cell state. In addition to the fundamental interest, there is a practical need to quantitatively measure changes in cell mechanics. Cell culture applications of molecular rotors are not just limited to the study of physical properties but have the potential to be used as a tool for studying stem and cancer cells. Evidence from literature shows stem cells of various lineages and cancer cells with different levels of invasiveness have significant differences in cell physical properties, and there remains a need to identify cells within heterogenous populations.

It has been suggested that cancer cell stiffness plays a role in invasion of surrounding tissues. Although cancer tissues have shown to be stiffer than normal tissues, recent reports suggest metastatic cancer cells themselves are more compliant than normal cells [62, 63]. Swaminathan *et al.* demonstrate the stiffness of patient tumor cells and cancer cell lines inversely correlate with migration and invasion through 3D basement membranes [64]. While a better understanding of the onset and progression of cancer can lead to improved detection and more efficacious anti-cancer drug testing, the potential for single cell mechanical properties to be used as a biomarker for disease is promising. If a change in mechanical phenotype is an indicator of metastasis, then molecular rotors could be used to study the utility of various cancer cell lines as in vitro cancer models. Molecular rotors are an attractive tool for mechanical property-based screening because, unlike benchtop methods like AFM and micropipette aspiration, they have the potential to be translated to an off-the-shelf assay that can be applied to fluorescence activated cell sorting (FACS) instrumentation. Other potential applications include combination with microfluidic devices to study single cell mechanics during migration and intravascular adhesion of metastatic cell lines.

Studies of single cell mechanical properties for adipose-derived stem cells (ASCs) enrichment has shown the potential for distinguishing differences in cell subpopulations, disease state, and tissue source based on mechanical properties [65]. As one example, the cellular biomechanics are remodeled during osteogenic differentiation, which may precede up-regulation of the osteogenic markers [66]. Membrane viscosity of undifferentiated stem cells could be correlated with lineage-specific metabolite production, potentially providing a more complete understanding of differentiation. While fundamental stem cell research aims to understand differentiation patterns, clinical applications of stem cells have shown great potential as a novel therapeutic alternative for musculoskeletal, hematopoietic, neurological, and cardiovascular disorders [67, 68]. Autologous ASCs are just one attractive cell source for cell-based regenerative therapies due to their immunogenicity and multipotent characteristics and are available in large quantities compare to MSCs derived from other tissues. However, adipose tissue contains multiple cell types and only a portion of MSCs satisfy the stem cell criteria, while others are more committed to a specific lineage [69, 70]. Furthermore, the long-term and large-scale in vitro adherent culture expansion of MSCs necessary to obtain a clinically relevant number of cells for therapeutic use results in reduced multilineage potential [71, 72]. Although studies suggest the potential for cellular mechanical properties as a novel ‘biomarker’ of cell phenotype, quantitative comparisons across different studies have proven difficult. Mechanical properties within a specific cell lineage have varied by up to an order of magnitude between different research groups, as shown in Table 1. In addition to differences in assumptions and constitutive models as well as experimental setups, these quantitative methods are not amenable to high-throughput applications, which limits their use to fundamental studies of single-cell mechanical properties. Ratiometric molecular rotors are unique in that instrument-dependent factors cancel out (see Section 2, Equation 10) making comparisons of cellular mechanical properties across lineages and studies more feasible. Although ASCs have several surface markers, many of these are shared with other cells present in adipose tissue [73]. Multivariate analysis of MSC multipotency biophysical markers suggests that no single biophysical property is robust enough to predict stem cell multipotency alone [74]. However, cell stiffness as a potential biophysical marker reported by ratiometric molecular rotor fluorescence, together with surface biomarkers (and potentially with other properties such as cell size), could improve the purification of multipotent subpopulations or differentiation of tripotent MSCs and MSCs that have already committed to a specific lineage.

In vitro cell culture has evolved into complex systems, which require new tools to study cell phenomena. Cell physical properties have become a popular ‘marker’ for cell physiological studies, but limitations in instrumentation make it difficult to study this in complex systems. Molecular rotors lend themselves to the notion of *viscosity imaging* which could prove to be a useful alternative. This tool provides the opportunity to study complex 3D cell systems and has the potential to become a useful approach to sorting heterogenous cell samples.

2.8 References

1. Förster, T. and G. Hoffmann, Die viskositätsabhängigkeit der fluoreszenzquantenausbeuten einiger farbstoffsysteme. Zeitschrift für Physikalische Chemie, 1971. 75(1_2): p. 63-76.
2. Rotkiewicz, K., K. Grellmann, and Z. Grabowski, Reinterpretation of the anomalous fluorescense of pn, n-dimethylamino-benzonitrile. Chemical Physics Letters, 1973. 19(3): p. 315-318.
3. Zhu, D., et al., Application of molecular rotors to the determination of the molecular weight dependence of viscosity in polymer melts. Macromolecules, 2007. 40(21): p. 7730-7732.
4. Mustafic, A., et al., Imaging of flow patterns with fluorescent molecular rotors. Journal of fluorescence, 2010. 20(5): p. 1087-1098.
5. Malacrida, L., D.M. Jameson, and E. Gratton, A multidimensional phasor approach reveals LAURDAN photophysics in NIH-3T3 cell membranes. Scientific reports, 2017. 7(1): p. 9215.
6. Sameni, S., et al., Alteration in fluidity of cell plasma membrane in Huntington disease revealed by spectral phasor analysis. Scientific reports, 2018. 8(1): p. 734.
7. Haidekker, M.A., N. L'Heureux, and J.A. Frangos, Fluid shear stress increases membrane fluidity in endothelial cells: a study with DCVJ fluorescence. American journal of physiology. Heart and circulatory physiology, 2000. 278(4): p. H1401-6.
8. Lai, Y., K. Cheng, and W. Kisaalita, Three dimensional neuronal cell cultures more accurately model voltage gated calcium channel functionality in freshly dissected nerve tissue. PLoS One, 2012. 7(9): p. e45074.

9. Wu, Z.Z., et al., Responsiveness of voltage-gated calcium channels in SH-SY5Y human neuroblastoma cells on quasi-three-dimensional micropatterns formed with poly (l-lactic acid). Int J Nanomedicine, 2013. 8: p. 93-107.

10. Haidekker, M.A., et al., Dyes with segmental mobility: molecular rotors, in Advanced Fluorescence Reporters in Chemistry and Biology I. 2010, Springer. p. 267-308.

11. Haidekker, M.A., et al., Effects of solvent polarity and solvent viscosity on the fluorescent properties of molecular rotors and related probes. Bioorg Chem, 2005. 33(6): p. 415-25.

12. Kung, C.E. and J.K. Reed, Microviscosity measurements of phospholipid bilayers using fluorescent dyes that undergo torsional relaxation. Biochemistry, 1986. 25(20): p. 6114-6121.

13. Loutfy, R.O. and B.A. Arnold, Effect of viscosity and temperature on torsional relaxation of molecular rotors. The Journal of Physical Chemistry, 1982. 86(21): p. 4205-4211.

14. Doolittle, A.K., Studies in Newtonian flow. III. The dependence of the viscosity of liquids on molecular weight and free space (in homologous series). Journal of Applied Physics, 1952. 23(2): p. 236-239.

15. Grabowski, Z.R., K. Rotkiewicz, and W. Rettig, Structural changes accompanying intramolecular electron transfer: focus on twisted intramolecular charge-transfer states and structures. Chemical reviews, 2003. 103(10): p. 3899-4032.

16. Singer, S. and G.L. Nicolson, The fluid mosaic model of the structure of cell membranes. Membranes and Viruses in Immunopathology; Day, SB, Good, RA, Eds, 1972: p. 7-47.

17. Vereb, G., et al., Dynamic, yet structured: the cell membrane three decades after the Singer–Nicolson model. Proceedings of the National Academy of Sciences, 2003. 100(14): p. 8053-8058.

18. Engelman, D.M., Membranes are more mosaic than fluid. Nature, 2005. 438(7068): p. 578-580.

19. Kuimova, M.K., et al., Molecular rotor measures viscosity of live cells via fluorescence lifetime imaging. Journal of the American Chemical Society, 2008. 130(21): p. 6672-6673.

20. Levitt, J.A., et al., Membrane-bound molecular rotors measure viscosity in live cells via fluorescence lifetime imaging. The Journal of Physical Chemistry C, 2009. 113(27): p. 11634-11642.

21. Haidekker, M.A. and E.A. Theodorakis, Ratiometric mechanosensitive fluorescent dyes: Design and applications. J Mater Chem C Mater, 2016. 4(14): p. 2707-2718.

22. Dakanali, M., et al., Self-calibrating viscosity probes: design and subcellular localization. Bioorg Med Chem, 2012. 20(14): p. 4443-50.

23. Yoon, H.J., et al., Synthesis and evaluation of self-calibrating ratiometric viscosity sensors. Org Biomol Chem, 2011. 9(9): p. 3530-40.

24. Haidekker, M.A., et al., Phospholipid-bound molecular rotors: synthesis and characterization. Bioorganic & medicinal chemistry, 2002. 10(11): p. 3627-3636.

25. Lukac, S., Thermally induced variations in polarity and microviscosity of phospholipid and surfactant vesicles monitored with a probe forming an intramolecular charge-transfer complex. Journal of the American Chemical Society, 1984. 106(16): p. 7.

26. Xie, K., Y. Yang, and H. Jiang, Controlling cellular volume via mechanical and physical properties of substrate. Biophysical journal, 2018. 114(3): p. 675-687.

27. Huiskes, R., et al., Effects of mechanical forces on maintenance and adaptation of form in trabecular bone. Nature, 2000. 405(6787): p. 704.

28. Boerckel, J.D., et al., Mechanical regulation of vascular growth and tissue regeneration in vivo. Proceedings of the National Academy of Sciences, 2011. 108(37): p. E674-E680.

29. Discher, D.E., P. Janmey, and Y.L. Wang, Tissue cells feel and respond to the stiffness of their substrate. Science, 2005. 310(5751): p. 1139-43.

30. Engler, A.J., et al., Matrix elasticity directs stem cell lineage specification. Cell, 2006. 126(4): p. 677-689.

31. Solon, J., et al., Fibroblast adaptation and stiffness matching to soft elastic substrates. Biophysical journal, 2007. 93(12): p. 4453-4461.

32. Pelham, R.J. and Y.-l. Wang, Cell locomotion and focal adhesions are regulated by substrate flexibility. Proceedings of the National Academy of Sciences, 1997. 94(25): p. 13661-13665.

33. Flanagan, L.A., et al., Neurite branching on deformable substrates. Neuroreport, 2002. 13(18): p. 2411.

34. Georges, P.C. and P.A. Janmey, Cell type-specific response to growth on soft materials. Journal of applied physiology, 2005. 98(4): p. 1547-1553.

35. Engler, A.J., et al., Myotubes differentiate optimally on substrates with tissue-like stiffness. J Cell Biol, 2004. 166(6): p. 877-887.

36. Wang, H.-B., M. Dembo, and Y.-L. Wang, Substrate flexibility regulates growth and apoptosis of normal but not transformed cells. American Journal of Physiology-Cell Physiology, 2000. 279(5): p. C1345-C1350.

37. Gojova, A. and A.I. Barakat, Vascular endothelial wound closure under shear stress: role of membrane fluidity and flow-sensitive ion channels. Journal of Applied Physiology, 2005. 98(6): p. 2355-2362.

38. Spector, A.A. and M.A. Yorek, Membrane lipid composition and cellular function. Journal of lipid research, 1985. 26(9): p. 1015-1035.

39. Kosmalska, A.J., et al., Physical principles of membrane remodelling during cell mechanoadaptation. Nature communications, 2015. 6: p. 7292.

40. Gervásio, O.L., et al., Caveolae respond to cell stretch and contribute to stretch-induced signaling. J Cell Sci, 2011. 124(21): p. 3581-3590.

41. Sinha, B., et al., Cells respond to mechanical stress by rapid disassembly of caveolae. Cell, 2011. 144(3): p. 402-413.

42. Raucher, D. and M.P. Sheetz, Membrane expansion increases endocytosis rate during mitosis. The Journal of cell biology, 1999. 144(3): p. 497-506.

43. Gauthier, N.C., et al., Temporary increase in plasma membrane tension coordinates the activation of exocytosis and contraction during cell spreading. Proceedings of the National Academy of Sciences, 2011. 108(35): p. 14467-14472.

44. Gauthier, N.C., et al., Plasma membrane area increases with spread area by exocytosis of a GPI-anchored protein compartment. Molecular biology of the cell, 2009. 20(14): p. 3261-3272.

45. Vahabikashi, A., et al., Probe Sensitivity to Cortical versus Intracellular Cytoskeletal Network Stiffness. Biophysical journal, 2019. 116(3): p. 518-529.

46. Darling, E., S. Zauscher, and F. Guilak, Viscoelastic properties of zonal articular chondrocytes measured by atomic force microscopy. Osteoarthritis and cartilage, 2006. 14(6): p. 571-579.

47. Majd, S. and M. Mayer, Hydrogel stamping of arrays of supported lipid bilayers with various lipid compositions for the screening of drug–membrane and protein–membrane interactions. Angewandte Chemie, 2005. 117(41): p. 6855-6858.

48. Baker, B.M. and C.S. Chen, Deconstructing the third dimension–how 3D culture microenvironments alter cellular cues. J Cell Sci, 2012. 125(13): p. 3015-3024.

49. Pampaloni, F., E.G. Reynaud, and E.H. Stelzer, The third dimension bridges the gap between cell culture and live tissue. Nature reviews Molecular cell biology, 2007. 8(10): p. 839-845.

50. Lan, S.-F., B. Safiejko-Mroczka, and B. Starly, Long-term cultivation of HepG2 liver cells encapsulated in alginate hydrogels: a study of cell viability, morphology and drug metabolism. Toxicology in Vitro, 2010. 24(4): p. 1314-1323.

51. Cukierman, E., et al., Taking cell-matrix adhesions to the third dimension. Science, 2001. 294(5547): p. 1708-1712.

52. Lai, Y., A. Asthana, and W.S. Kisaalita, Biomarkers for simplifying HTS 3D cell culture platforms for drug discovery: the case for cytokines. Drug discovery today, 2011. 16(7): p. 293-297.

53. Asthana, A. and W.S. Kisaalita, Microtissue size and hypoxia in HTS with 3D cultures. Drug Discov Today, 2012. 17(15-16): p. 810-7.

54. Asthana, A. and W.S. Kisaalita, Is time an extra dimension in 3D cell culture? Drug discovery today, 2016. 21(3): p. 395-399.

55. Luckert, C., et al., Comparative analysis of 3D culture methods on human HepG2 cells. Archives of toxicology, 2017. 91(1): p. 393-406.

56. Ramaiahgari, S.C., et al., A 3D in vitro model of differentiated HepG2 cell spheroids with improved liver-like properties for repeated dose high-throughput toxicity studies. Arch Toxicol, 2014. 88(5): p. 1083-95.

57. El Ghalbzouri, A., et al., Basement membrane reconstruction in human skin equivalents is regulated by fibroblasts and/or exogenously activated keratinocytes. Journal of investigative dermatology, 2005. 124(1): p. 79-86.

58. McMillan, J.R. and H. Shimizu, Desmosomes: structure and function in normal and diseased epidermis. The Journal of dermatology, 2001. 28(6): p. 291-298.

59. Doyle, A.D., et al., Local 3D matrix microenvironment regulates cell migration through spatiotemporal dynamics of contractility-dependent adhesions. Nature communications, 2015. 6.

60. Yeung, T., et al., Effects of substrate stiffness on cell morphology, cytoskeletal structure, and adhesion. Cell motility and the cytoskeleton, 2005. 60(1): p. 24-34.

61. Georges, P.C., et al., Matrices with compliance comparable to that of brain tissue select neuronal over glial growth in mixed cortical cultures. Biophysical journal, 2006. 90(8): p. 3012-3018.

62. Cross, S.E., et al., Nanomechanical analysis of cells from cancer patients. Nature nanotechnology, 2007. 2(12): p. 780-783.

63. Remmerbach, T.W., et al., Oral cancer diagnosis by mechanical phenotyping. Cancer research, 2009. 69(5): p. 1728-1732.

64. Swaminathan, V., et al., Mechanical stiffness grades metastatic potential in patient tumor cells and in cancer cell lines. Cancer research, 2011. 71(15): p. 5075-5080.

65. Darling, E.M., et al., Viscoelastic properties of human mesenchymally-derived stem cells and primary osteoblasts, chondrocytes, and adipocytes. Journal of biomechanics, 2008. 41(2): p. 454-464.

66. Titushkin, I.A. and M.R. Cho. Controlling cellular biomechanics of human mesenchymal stem cells. in Engineering in Medicine and Biology Society, 2009. EMBC 2009. Annual International Conference of the IEEE. 2009. IEEE.

67. Trounson, A. and C. McDonald, Stem cell therapies in clinical trials: progress and challenges. Cell stem cell, 2015. 17(1): p. 11-22.

68. Wu, X., et al., Muscle-derived stem cells: isolation, characterization, differentiation, and application in cell and gene therapy. Cell and tissue research, 2010. 340(3): p. 549-567.

69. Russell, K.C., et al., In vitro high-capacity assay to quantify the clonal heterogeneity in trilineage potential of mesenchymal stem cells reveals a complex hierarchy of lineage commitment. Stem cells, 2010. 28(4): p. 788-798.

70. Stich, S., et al., Characterization of single cell derived cultures of periosteal progenitor cells to ensure the cell quality for clinical application. PloS one, 2017. 12(5): p. e0178560.

71. McMurray, R.J., et al., Nanoscale surfaces for the long-term maintenance of mesenchymal stem cell phenotype and multipotency. Nature materials, 2011. 10(8): p. 637.

72. Pevsner-Fischer, M., S. Levin, and D. Zipori, The origins of mesenchymal stromal cell heterogeneity. Stem Cell Reviews and Reports, 2011. 7(3): p. 560-568.

73. González-Cruz, R.D. and E.M. Darling, Adipose-derived stem cell fate is predicted by cellular mechanical properties. Adipocyte, 2013. 2(2): p. 87-91.

74. Lee, W.C., et al., Multivariate biophysical markers predictive of mesenchymal stromal cell multipotency. Proceedings of the National Academy of Sciences, 2014. 111(42): p. E4409-E4418.

75. Bongiorno, T., et al., Mechanical stiffness as an improved single-cell indicator of osteoblastic human mesenchymal stem cell differentiation. Journal of biomechanics, 2014. 47(9): p. 2197-2204.

76. Titushkin, I. and M. Cho, Modulation of cellular mechanics during osteogenic differentiation of human mesenchymal stem cells. Biophysical journal, 2007. 93(10): p. 3693-3702.

77. Yourek, G., M.A. Hussain, and J.J. Mao, Cytoskeletal changes of mesenchymal stem cells during differentiation. ASAIO journal (American Society for Artificial Internal Organs: 1992), 2007. 53(2): p. 219.

78. Yu, H., et al., Mechanical behavior of human mesenchymal stem cells during adipogenic and osteogenic differentiation. Biochemical and biophysical research communications, 2010. 393(1): p. 150-155.

79. Koay, E.J., A.C. Shieh, and K.A. Athanasiou, Creep indentation of single cells. Journal of biomechanical engineering, 2003. 125(3): p. 334-341.

80. Charras, G.T. and M.A. Horton, Single cell mechanotransduction and its modulation analyzed by atomic force microscope indentation. Biophysical journal, 2002. 82(6): p. 2970-2981.

81. Charras, G.T. and M.A. Horton, Determination of cellular strains by combined atomic force microscopy and finite element modeling. Biophysical journal, 2002. 83(2): p. 858-879.

82. Solon, J., et al., Fibroblast adaptation and stiffness matching to soft elastic substrates. Biophys J, 2007. 93(12): p. 4453-61.

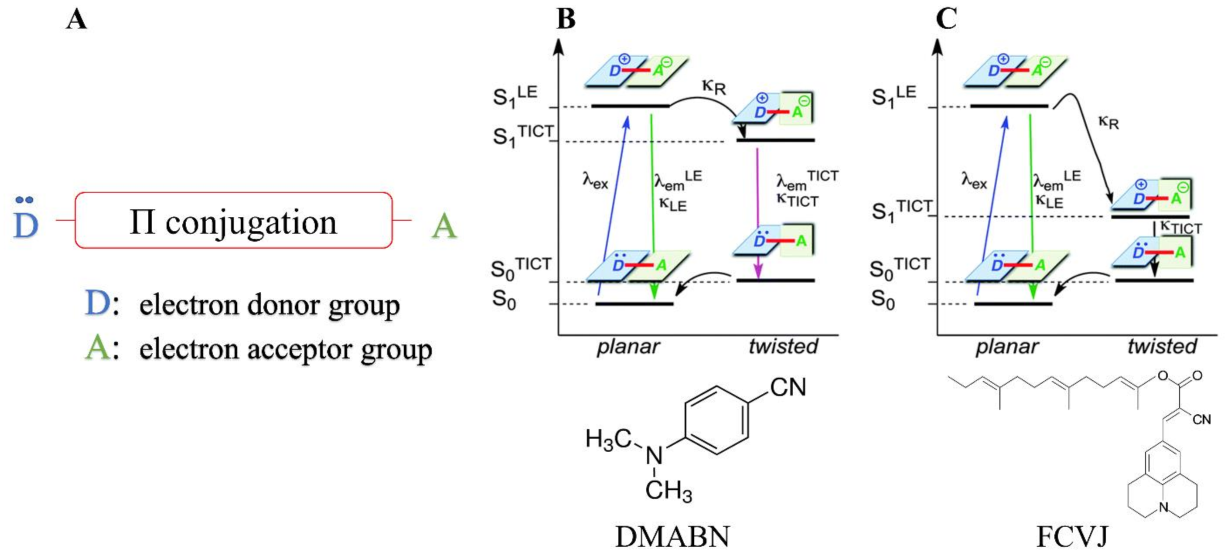

Figure 2.1: Structure and twisted intramolecular charge transfer (TICT) states and kinetics for molecular rotors. (A) Generic motif of a molecular rotor. Jablonski diagram of a dual emission (e.g., DMABN) (B) and a single emission (e.g., FCVJ) (C) molecular rotor. The electronic states are organized vertically by energy and horizontally by spin multiplicity. Radiative transitions involve the absorption, if the transition is to a higher energy level, or in the reverse case, emission of a photon, and are represented by colored arrows. Nonradiative transitions are indicated by black arrows. Adapted from Haidekker and Theodorakis [21] with permission from the Royal Society of Chemistry.

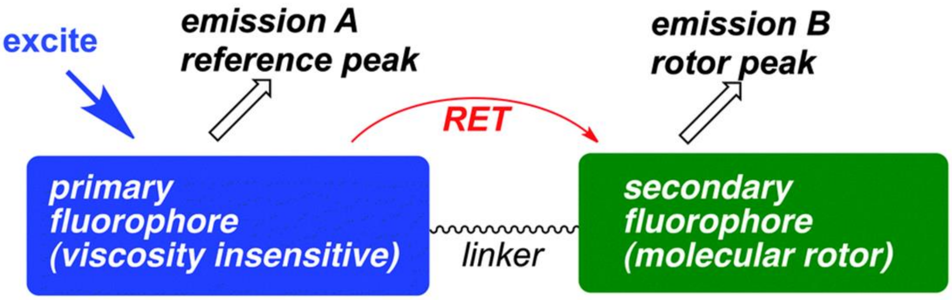

Figure 2.2: Generic motif of ratiometric twisted intramolecular charge transfer (TICT) nanoviscometers based on resonance energy transfer (RET) concept. The viscosity insensitive reference fluorophore is excited and emits at reference peak A. The reference emission peak A has a significant overlap with the covalently linked molecular rotor excitation spectrum, allowing the viscosity sensitive molecular rotor to be excited via RET. The molecular rotor emits at rotor peak B, with the emission quantum yield depending on environmental microviscosity. Reprinted from Haidekker and Theodorakis [21] with permission from the Royal Society of Chemistry.

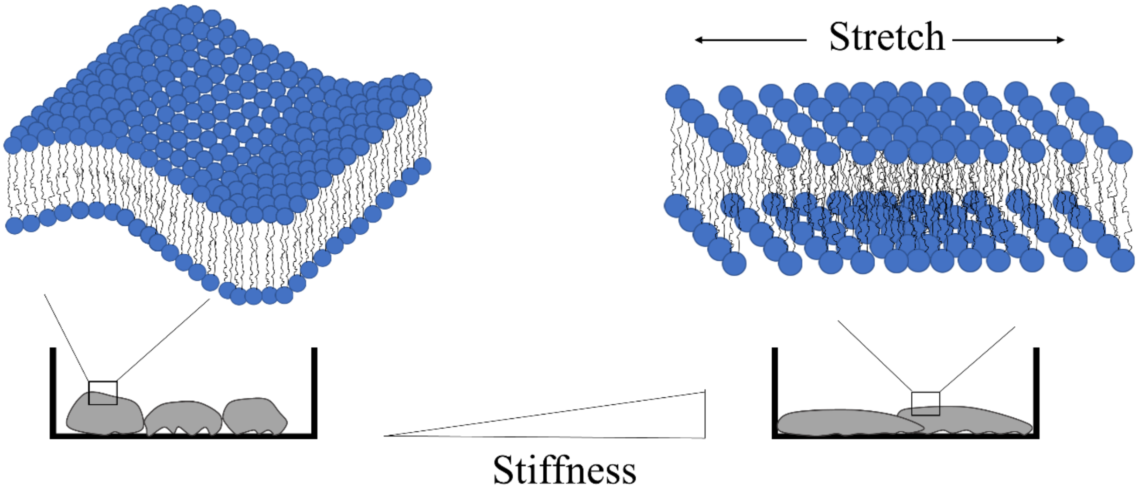

Figure 2.3: Differences in substrate stiffness have been linked to changes in cell shape [82], and the bilayer membrane must accommodate these changes. Passive remodeling of the membrane includes flattening of membrane ruffles in response to cell stretch [39], which we hypothesize is associated with an increase in macromolecular free-volume.

Table 2.1: Elastic moduli of several stem cell lineages measured by common techniques.

Cell Type	**Elastic Modulus (kPa)**	**Measurment Technique**	**Notes**	**Reference**
Mesenchymal Stem Cell				
human bone marrow-derived (Texas A&M)	2.8	AFM indentation	spread morphology on glass coverslip; spherical AFM tip	75
human adipose-derived (Zen-Bio Inc.); passage 4	2.5 ± 1.2	AFM indentation	spread morphology on PLL-coated TCP; nucleus measured; spherical AFM tip	65
human adipose-derived (Zen-Bio Inc.); passage 4	2.6 ± 1.6	AFM indentation	spherical morphology on PLL-coated TCP; nucleus measured; spherical AFM tip	65
human bone marrow-derived (Cambrex and Tulane Center for Gene Therapy); passage 4	3.2 ± 2.2	AFM indentation	spread morphology on PLL-coated TCP; nucleus measured; spherical AFM tip	65
human bone marrow-derived (Cambrex and Tulane Center for Gene Therapy); passage 4	2.5 ± 1.8	AFM indentation	spherical morphology on PLL-coated TCP; nucleus measured; spherical AFM tip	65
human adipose-derived; passage 3	0.345 ± 0.15	AFM indentation	spread morphology on PLL-coated TCP; spherical AFM tip	73
human adipose-derived; passage 4	0.884 ± 0.497	AFM indentation	spread morphology on PLL-coated TCP; spherical AFM tip	73
human adipose-derived; passage 5	0.8 ± 0.511	AFM indentation	spread morphology on PLL-coated TCP; spherical AFM tip	73

human bone marrow-derived (Tulane Center for Gene Therapy)	3.2 ± 1.4	AFM indentation	spread morphology on glass coverslips; cytoplasm measured; spherical AFM tip	76
human bone marrow-derived (AllCells)	33 ± 7	AFM indentation	spread morphology on Thermanox glass coverslips; pyramidal AFM tip	77
human bone marrow-derived (Cambrex Inc.); passage 5	0.466 ± 0.087	Micropipette Aspiration	spherical morphology in suspension; cytoplasm measured	78
Adipocyte				
Primary cells isolated from human fat	0.9 ± 0.8	AFM indentation	spherical morphology on PLL-coated TCP; nucleus measured; spherical AFM tip	65
Adipogenic differentiation				
day 7 of induction	0.671 ± 0.158	Micropipette Aspiration	spherical morphology in suspension; cytoplasm measured	78
day 21 of induction	0.42 ± 0.052	Micropipette Aspiration	spherical morphology in suspension; cytoplasm measured	78
Chondrocyte				
Porcine, superficial articular chondrocytes harvested from femoral condyles	0.46 ± 0.22	AFM indentation	spherical morphology on PLL-coated glass; central region of cell measured; spherical AFM tip	46
Porcine, middle/deep zone articular chondrocytes harvested from femoral condyles	0.26 ± 0.14	AFM indentation	spherical morphology on PLL-coated glass; central region of cell measured; spherical AFM tip	46

Porcine, middle/deep zone articular chondrocytes harvested from femoral condyles	0.2 ± 0.07	Micropipette Aspiration	spherical morphology in suspension; central region of cell measured; spherical AFM tip	46
Primary cells isolated from human, full thickness articular cartilage	1.8 ± 1.7	AFM indentation	spread morphology on PLL-coated TCP; nucleus measured; spherical AFM tip	65
Primary cells isolated from human, full thickness articular cartilage	1.4 ± 1.1	AFM indentation	spherical morphology on PLL-coated TCP; nucleus measured; spherical AFM tip	65
Bovine, articular chondrocytes isolated from cartilage of the first metatarsal	1.10 ± 0.48	Creep indentation	spherical morphology on glass coverslip; spherical probe tip	79
Chondrogenic differentiation				
day 14 of induction	38 ± 10	AFM indentation	spread morphology on Thermanox glass coverslips; pyramidal AFM tip	77
Osteoblast				
Normal human osteoblasts (Lonza)	1.9	AFM indentation	spread morphology on glass coverslip; spherical AFM tip	75
Murine, isolated from long bones	3.175	AFM indentation	spread morphology on glass; spherical AFM tip	80
Murine, isolated from long bones	14	AFM indentation	spread morphology on glass; pyramidal AFM tip	81
Primary cells isolated from human bone	6.5 ± 2.7	AFM indentation	spread morphology on PLL-coated TCP; nucleus measured; spherical AFM tip	65

Primary cells isolated from human bone	2.6 ± 2.0	AFM indentation	spherical morphology on PLL-coated TCP; nucleus measured; spherical AFM tip	65
human fetal osteoblasts (hFOB 1.19) (ATCC)	1.7 ± 0.3	AFM indentation	spread morphology on glass coverslips; cytoplasm measured; spherical AFM tip	76
Osteogenic differentiation				
day 10 of induction	2.8	AFM indentation	spread morphology on glass coverslip; spherical AFM tip	75
day 20 of induction	1.4	AFM indentation	spread morphology on glass coverslip; spherical AFM tip	75
day 10 of induction	2.1 ± 0.9	AFM indentation	spread morphology on glass coverslips; cytoplasm measured; spherical AFM tip	76
day 14 of induction	52 ± 5	AFM indentation	spread morphology on Thermanox glass coverslips; pyramidal AFM tip	77
day 7 of induction	0.631 ± 0.166	Micropipette Aspiration	spherical morphology in suspension; cytoplasm measured	78
day 21 of induction	0.89 ± 0.219	Micropipette Aspiration	spherical morphology in suspension; cytoplasm measured	78

Abbreviations: hMSC: human mesenchymal stem cell; AFM: atomic force microscopy; TCP: tissue culture plastic

CHAPTER 3

PATTERNED POLYSTYRENE MULTIWELL PLATES FOR 3D CELL CULTURE IMAGING[2]

---

[2] White, C. M., Ndyabawe, K., Asthana, A.., and Kisaalita, W. S. To be submitted to SLAS Technology

3.1 Abstract

The work reported here demonstrates a polydimethylsiloxane (PDMS) -based hot embossing approach for low-cost prototyping of polystyrene (PS) microwell cell culture platforms. Unlike conventional hot embossing, the method reported here does not require any special tools or equipment. Micron-scale wells were successfully replicated in 0.4 mm thick PS sheets using a PDMS stamp fabricated via soft lithography, two 1” binder clips, two standard glass microscopy slides and an oven. The PDMS stamps were reusable without any damage. We demonstrate fibroblast cell adhesion to the PS wells as well as microtissue formation, with potential applications for high throughput screening (HTS) assays.

3.2 Introduction

It is now widely accepted that in comparison to two-dimensional (2D), three-dimensional (3D) cell cultures have a greater potential to imitate in vivo conditions. Thus, it is important to optimize cell culture conditions to ensure experimental reproducibility, and many research groups have invested heavily in studying the effects of the in vitro cellular microenvironment. A popular study by Discher et al. reports observations that for some adherent cell cultures, numerous cell-cell contacts may negate the effects of substrate stiffness, leading to the formation of the cell-on-cell hypothesis [1]. Validating the cell-on-cell hypothesis could make materials with physiologically irrelevant mechanical properties attractive alternatives for certain applications, like high-throughput screening (HTS) assays, where other platforms, such as hydrogels and scaffold-free cultures, have shortcomings. To explore the cell-on-cell hypothesis further, a culture platform that allows 3D microtissue formation and promotes cell-substrate and cell-cell interactions needs to be developed. Appropriate spatial, temporal, and mechanical cues are necessary for the platform to be successful. The platform must also have suitable optical properties for confocal microscopy imaging of fluorescent molecular rotors. From an engineer's perspective, the design approach must be manufacturable, reproducible, and affordable.

Polystyrene (PS) is central to in vitro cell-based research due to its commercial availability as tissue culture plasticware and is therefore unlikely to be replaced by other materials. It has excellent optical properties compared to other materials, can be colored white by the addition of titanium oxide for luminescence or absorbance or black by the addition of carbon for fluorescence assays. PS can be sterilized post-molding and surface modified with oxygen-rich plasma or adsorption of matrix proteins. Additionally, the Young's Modulus of PS is in the range of 3 - 3.6 GPa, well outside the physiologically relevant range, making it an excellent material choice for testing the cell-on-cell hypothesis.

In this paper, we present a 3D culture platform suitable for studying the cell-on-cell hypothesis using fluorescent molecular rotors. The approach for developing a 3D culture platform described here allows for specifically defined microwells to be hot embossed into PS sheets, which can easily be achieved on a small scale in a laboratory setting. This low-cost approach to 3D culture platform fabrication will hopefully encourage researchers to explore other possible applications and experiment with design. We also discuss the potential for scale up in manufacturing and scale down to a 96-well plate format for HTS applications.

3.3 Design and Fabrication

Figure 1 depicts the different stages taken to create our 3D culture platform. The culture platform design was inspired by Cheng et al. "three-dimensional polymer scaffolds for HTS cell-based assay systems" which presents a microporous PS scaffold that can be integrated with standard cell culture dishes and microwell plates [2]. Whereas in their study the micropores were created using sieved ammonium bicarbonate particles mixed with a solution of PS dissolved in chloroform, we wanted to have precise control over the pattern and size of the micropores. We were inspired by the simplicity of the Cheng et al. scaffold fabrication [2]. The advantages of using SU-8 negative photoresist to create high aspect ratio structures on the micron scale were previously studied in our lab [3]. Our pattern was designed using autoCAD and a photomask was purchased from a vendor ($67 including shipping). Photolithography is a commonly available capability in university settings for design and fabrication of microfluidics [4, 5] and microelectromechanical systems (MEMS) [6-8] devices with SU-8 negative photoresist.

Although SU-8 devices have many different applications, the structures are usually in the micron range and the bond between the SU-8 structures and the base (in our case, a silicon wafer) is strong, and therefore prone to damage if performing multiple replications. This does not make them ideal as a reusable master mold for device prototyping. Soft lithography is a technique for replicating micro- and nanometer structures using elastomeric materials, notably PDMS. Soft lithography is advantageous for prototyping compared to photolithography because of the relatively low cost. In its prepolymer form, PDMS can be cast over SU-8 devices and after curing can be gently peeled off to reveal a reusable “negative” mold with features that are accurately replicated across the design array (Figure 1). To create a reusable PDMS stamp, we explored numerous methods previously reported [9-12] for surface modification of the PDMS mold to achieve a non-sticking behavior which would allow PDMS-PDMS casting. Spontaneous adhesion between the PDMS mold and the PDMS prepolymer during the curing process results in fusion of the two PDMS layers. We found the combination of oxygen plasma activation follow by silanization of the PDMS mold surface to be the most consistent process. The treated PDMS mold was used three times without need for additional surface modification. In addition, using a 10:1 ratio of PDMS prepolymer to curing agent to create the PDMS mold and a 5:1 ratio for the casted PDMS gave the best results. Finally, while PDMS curing is typically performed for 2 hours at 65°C, we used a partial curing time of 1 hour at 65°C. This seemed to be the right balance between curing and preventing fusion of the two PDMS layers. Once the two PDMS layers were peeled apart, the newly formed PDMS replica was returned to the oven for 1 hour to ensure the curing process is complete. The dimensions of the SU-8 master mold were translated well during all soft lithography steps (Figure 2A). Due to the compression resistance and thermal stability (up to 200°C) of PDMS, the final PDMS replica could be used repeatedly for hot embossing plastics without compromising the micron-scale features.

To translate the micropillar features from the newly formed PDMS stamp replica to PS sheets, we employed a simple and low-cost method for hot embossing. Device fabrication via hot embossing uses mechanical force and two closely fitting die halves to press a plastic sheet to the desired form. In our case, we used the PDMS stamp sandwiched between two microscope slides in the place of the die halves. The sandwich assembly was clamped together by two 1” binder clips, which applied the force required for hot embossing (Figure 1). An oven was heated to 115°C, just above the glass transition temperature commonly reported for PS (approximately 100°C). The micropillar dimensions (250 µm width and 250 µm depth) were chosen to meet the depth-to-width ratio recommended for drape forming over a male mold [13], which is similar in principle to hot embossing. There were no signs of the PDMS micropillars leaning under pressure.

3.4 Results and Discussion

Device and culture characterization

Figures 2B shows the microwell pattern in PS following the hot embossing process in which microtissues can be formed with multiple cell-substrate and cell-cell interactions. For the purposes of studying the cell-on-cell hypothesis, the walls of the microwells were designed to be 100 µm in width to allow cell adhesion. Ideally, this would serve as a model for cell interactions with flat tissue culture dishes, which could be compared to the cell interactions within the adjacent microwell. The microwell width and depth were both designed to be 250 µm to ensure the features were large enough for the fabrication process. Although oxygen can diffuse across 100 - 200 µm of tissue thickness, it is advisable to limit tissue size to approximately 250 µm diameter to prevent hypoxic conditions [14].

The embossed PS sheets showed good replication from the PDMS stamps as revealed by phase contrast imaging (Figure 2A and B). Inspecting the dimensions of the PDMS stamp micropillars and the PS sheet microwells using phase contrast images and the image processing software ImageJ, the PDMS stamp features showed good replication of the original SU-8 dimensions (Figure 2A). However, ImageJ analysis of the PS microwells show an increase in size compared to the PDMS micropillars (Figure 2B). Furthermore, the bottom widths of the PS microwells appear smaller than the top widths, despite the fact drafting was not used in the design. It should be noted this effect is not apparent with the PDMS stamp micropillars, which indicates this is an effect of the hot embossing process. This also indicates PDMS-PDMS casting is an effective method for accurately replicating micron-scale features if care is taken to avoid fusion of the two PDMS layers. Design for manufacturability guidelines (e.g., [13]) recommend avoiding sharp corners and rectangular shapes because they hamper the flow of the material and are difficult to replicate for manufacturing processes such as thermoforming and injection molding. These are considerations for future micro-feature designs intended for patterning thermoformable plastics like PS.

As a proof-of-concept, PS sheets were chemically welded to 6-well plates with chloroform. The well plate was incubated with 7.5 µg fibronectin in 250 µL phosphate-buffered saline (PBS) overnight at 4°C to promote cell adhesion to the PS microwells. Following the fibronectin treatment, the wells were washed three times with PBS and 500 µL of MRC-5 fibroblast cell solution (1,000,000 cells/mL) were added to each well of the 6-well plate. The cells were allowed 4 hours to attach, then the 6-well plate was topped off with medium. Figure 3A and B demonstrate the proof-of-concept for microtissue formation within the microwells.

Translation to a manufacturable product

PDMS-based hot embossing of PS presented here demonstrates a simple process that can be used in regular laboratory settings. However, the microwell design concept in a multiwell plate format has the potential to be translated to a tangible product, by taking advantage of rapid injection molding commonly used to make multiwell plates for cell culture. Embossed and thermoformed plastic parts lack the dimensional accuracy of injection-molded parts. A number of factors contribute to this: low-pressure nature of embossing/thermoforming reduces the degree to which the sheet being formed is forced to conform to the molds, and sheet-material variations, chiefly in the thickness of the sheet, affect the final accuracy of the part. Hot embossing lends itself to low-quantity production while pressure, time and temperature variation affect final part dimensions, of these factors evenness of heating the sheet before forming is perhaps the most important. Rapid injection molding, however, enables high throughput manufacturing of thermoformable plastics while maintaining tight tolerances and high reproducibility [15, 16]. Although this approach to manufacturing is associated with low costs per device, it requires a large initial investment for the high-quality steel and precision milling required to create the complex molds. This makes rapid injection molding out of reach for most academic budgets which seldom require the need to fabrication hundreds of thousands of devices. However, considering the potentially relevant application a down-scaled 96-well plate format for HTS assays, this type of investment could be worthwhile for companies that are already heavily invested in the production of cell culture products.

The fabrication process described here simplifies the existing approach to hot embossing of plastics and can be used regularly in laboratory and prototyping settings. We describe an approach that prevents the fusion of PDMS layers so that PDMS-PDMS casting can be achieved. We also demonstrate that simple binder clips can generate enough force to translate micron-scale patterns from a PDMS stamp to PS sheets. Although the hot embossing process described here is sufficient for prototyping, we speculate that these cell culture platforms can be manufactured in a high throughput setting using rapid prototype injection.

3.5 References

1. Discher, D.E., P. Janmey, and Y.L. Wang, Tissue cells feel and respond to the stiffness of their substrate. Science, 2005. 310(5751): p. 1139-43.

2. Cheng, K., Y. Lai, and W.S. Kisaalita, Three-dimensional polymer scaffolds for high throughput cell-based assay systems. Biomaterials, 2008. 29(18): p. 2802-12.

3. Wang, L., et al., SU-8 microstructure for quasi-three-dimensional cell-based biosensing. Sensors and Actuators B: Chemical, 2009. 140(2): p. 349-355.

4. Dy, A.J., et al., Fabricating microfluidic valve master molds in SU-8 photoresist. Journal of Micromechanics and Microengineering, 2014. 24(5): p. 057001.

5. Taylor, A.M., S.W. Rhee, and N.L. Jeon, Microfluidic chambers for cell migration and neuroscience research, in Microfluidic Techniques. 2006, Springer. p. 167-177.

6. Wang, Y., et al., Surface graft polymerization of SU-8 for bio-MEMS applications. Journal of Micromechanics and Microengineering, 2007. 17(7): p. 1371.

7. Voskerician, G., et al., Biocompatibility and biofouling of MEMS drug delivery devices. Biomaterials, 2003. 24(11): p. 1959-1967.

8. Inoue, M., et al., Cell culture on MEMS materials in microenvironment limited by a physical condition. Micro & Nano Letters, 2012. 7(8): p. 725-728.

9. Yu, H., et al., Soft lithography replication based on PDMS partial curing. Microsystem technologies, 2011. 17(3): p. 443.

10. Lopera, S. and R. Mansano, Plasma-based surface modification of polydimethylsiloxane for PDMS-PDMS molding. ISRN Polymer Science, 2012. 2012.

11. Chen, X., et al., A facile and simple high-performance polydimethylsiloxane casting based on self-polymerization dopamine. Journal of Micromechanics and Microengineering, 2014. 24(9): p. 095006.

12. Wang, J., et al., Optimal protocol for molding PDMS with a PDMS master. Chips & Tips (Lab on a Chip), 2010. 6.

13. Bralla, J., Design for manufacturing handbook, 1998. McGraw-Hill, New York.

14. Griffith, L.G. and M.A. Swartz, Capturing complex 3D tissue physiology in vitro. Nature reviews Molecular cell biology, 2006. 7(3): p. 211-224.

15. Piotter, V., et al., Injection molding and related techniques for fabrication of microstructures. Microsystem Technologies, 1997. 3(3): p. 129-133.

16. You, B.H., et al. Assembly Tolerance Analysis for Injection Molded Modular, Polymer Microfluidic Devices. in ASME 2008 International Mechanical Engineering Congress and Exposition. 2008. American Society of Mechanical Engineers Digital Collection.

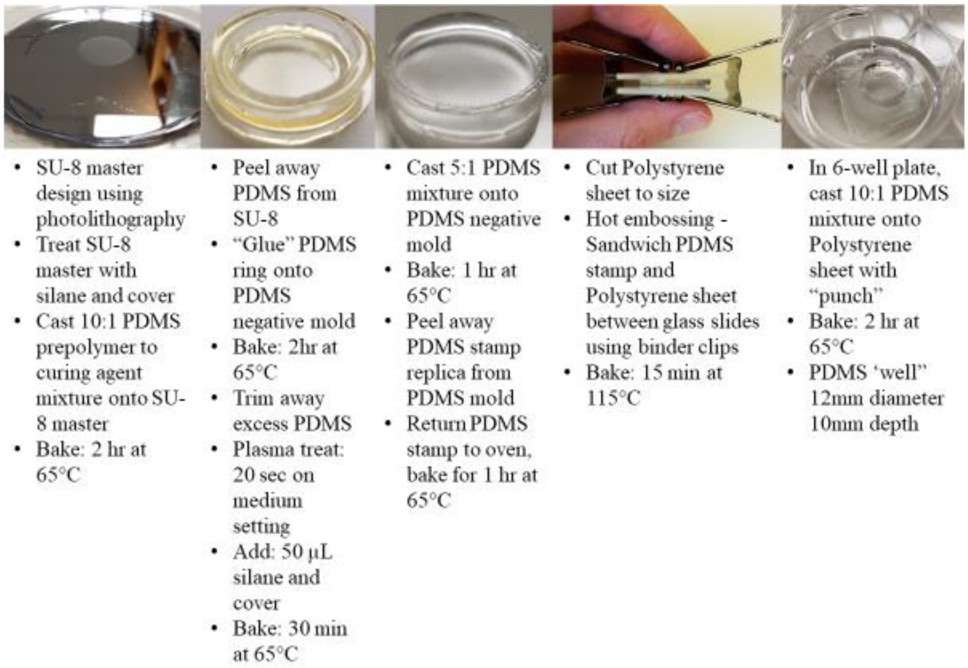

- SU-8 master design using photolithography
- Treat SU-8 master with silane and cover
- Cast 10:1 PDMS prepolymer to curing agent mixture onto SU-8 master
- Bake: 2 hr at 65°C

- Peel away PDMS from SU-8
- “Glue” PDMS ring onto PDMS negative mold
- Bake: 2hr at 65°C
- Trim away excess PDMS
- Plasma treat: 20 sec on medium setting
- Add: 50 μL silane and cover
- Bake: 30 min at 65°C

- Cast 5:1 PDMS mixture onto PDMS negative mold
- Bake: 1 hr at 65°C
- Peel away PDMS stamp replica from PDMS mold
- Return PDMS stamp to oven, bake for 1 hr at 65°C

- Cut Polystyrene sheet to size
- Hot embossing - Sandwich PDMS stamp and Polystyrene sheet between glass slides using binder clips
- Bake: 15 min at 115°C

- In 6-well plate, cast 10:1 PDMS mixture onto Polystyrene sheet with “punch”
- Bake: 2 hr at 65°C
- PDMS ‘well” 12mm diameter 10mm depth

Figure 3.1: Schematic of microwell platform fabrication.

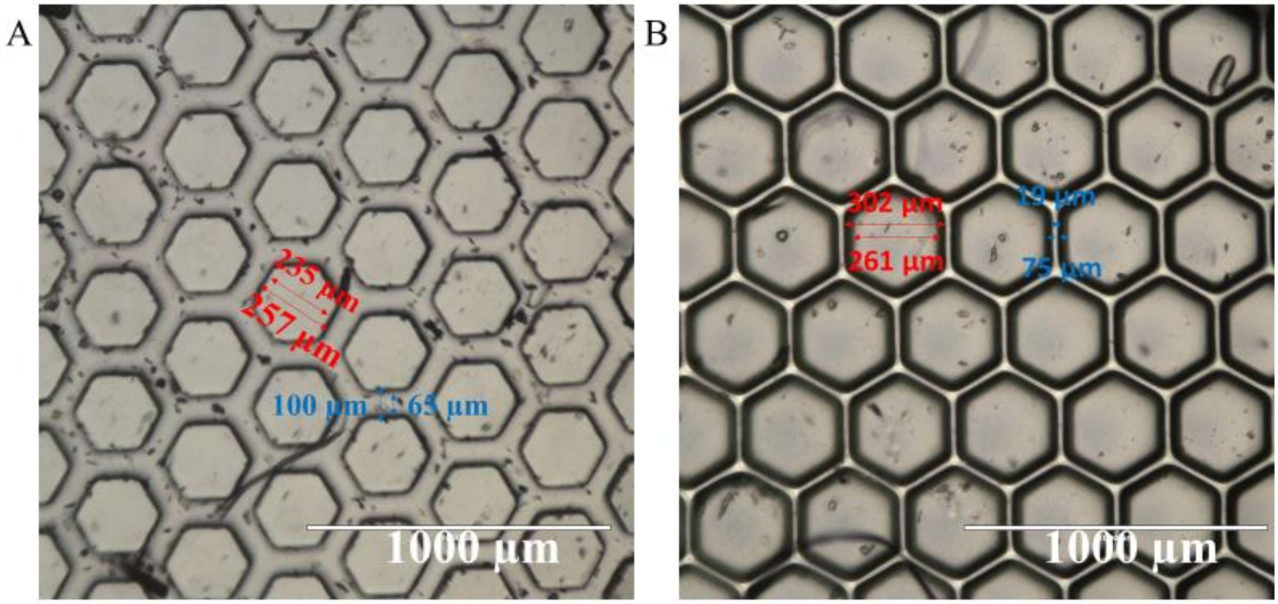

Figure 3.2: Replicas created using PDMS-PDMS casting (A) and hot embossing (B) show good translation of micron-scale features. (A) The micropillar features of the PDMS stamp (257 µm ± 3 µm, n = 15) and the spacing between the PDMS stamp micropillars (100 µm ± 4 µm, n = 15) were close replicates of the designed SU-8 master mold (250 µm and 100 µm, respectively). (B) The microwell features of the PS sheets were on average larger than the features on the PDMS stamp. The bottom width of the microwell appears to be smaller than the top width, which could indicate interference of PS flow around the right-angle features during hot embossing.

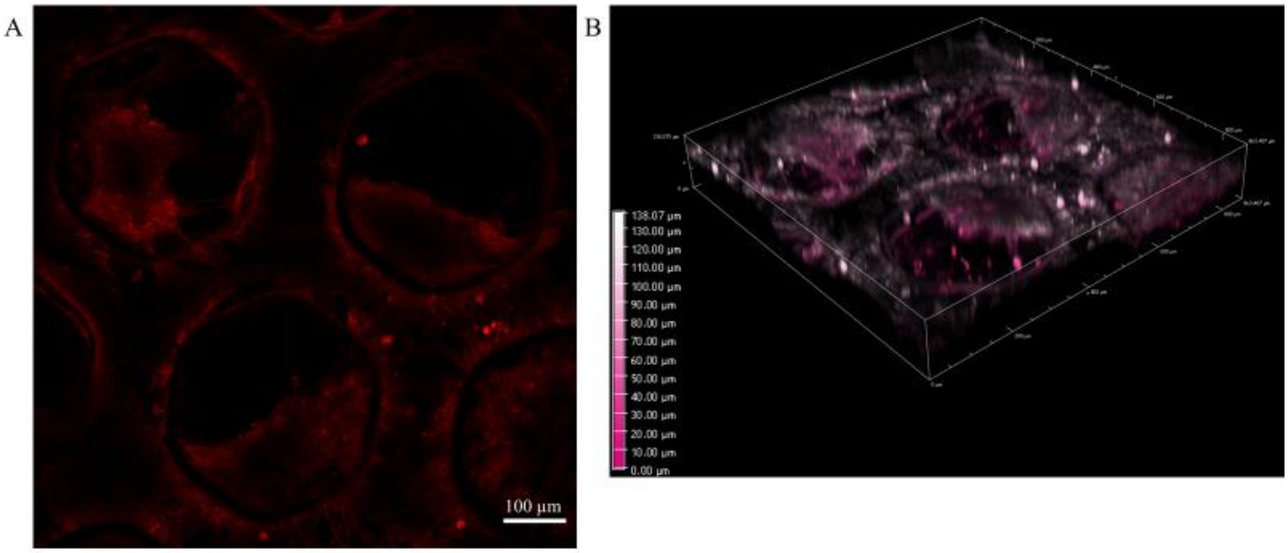

Figure 3.3: Confocal microscopy image of MRC-5 fibroblast culture stained with plasma membrane-specific dye CellMask Orange. (A) Microtissue formation and numerous cell-substrate interactions provides an opportunity to study the cell-on-cell hypothesis. (B) 3D reconstruction of z-section acquisitions shows cell adhesion within the microwells in addition to around the circumference of the microwells and across the walls between microwells. Color scale bar represents z-axis depth. Dark pink signal in the image indicates cell adhesion within the microwells.

CHAPTER 4

VISCOSITY IMAGING OF FIBROBLASTS AND THEIR ADAPTATION TO SUBSTRATE COMPLIANCE[3]

---

[3] White, C. M., Reese, A., Xu, B.Q., Haidekker, M. A., and Kisaalita, W. S. To be submitted to ACS Biomaterials Science and Engineering

4.1 Abstract

Membrane viscosity is a key parameter in cell function and signaling, as it determines molecular mobility. The purpose of this study is to assess fluorescence quantum yield of membrane-compatible, viscosity-sensitive fluorophore FCVJ, which belongs to a family of fluorescent probes termed molecular rotors. MRC-5 lung fibroblast deformability and morphology were investigated when grown on substrates with different rigidities. A more rigid substrate induced a state of lower deformability and increased cell area. FCVJ fluorescence was imaged using confocal microscopy and evaluated. FCVJ fluorescence generally increases when fibroblasts are grown on stiffer substrates, indicating an increase in membrane viscosity and a decrease in free volume. Trends in the FCVJ data among cells growing on the same substrate were also observed. We speculate on the significance of these observations and make the case that in dynamic, heterogenous systems like the cell membrane, a non-ratiometric approach to quantum yield-based measurements is not suitable, underscoring the need to improve ratiometric, dual-emission molecular rotor design.

4.2 Introduction

The biophysical signals experienced by cells greatly influence cellular and subcellular functions, including cell adhesion [1], migration [2], and differentiation [3]. Mechanotransduction, the process through which cells convert a mechanical stimulus to biochemical signals, is critical to the homeostasis of adult tissues and organs. The cell biomechanics are primarily determined by the cytoskeleton, the cell membrane, and the cytoplasm and is measured as “deformability” or “fluid properties”. Deformability is typically used to define the “elastic modulus”, where a force is applied to the cell and information, conventionally linked to the meaning of “stiffness”, can be extracted from the data. Fluid properties (also defined as fluidity or its inverse, viscosity) is typically used to define the diffusion (translational and/or rotational) of membrane constituents. The increased focus on cellular biomechanical properties has revealed that disparities in membrane viscosity are linked to diseases such as diabetes [4, 5], hypercholesterolemia [6], Huntington disease [7], and Alzheimer's disease [8-10] while changes in cell deformability is a hallmark for metastatic cancer [11, 12].

Numerous methods have been developed to measure cell mechanical properties, but each have important limitations. Atomic force microscopy and micropipette aspiration are some of the most widely used methods to probe deformability of single cells at nanoscale resolutions by applying nanoindentation, shear stresses, and pressure gradients. However, intrinsic variability in these techniques, such as probe geometry [13] and the models used to derive the quantitative mechanical properties [13, 14], make comparisons across studies difficult [15]. Furthermore, membrane viscosity must be extrapolated as a function of external physical parameters. Non-invasive elastography techniques like fluorescence recovery after photobleaching (FRAP) and fluorescence anisotropy are popular alternatives to estimate local membrane viscosity, but both rely on the diffusivity of specific fluorophores and local viscosities can only be approximately determined.

A family of fluorescent molecules, referred to as molecular rotors, exhibit free volume-dependent fluorescence quantum yield and have recently been explored as an alternative approach to assess membrane viscosity [16]. More specifically, the quantum yield ϕ_F depends on the local microviscosity η following the Förster - Hoffmann equation [17]

$$\phi_F = \phi_0 * \left(\frac{\eta}{\sigma}\right)^x \tag{1}$$

where ϕ_0 is the dye's intrinsic quantum yield, σ is a dye-specific constant, and x depends on both the dye and solvent. Molecular rotors, also known as twisted intramolecular charge transfer (TICT) complexes, have two competing deexcitation pathways that forms the basis for viscosity sensing: upon photoexcitation it assumes the twisted state with subsequent nonradiative deexcitation, or it emits a photon (Figure 1). In microenvironments with higher viscosity, photon emission is the preferred deexcitation pathway and thus the quantum yield increases. This relationship holds true in macromolecule systems (which includes the lipid bilayer) and was experimentally provided by Doolittle et al. [18].

The purpose of the work reported herein was to explore, as a first step, the potential of molecular rotors in reporting local viscosity of the cell membrane for cells grown on 2D substrates. We use polyacrylamide (PA) gels as a culture substrate to induce the mechanotransduction behavior of MRC-5 fibroblasts. AFM is used to confirm PA gel stiffness induces an increase in the cortical stiffness of the cell, which is reflected by an increase in cell area. We hypothesized that the plasma membrane is stretched, thus increasing its free volume, to accommodate the changes in cortical stiffness and increased cell area. Molecular rotors can report free volume (and related, viscosity) of the immediate surroundings in real time, require relatively simple steady state instrumentation, and their spatial resolution is only limited by the optical system.

4.3 Materials and Methods

MRC-5 Fibroblast Cell Culture

MRC-5 human lung fibroblast cells (CCL-171, ATCC, VA) were routinely cultured in 75 cm^2 tissue culture flasks in Eagle's Minimum Essential Medium containing 10% heat inactivated fetal bovine serum and were maintained at 5% CO^2 and 37°C. For seeding on polyacrylamide gels, cells were counted using a hemocytometer and 8 x 10^3 cells (in 300 µL medium) were added to each gel. After allowing 4 hours for attachment, acrylamide gels were transferred to 6-well plates and fresh growth medium was added to make the total volume 3 mL in each well.

Polyacrylamide (PA) gel fabrication

Polyacrylamide (PA) gels were fabricated following a modified method inspired by [19]. In brief, 22 mm square coverslips were soaked in 100% ethanol and flamed in a Bunsen burner, then placed in a coverslip rack. The coverslips were immersed in a 0.5% (3-Aminopropyl)trimethoxysilane (3-APTMS) solution. After 30 minutes, the coverslips were washed in three changes of ddH2O and allowed to dry. The coverslips were then immersed in 0.5% glutaraldehyde for 30 minutes followed by three wash steps with ddH$_2$O and allowed to dry. Acrylamide (5% or 3%) and bis-acrylamide (0.3%, 0.15%, and 0.075%) solutions were mixed with 1X PBS and polymerized using ammonium persulfate and N,N,N',N'-Tetramethylethylenediamine. A 30 µL drop of solution was distributed onto a glass slide treated with Rain-X and an activated 22 mm square coverslip was placed on top. After polymerization, the square coverslip was carefully removed and the gel was rinsed multiple times with PBS. 200 µL of 2.03 mM sulfosuccinimidyl 6-(4'-azido-2'-nitrophenylamino)hexanoate (sulfo-SANPAH) in 20 mM HEPES (pH 8.5) was pipetted onto the gel surface and exposed to UV light for 8 minutes. The sulfo-SANPAH solution was then removed, the gels rinsed with 20 mM HEPES (pH 8.5), and the process was repeated. Following photoactivation, the gels were rinsed twice in 20 mM HEPES (pH 8.5). A 100 µg/mL fibronectin solution in 20 mM HEPES (pH 8.5) was added to the gel surface and allowed to react for 6 hours at 4°C. After washing several times with PBS, the gels were ready for cell culture and stored under humid conditions united needed.

Fibronectin-coated polyacrylamide gels were indented using AFM in contact mode and the Hertz model was used to infer Young's moduli from the resulting force-indention curves.

Atomic force microscopy measurements

Atomic force microscopy (AFM) was used to estimate the stiffness (Young's modulus, E) of cells and the polyacrylamide gels to which they were adhered. AFM elasticity measurements were performed in Hank's Balanced Salt Solution (with calcium, magnesium, glucose) (gibco) supplemented with 25 mM HEPES (gibco) using an Aglient 5500 AFM (Aglient/Keysight, Chandler, AZ) coupled to an Olympus inverted light microscope operated in contact mode with the cantilever tip submerged in the solution within a PTFE liquid cell designed for the instrument. Experiments were conducted with an Aspire CCS conical contact mode short cantilever tip (nanoScience Instruments Store) with a length of 225 µm, a nominal tip radius of 8 nm, a cone angle of 30° and a spring constant of 0.0439 N/m. The spring constant was calibrated using the thermal tuning method [20]. The system was positioned so that the tip was located on top of a chosen cell. The PA gel immediately adjacent to the cell was also probed. Measurements were made in closed-loop mode. The applied force was 8 nN in order to maintain the deformation of the substrate and cell of interest within the linear elastic regime, allowing us to use the Hertz model. Typically, 10 - 20 AFM measurements were made per cell or polyacrylamide region of interest.

To estimate the local average Young's modulus of a cell and its PA substrate, the Hertz model was fitted to the first 100 - 200 nm of tip indentation using the Hertz Fit Application [21] created by Holger Doschke and Manfred Radmacher of the Institute of Biophysics at the University of Bremen (Bremen, Germany) (Supplementary Figure 1). Young's modulus relates an applied strain (uniaxial deformation) to the resulting stress. The Poisson ratio was taken to be 0.5 for all samples, which is consistent with other AFM studies on mammalian cell culture [22, 23].

PDMS Stamp Design and Fabrication

Conventional photolithography was used to create an SU-8 master mold on a silicon wafer, which was then silanized with chlorotrimethylsilane to aid the release of PDMS from the master. PDMS prepolymer (Sylgard 184, Dow Corning) was cast on the mold and left to cure in an oven for 2 hours at 65°C. After curing, the PDMS was stripped from the mold and bonded to a PDMS ring with small amounts of PDMS prepolymer. This PDMS “negative” mold was then used as a template for creating a PDMS stamp replicate of the SU-8 master. PDMS-PDMS casting was made possible by plasma-activated silanization. Briefly, the PDMS “negative” mold was plasma oxidized for 20 seconds (Plasma Cleaner PDC-32G, Harrick Plasma) then placed in an oven at 65°C with three drops of chlorotrimethylsilane covered with a Petri dish immediately afterward. The PDMS “negative” was then placed in a Petri dish molded side up and PDMS mixture (5:1 base to curing agent) was poured to fill the entire mold. This was placed in vacuum to eliminate air bubbles, then cured at 65°C for 1 hour. The flexibility of the PDMS allowed for the PDMS “replicate” stamp to be easily peeled away from the PDMS “negative” mold, after which the PDMS stamp was returned to the oven for 1 hour.

Hot Embossing Polystyrene with PDMS Stamp

Polystyrene microwells were created via a user-friendly, quick and low-cost hot embossing process utilizing a PDMS stamp and a PS sheet (evergreen scale models sheet styrene; 0.4 mm thick). Briefly, 22 mm square pieces were cut from the PS sheet. The PDMS stamp and square PS piece were sandwiched between two 25 x 75 x 1 mm glass microscope slides. Two 1” wide binder clips were used to hold the sandwich together and apply the pressure necessary for hot embossing. The sandwich was placed in an oven at 115°C for 15 minutes. With the binder clips still clamped to the slides, the whole assembly was cooled to room temperature. Once cooled the PDMS stamp can be carefully peeled away from the PS sheet.

Microwell plate fabrication and characterization

6-well plates were placed on a hot plate set to 80°C while a 10 mm metal punch was placed in an oven and heated to 260°C. The hot punch was used to create a 10 mm diameter hole in the center of each well. A square 22 mm PS microwell sheet was then chemically welded to the bottom of each well with chloroform. Then, 10 mm plastic tubes were cut to size and used as a scaffold while PDMS prepolymer (10:1 base to curing agent) was poured around the tube to create a 10 mm well. PDMS prepolymer was cured at 65°C for 2 hours. The tube was carefully removed. PS microwells were then sterilized with isopropyl alcohol for 30 minutes then exposed to UV in a biosafety cabinet overnight to ensure sterility. Fibronectin solution (7.5 µg in 250 µL PBS) was added to each well and incubated at 4°C overnight. PS microwells were rinsed twice with 1 mL PBS then incubated at 37°C for 1 hour in cell culture medium prior to adding cells.

General procedure for cell culture staining and imaging

A 5 mM stock solution of FCVJ (Figure 1) in ethanol was prepared and was then diluted and used at a final concentration of 100 µM in appropriate growth medium. After a 10 minute incubation, the cells were washed twice with PBS++ then incubated with CellMaskTM Orange plasma membrane stain (Invitrogen) in growth medium for 10 minutes. The cells were washed twice with PBS++ then incubated with Hoechst 33342 in PBS++ for 5 minutes. Cells were imaged live in Hank’s Balanced Salt Solution (with Mg, Ca, glucose, no phenol red, Gibco) using a Nikon A1R confocal microscope system, Nikon Eclipse Ti-E inverted microscope with

CFi Plan Fluor 40x oil objective (NA 1.30 WD 0.20 mm) controlled by NIS-Elements software (Nikon, Melville, NY).

Image Processing and Analysis

Image analysis of cells stained with FCVJ and CellMask Orange was performed using the Crystal Image Software. To isolate FCVJ fluorescence from the plasma membrane, the membrane-specific dye CellMask Orange was used to create a binary mask. To create the mask, preprocessing steps were performed on the CellMask Orange image. First, a Gaussian filter was applied to smooth the image and reduce noise. The background signal was then subtracted. The CellMask Orange signal from the plasma membrane was then detected by thresholding, which results in a binary image where the background is forced to a pixel value of 0 and the stained structures have a pixel value of 1 (e.g., Figure 5C and F). The preprocessing steps were performed to reduce the amount of noise in the image so a lower threshold, which detects more structures but has a harder time of distinguishing between object and non-object pixels, can be used. The original images of FCVJ and CellMask Orange were then multiplied by the binary mask, resulting in a 16-bit image where the membrane signal has a pixel range from 0 - 65,535 and all other signal is forced to 0. For each cell, the mean intensity of five regions of interest (ROI) were averaged, and the data was presented as an intensity ratio of FCVJ / CellMask Orange.

4.4 Results

MRC-5 fibroblast morphology and apparent Young’s modulus depends on substrate compliance

In this work, five polyacrylamide (PA) gels with unique stiffness values (Figure 2) were used for cell culture, which we refer to as “soft” (0.4, 1.9, 3.6 kPa) and “stiff” (10.5, 25 kPa).

The attachment and morphology of MRC-5 fibroblasts were monitored for the first 12 hours post-seeding. Although a majority readily and homogenously adhered to PA gels within the first four hours as individual cells, some were observed to be unattached and aggregating at the gel surface (images not shown). These aggregates were gently washed away with medium when the gels were transferred to 6-well plates. After 12 hours, cell morphology was observed using phase-contrast imaging (Figure 3). Figure 4A shows the difference in cell area as a function of substrate compliance. Fibroblast area increased almost three-fold when grown on stiffer substrate (10 kPa; ~ 3100 μm^2) compared to soft (400 Pa; ~ 800 μm^2). Fibroblasts were well spread and appeared indistinguishable between the 10 kPa and 25 kPa gels and more rigid substrates like tissue culture plastic and glass (Figure 3).

To establish the effect of substrate compliance on fibroblast stiffness, AFM was used to obtain force indentation curves from which apparent Young’s modulus (E) was extracted using a modified Hertz equation [21, 23]. For each probed cell the PA gel directly adjacent to the cell was measured, allowing us to account for any local variations in substrate stiffness. For fibroblasts growing on the stiffest gel and therefore the most spread out, tapping mode AFM determined cell height at the cell edge was approximately 1 - 2 µm. Generally, AFM indentations larger than 10% of the cell thickness are influenced by the underlying substrate. Therefore, the first 100 - 200 nm of indentation was used to estimate fibroblast Young’s modulus. A global trend of cell stiffness increase with substrate stiffness as measured by AFM was observed (Figure 4B). Fibroblast stiffness was lower than that associated substrate stiffness, except those grown on the softest gel, which had an average stiffness of 4.1 ± 1.3 kPa.

Figures 4A and B indicate a correlation between fibroblast stiffness and cell area. An increase in average cell stiffness from 1 to 4.5 kPa (for gels with average stiffness ranging 1.5 -

10 kPa) was associated with an increase in area from 1017 to 3124 μm^2. A slight increase in cell stiffness from 4.5 to 7 kPa was observed for gels with stiffness of 10 and 25 kPa, respectively, with little increase in cell area (Figure 4A and B).

Viscosity imaging of fibroblasts with molecular rotor FCVJ

Validation of FCVJ viscosity sensitivity and the associated change in fluorescence emission intensity was performed in mixtures of methanol : glycerol and presented in Supplementary Figure 2. Fibroblasts cultured and stained on PA gels were imaged using confocal microscopy. Although the plasma membrane was the target organelle for this dye, confocal microscopy revealed internal membranes and the cytosol were also fluorescently stained (Figure 5A and D). The addition of commercially available dye CellMask Orange was used to identify the plasma membrane (Figure 5B and E). All samples were stained at the same time to avoid variability in staining solution concentrations and incubation times, but only one sample could be imaged at a time. Punctate features stained with CellMask Orange observed later in time (Figure 5E) compared to early in time (Figure 5B) show an internalization of membrane, presumably due to endocytosis. We speculate this could be the case for FCVJ as well, although strong FCVJ fluorescence was observed soon after staining (Figure 5A).

The two dye intensities, viscosity-sensitive FCVJ and viscosity-insensitive CellMask Orange, were used as a ratio pair for fluorometric determination of membrane microviscosity. Binary masks (Figure 5C and F) were created using CellMask images and multiplied by the original FCVJ and CellMask images to isolate plasma membrane fluorescence (see Materials and Methods). The FCVJ and CellMask intensity ratios were measured at eight regions of interest (ROIs) per cell, which allowed us to observe potential variability in intensity among cells grown on the same gel substrate (Figure 6). Interestingly, some trends in the data could be inferred. As an example, a decrease in intensity for cells growing on the softest gel (0.4 kPa) with an increase in area was noticeable. Remarkably, the opposite trend was noted for cells growing on stiffer gel substrates (3.6, 10.5 and 25 kPa) (Figure 6). Plotting cell area versus ratiometric intensity (Figure 7) shows an increase in cell area for cells grown on stiffer substrate, much like the trend observed with phase contrast imaging (Figure 4A) and a general increase in fluorescence intensity for cells growing on gels within the physiological stiffness range of healthy (~1.8 - 7 kPa) and diseased (~10 - 25 kPa) lung.

4.5 Discussion

Figures 3 and 4 demonstrates the correlation between cell morphology and the compliance of the substrate on which the cells are grown. Our results show that within a range of soft substrates (1 to 20 kPa) cell area increases. Although a substrate stiffness within the range of 20 - 30 kPa can still be considered physiologically relevant, most adherent cell types reach a constant or saturated spread area around 20 kPa, with morphology being relatively indistinguishable between stiffer gels (20 - 30 kPa) and physiologically irrelevant materials such as tissue culture plastics and glass [24]. In addition, cell cortical stiffness gradually increases from 1 to 7 kPa when grown on physiologically relevant substrates. These results are in agreement with previous studies that report cell stiffness is influence by both substrate stiffness and cell area [25-27]. A slight increase in cell stiffness from 4.5 to 7 kPa was observed for gels with stiffness of 10 and 25 kPa, respectively, with little increase in cell area (Figure 4A and B). This can be attributed to thicker, more organized cytoskeleton fibers that form when substrate compliance increases past the physiologically relevant range [24].

The exception to this relationship was the measured stiffness of fibroblasts (4.1 ± 1.3 kPa) growing on the softest (400 Pa) PA substrate. Although our best efforts were made to probe the cell body between the nucleus and cell edge, we believe the location of measurement was not always consistent to where we attempted to locate the probe. This was evident by occasional drifting of the AFM probe upon approach of the specimen. Considering the small spread area (~ 800 µm^2) of fibroblasts growing on soft PA gels, we speculate the apparent Young's modulus values were influenced by the cell nucleus. This does not mean in our case the nucleus was directly measured. The cell nucleus has a reported apparent Young's modulus of 5 kPa [15, 28]. Abidine and colleagues reported an apparent Young's modulus of 3 kPa over the nuclear region, attributing the lower value as an average of the nucleus, cytoplasm, and membrane effects [29].

For the purposes of this study, the actin-rich cortex is of the most interest because of its close interactions with the membrane. Evidence suggests that the sharp-tip conical probe we used in this study emphasizes cortical properties, while round-tip probes emphasize the non-cortical intracellular network [30]. At short time scales and small deformations, the cell is elastic (solid elastic sphere model) where a characteristic Hertz model upon indentation is appropriate. The force curves obtained in this study were analyzed in terms of a modified Hertz model to obtain Young's modulus; however, considering this model does not account for viscous effects of the cell response to deformation, we consider our results apparent Young's modulus. The approach curves were used to avoid any adhesion effects between the tip and the glycocalyx or glycoproteins that might be present in the retract curve.

We hypothesized that with an increase in cell area the plasma membrane adopts a stretched condition, in turn increasing the free volume of the lipid bilayer. Here we use the molecular rotor FCVJ, a free volume sensor, in an attempt to establish a link between membrane stretch and membrane free volume (i.e., viscosity). Molecular rotors with TICT excited states have already demonstrated their usefulness as viscosity probes for cellular organelles, including the plasma membrane of live cells [16, 31, 32]. Molecular rotors that exhibit TICT behavior are attractive because of their ability to react instantaneously (within 10 ns) to changes in the environment, allowing real-time measurements with high spatial and temporal resolution. Taking advantage of the farnesyl chain, known to improve solubility up to 10-fold, Haidekker and co-workers reported significantly higher affinity for cellular membranes for farnesyl derivatives of DCVJ and CCVJ [32]. To this end, molecular rotor FCVJ was selected to explore the potential relationship between the increase in cell area and apparent Young's modulus and hypothesized increase in cell membrane stretch (i.e., viscosity).

It is apparent that TICT molecular rotor FCVJ is not entirely specific to the plasma membrane, with strong intracellular fluorescence signal (Figure 5A and D). We attributed these stained components to endosomes or lipid droplets. Another study using a fluorescent compound with a farnesyl chain reported similar preferential localization for intracellular membrane-bound organelles [33]. Comparing the CellMask images of cells imaged immediately after staining (Figure 5B) to cells imaged later (Figure 5E) also indicates membrane remodeling activity. In addition, regions of lower intracellular fluorescence intensity are most likely the cell cytosol. We note that the plasma membrane localization of BODIPY-based molecular rotors was significantly improved with the addition of a double positive charge on a hydrocarbon chain [34]. Additional studies are required to determine if this modification is possible for our family of TICT molecular rotors.

In order to make localized measurements of the plasma membrane, we implemented a method for identifying FCVJ fluorescence from the plasma membrane by using the plasma membrane-specific fluorophore CellMask Orange. Through a series of image processing step, we were able to measure FCVJ plasma membrane by applying a binary mask to the original FCVJ and CellMask images. The result is a stacked image where the background and intracellular signals are assigned a pixel value of zero, thereby isolating the fluorescence signal from the plasma membrane. The intensity values for eight regions of interest (ROI) were recorded per cell, and a ratio of FCVJ over CellMask intensity was used. Assuming correlated fluorophore concentration, we believed this would serve as a suitable proxy for observing differences in viscosity between cells.

Although a clear relationship exists between cell stiffness and cell area when grown on stiffer substrates, the ratiometric intensity measurements of FCVJ and CellMask were more difficult to interpret (Figure 7). Considering our results depend on differences in FCVJ fluorescence intensity between cells on the same sample as well as cells on different samples, we made every attempt during sample preparation to eliminate external factors that might influence our results. This included staining all samples as the same time with the same staining solutions in the same environment. However, evidence indicates a continuous exchange of the plasma membrane [35], which means we cannot be certain the concentration of membrane-bound FCVJ is the same between samples. We attempted to account for the heterogenous concentration of FCVJ by using a fluorescence intensity ratio of FCVJ / CellMask Orange. However, the two dyes are not homologous, and the assumption of equal uptake is reasonable only if both dyes can be delivered by the same carrier/method of delivery, as was the case for Luby-Phelps et al. [36].

Comparing FCVJ data for cells growing on all 5 gels shows a slight decrease in fluorescence for very round cells with a shift to increasing fluorescence with cell areas larger than 775 μm^2 (Figure 7). This observation is even more apparent when fluorescence intensity among cells growing on the same substrate is compared (Figure 6). An apparent increase in fluorescence intensity with an increase in cell area would indicate the opposite of our hypothesis occurs. An increase in membrane free volume when cells become more spread out would favor the intramolecular rotation deexcitation pathway, which means we would see a decrease in fluorescence. However, we see the opposite, indicating that with an increase in cell area the membrane free volume decreases and membrane viscosity increases, which could be associated with an increase in membrane order.

Considering the MRC-5 lung fibroblast line was derived from normal lung tissue of a 14-week-old fetus and not a specific anatomical compartment of an adult human lung, we can only broadly speculate on the ‘physiologically relevant’ modulus. To study the role of matrix stiffness for normal and idiopathic pulmonary fibrosis lung and the associated pathological change in lung-derived fibroblasts, Marinković and colleagues used PA gels with modulus of 1 kPa as a model for healthy lung and 6 and 20kPa as a model for idiopathic pulmonary fibrosis lung [37]. Another study, using AFM to measure the modulus of tissue samples from three anatomical lung compartments (airways, vessels, and parenchyma), reported a mean elastic modulus of 15.76 kPa for airways, 7.17 kPa for vessels, and 1.87 kPa for parenchyma [38]. With this information, we believe our 1.9 and 3.6 kPa gels are well within the modulus range of normal lung tissue, while it could be argued our 10.5 and 25 kPa gels can be considered physiologically relevant to diseased lung tissue. Additionally, we can say with confidence our softest gel (0.4 kPa) is too soft for lung tissue and is therefore physiologically irrelevant to this cell line. We speculate the MRC-5 fibroblasts used in this study were struggling to adapt to the softest substrate which could be a contributing factor to the apparent negative trend in fluorescence intensity (Figure 6). Previous studies indicate some adherent cell lines have difficulty growing on soft substrates [39-42]. For the gel substrates within the modulus range of normal lung tissue, the intensity ratio did not change with cell area (1.9 kPa) or had a slightly positive trend (3.6 kPa). On the other hand, there was an obvious positive trend of fluorescence intensity with cell area for the gel substrates with moduli within the range of diseased lung tissues (10.5 and 25 kPa). This could indicate that fibroblasts growing on physiologically relevant substrates were well adapted with no significant changes to membrane properties, while substrates relevant to diseased lung tissue induced pathological changes associated with alterations in fibroblast membrane properties. Without a means for accounting for FCVJ and CellMask dye concentration, however, we can only speculate on the apparent trends in membrane viscosity.

4.6 Conclusions and Future Perspectives

Spatial variations in fluorophore concentration exist in many heterogenous systems but considering fluorophore concentration has a major effect on the measured fluorescence intensity, it is impossible to decouple the viscosity-relevant changes in rotor intensity and the spatial variations in concentration. Ultimately, this concentration uncertainty makes the determination of fluorescence intensity in cell culture impossible with the current experimental approach. Theoretically, fluorescence lifetime imaging microscopy (FLIM) is a possible alternative to steady-state instrumentation and the fluorescence lifetime of FCVJ can be useful where determining fluorescence quantum yield fails. Unlike fluorescence intensity, the lifetime does not change as a function of the fluorophore concentration. It is possible to invert equation 1 and solve for viscosity $\eta = \sigma \left({}^{\phi_F}\!/_{\phi_0}\right)^{1/x}$, but as we have reported in this manuscript the concentration uncertainty makes quantum yield ϕ_F in heterogenous systems like cell culture impossible to determine. However, using time-resolved spectroscopy or FLIM, we can substitute quantum yield with measured lifetime τ using the equation $\phi_F = \frac{\tau}{\tau_N}$ where τ_N is the fluorophore's natural lifetime (i.e., the lifetime where intramolecular rotation is inhibited and nonradiative deexcitation is absent). The disadvantages of using lifetime compared to steady-state measurements have been discussed previously [43, 44].

In such cases, viscosity measurements based on a more representative ratiometric intensity measurement are particularly useful. This was the justification for developing ratiometric TICT molecular rotors with a viscosity-insensitive reference fluorophore conjugated to a viscosity-sensitive molecular rotor [45, 46]. Simply put, the viscosity-insensitive fluorophore is used to determine the probe concentration, while the viscosity is determined by the fluorescence quantum yield of a molecular rotor. These ratiometric probes have the potential to “close the gap” where non-ratiometric molecular rotors like FCVJ fall short.

4.7 References

1. Tomakidi, P., et al., Focal adhesion kinase (FAK) perspectives in mechanobiology: implications for cell behaviour. Cell and tissue research, 2014. 357(3): p. 515-526.

2. Marzban, B., et al., A contraction–reaction–diffusion model: Integrating biomechanics and biochemistry in cell migration. Extreme Mechanics Letters, 2019. 32: p. 100566.

3. Sun, Y., C.S. Chen, and J. Fu, Forcing stem cells to behave: a biophysical perspective of the cellular microenvironment. Annual review of biophysics, 2012. 41: p. 519-542.

4. Nadiv, O., et al., Elevated protein tyrosine phosphatase activity and increased membrane viscosity are associated with impaired activation of the insulin receptor kinase in old rats. Biochemical Journal, 1994. 298(Pt 2): p. 443.

5. Osterode, W., C. Holler, and F. Ulberth, Nutritional antioxidants, red cell membrane fluidity and blood viscosity in type 1 (insulin dependent) diabetes mellitus. Diabetic Medicine, 1996. 13(12): p. 1044-1050.

6. Gleason, M.M., M.S. Medow, and T.N. Tulenko, Excess membrane cholesterol alters calcium movements, cytosolic calcium levels, and membrane fluidity in arterial smooth muscle cells. Circulation Research, 1991. 69(1): p. 216-227.

7. Sameni, S., et al., Alteration in fluidity of cell plasma membrane in Huntington disease revealed by spectral phasor analysis. Scientific reports, 2018. 8(1): p. 734.

8. Zubenko, G.S., et al., Platelet membrane fluidity individuals at risk for Alzheimer’s disease: a comparison of results from fluorescence spectroscopy and electron spin resonance spectroscopy. Psychopharmacology, 1999. 145(2): p. 175-180.

9. Kosicek, M. and S. Hecimovic, Phospholipids and Alzheimer’s disease: alterations, mechanisms and potential biomarkers. International journal of molecular sciences, 2013. 14(1): p. 1310-1322.

10. Walter, J. and G. van Echten-Deckert, Cross-talk of membrane lipids and Alzheimer-related proteins. Molecular neurodegeneration, 2013. 8(1): p. 34.

11. Cross, S.E., et al., Nanomechanical analysis of cells from cancer patients. Nature nanotechnology, 2007. 2(12): p. 780-783.

12. Remmerbach, T.W., et al., Oral cancer diagnosis by mechanical phenotyping. Cancer research, 2009. 69(5): p. 1728-1732.

13. Guz, N., et al., If cell mechanics can be described by elastic modulus: study of different models and probes used in indentation experiments. Biophysical journal, 2014. 107(3): p. 564-575.

14. Brückner, B.R. and A. Janshoff, Elastic properties of epithelial cells probed by atomic force microscopy. Biochimica et Biophysica Acta (BBA)-Molecular Cell Research, 2015. 1853(11): p. 3075-3082.

15. Wu, P.-H., et al., Comparative study of cell mechanics methods. Nature methods, 2018. 15(7): p. 491.

16. Haidekker, M.A., N. L'Heureux, and J.A. Frangos, Fluid shear stress increases membrane fluidity in endothelial cells: a study with DCVJ fluorescence. American journal of physiology. Heart and circulatory physiology, 2000. 278(4): p. H1401-6.

17. Förster, T. and G. Hoffmann, Die viskositätsabhängigkeit der fluoreszenzquantenausbeuten einiger farbstoffsysteme. Zeitschrift für Physikalische Chemie, 1971. 75(1_2): p. 63-76.

18. Doolittle, A.K., Studies in Newtonian flow. III. The dependence of the viscosity of liquids on molecular weight and free space (in homologous series). Journal of Applied Physics, 1952. 23(2): p. 236-239.

19. Fischer, R.S., et al., Stiffness-controlled three-dimensional extracellular matrices for high-resolution imaging of cell behavior. Nature protocols, 2012. 7(11): p. 2056.

20. Butt, H.-J. and M. Jaschke, Calculation of thermal noise in atomic force microscopy. Nanotechnology, 1995. 6(1): p. 1.

21. Haupt, P.D., Holger; Radmacher, Manfred. Data Analysis: Hertz Fit. 2013 November 10, 2017 [cited 2018 October 10]; Available from: http://www.biophysik.uni-bremen.de/start/radmacher-group/data-analysis/hertzfit/hertz-fit-credits/.

22. Mahaffy, R., et al., Quantitative analysis of the viscoelastic properties of thin regions of fibroblasts using atomic force microscopy. Biophysical journal, 2004. 86(3): p. 1777-1793.

23. Radmacher, M., Studying the mechanics of cellular processes by atomic force microscopy. Methods in cell biology, 2007. 83: p. 347-372.

24. Solon, J., et al., Fibroblast adaptation and stiffness matching to soft elastic substrates. Biophys J, 2007. 93(12): p. 4453-61.

25. Tee, S.-Y., et al., Cell shape and substrate rigidity both regulate cell stiffness. Biophysical journal, 2011. 100(5): p. L25-L27.

26. Han, S.J., et al., Decoupling substrate stiffness, spread area, and micropost density: a close spatial relationship between traction forces and focal adhesions. Biophysical journal, 2012. 103(4): p. 640-648.

27. Yeung, T., et al., Effects of substrate stiffness on cell morphology, cytoskeletal structure, and adhesion. Cell motility and the cytoskeleton, 2005. 60(1): p. 24-34.

28. Caille, N., et al., Contribution of the nucleus to the mechanical properties of endothelial cells. Journal of biomechanics, 2002. 35(2): p. 177-187.

29. Abidine, Y., et al., Mechanosensitivity of cancer cells in contact with soft substrates using AFM. Biophysical journal, 2018. 114(5): p. 1165-1175.

30. Vahabikashi, A., et al., Probe Sensitivity to Cortical versus Intracellular Cytoskeletal Network Stiffness. Biophysical journal, 2019. 116(3): p. 518-529.

31. Haidekker, M.A. and J.A. Frangos. Fluorescent molecular rotor for the study of membrane fluidity in endothelial cells under fluid shear stress. in BiOS 2000 The International Symposium on Biomedical Optics. 2000. International Society for Optics and Photonics.

32. Haidekker, M.A., et al., New fluorescent probes for the measurement of cell membrane viscosity. Chemistry & biology, 2001. 8(2): p. 123-131.

33. Levitt, J.A., et al., Membrane-bound molecular rotors measure viscosity in live cells via fluorescence lifetime imaging. The Journal of Physical Chemistry C, 2009. 113(27): p. 11634-11642.

34. López-Duarte, I., et al., A molecular rotor for measuring viscosity in plasma membranes of live cells. Chemical Communications, 2014. 50(40): p. 5282-5284.

35. Tanaka, M., et al., Turnover and flow of the cell membrane for cell migration. Scientific reports, 2017. 7(1): p. 1-13.

36. Luby-Phelps, K., et al., A novel fluorescence ratiometric method confirms the low solvent viscosity of the cytoplasm. Biophysical journal, 1993. 65(1): p. 236-242.

37. Marinković, A., F. Liu, and D.J. Tschumperlin, Matrices of physiologic stiffness potently inactivate idiopathic pulmonary fibrosis fibroblasts. American journal of respiratory cell and molecular biology, 2013. 48(4): p. 422-430.

38. Sicard, D., et al., Aging and anatomical variations in lung tissue stiffness. American Journal of Physiology-Lung Cellular and Molecular Physiology, 2018. 314(6): p. L946-L955.

39. Pelham, R.J. and Y.-l. Wang, Cell locomotion and focal adhesions are regulated by substrate flexibility. Proceedings of the National Academy of Sciences, 1997. 94(25): p. 13661-13665.

40. Georges, P.C. and P.A. Janmey, Cell type-specific response to growth on soft materials. Journal of applied physiology, 2005. 98(4): p. 1547-1553.

41. Engler, A.J., et al., Myotubes differentiate optimally on substrates with tissue-like stiffness. J Cell Biol, 2004. 166(6): p. 877-887.

42. Wang, H.-B., M. Dembo, and Y.-L. Wang, Substrate flexibility regulates growth and apoptosis of normal but not transformed cells. American Journal of Physiology-Cell Physiology, 2000. 279(5): p. C1345-C1350.

43. Haidekker, M.A. and E.A. Theodorakis, Ratiometric mechanosensitive fluorescent dyes: Design and applications. J Mater Chem C Mater, 2016. 4(14): p. 2707-2718.

44. White, C.M., M.A. Haidekker, and W.S. Kisaalita, Ratiometric Nanoviscometers: Applications for Measuring Cellular Physical Properties in 3D Cultures. SLAS TECHNOLOGY: Translating Life Sciences Innovation, 2020: p. 2472630319901262.

45. Yoon, H.J., et al., Synthesis and evaluation of self-calibrating ratiometric viscosity sensors. Org Biomol Chem, 2011. 9(9): p. 3530-40.

46. Nipper, M.E., et al., Detection of liposome membrane viscosity perturbations with ratiometric molecular rotors. Biochimie, 2011. 93(6): p. 988-994.

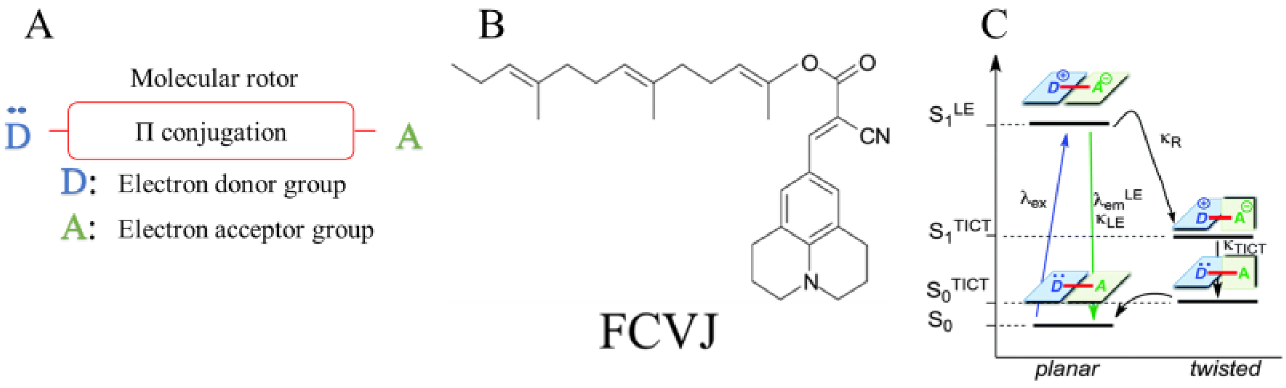

Figure 4.1: Generic motif of a molecular rotor (A) and the chemical structure of molecular rotor FCVJ (B). Jablonski diagram of a single emission (e.g., FCVJ) (C) molecular rotor. The electronic states are organized vertically by energy and horizontally by spin multiplicity. Radiative transitions involve the absorption, if the transition is to a higher energy level, or in the reverse case, emission of a photon, and are represented by colored arrows. Nonradiative transitions are indicated by black arrows.

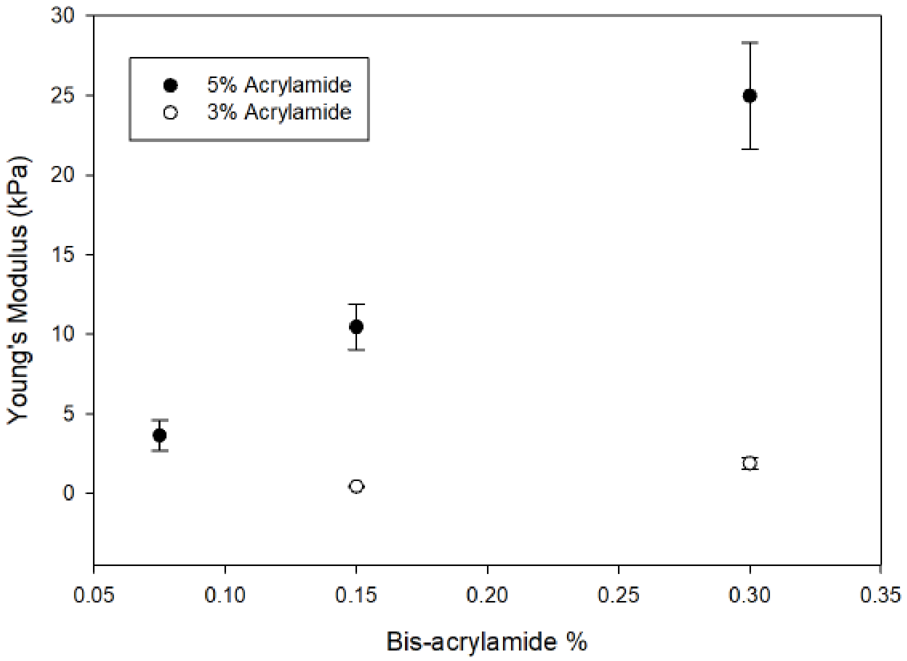

Figure 4.2: Polyacrylamide (PA) gel stiffness as a function of bis-acrylamide crosslinker concentration. Different mixtures of acrylamide and bis-acrylamide crosslinker allowed for a wide range of Young's modulus outcomes. Young's modulus was consistent batch-to-batch.

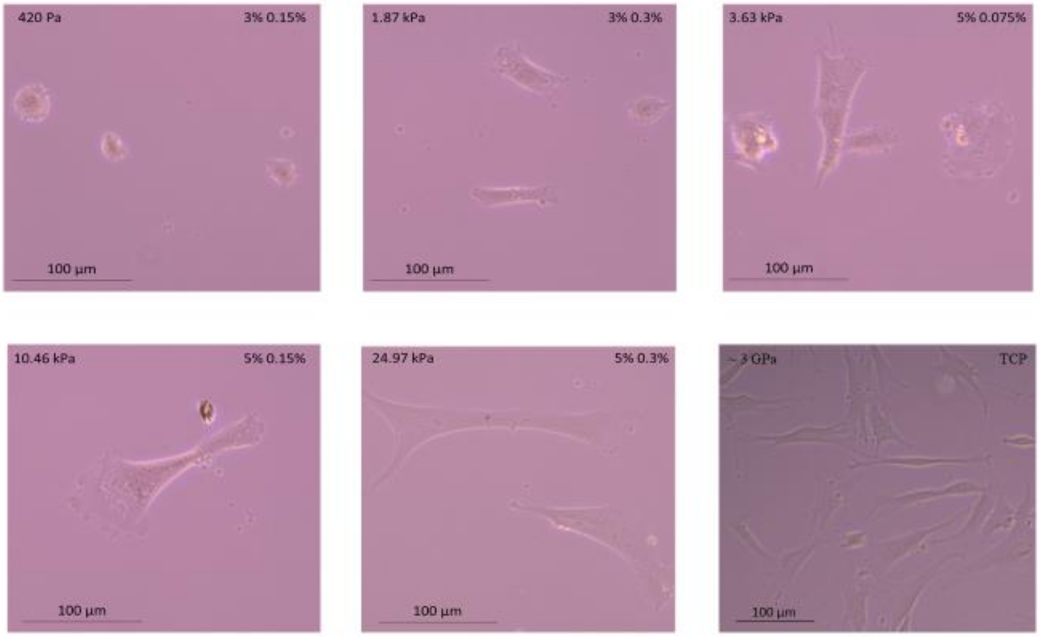

Figure 4.3: Phase contrast microscopy analysis of MRC-5 fibroblasts on PA gels. The Young's modulus of PA gels, as measured by force-indention AFM, is reported in the upper left corner, while the acrylamide and bis-acrylamide concentrations are reported in the upper right corner. TCP = tissue culture plastic

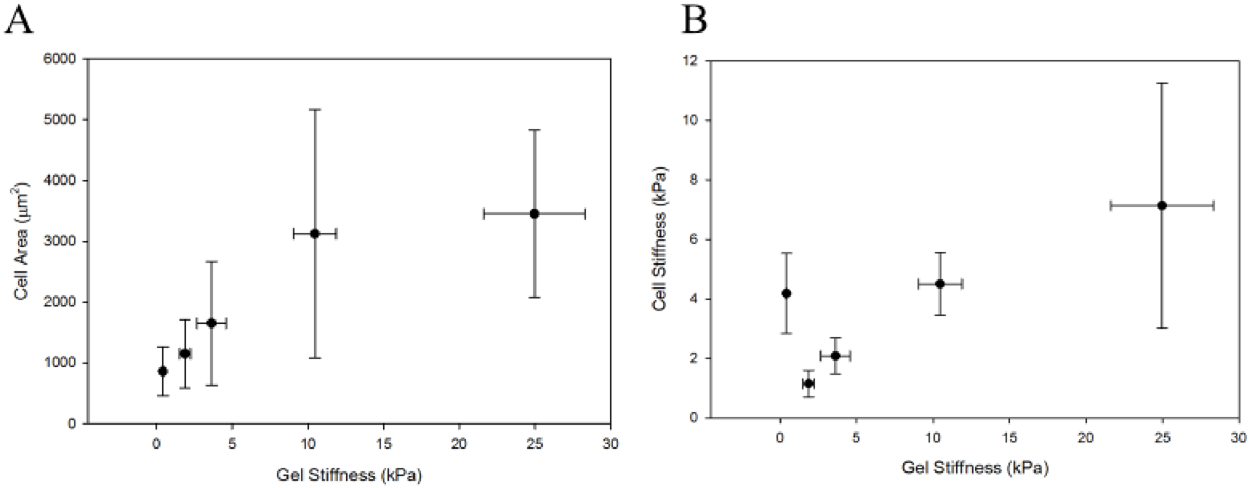

Figure 4.4: Microscopic analysis of MRC-5 fibroblasts growing on PA gels. (A) Projected cell area as a function of PA gel stiffness. Each point on the plot is a mean ± standard deviation of 70 – 100 cells. (B) Cell stiffness as a function of PA gel stiffness. Each point on the graph is a mean ± standard deviation of 12 – 15 different cells.

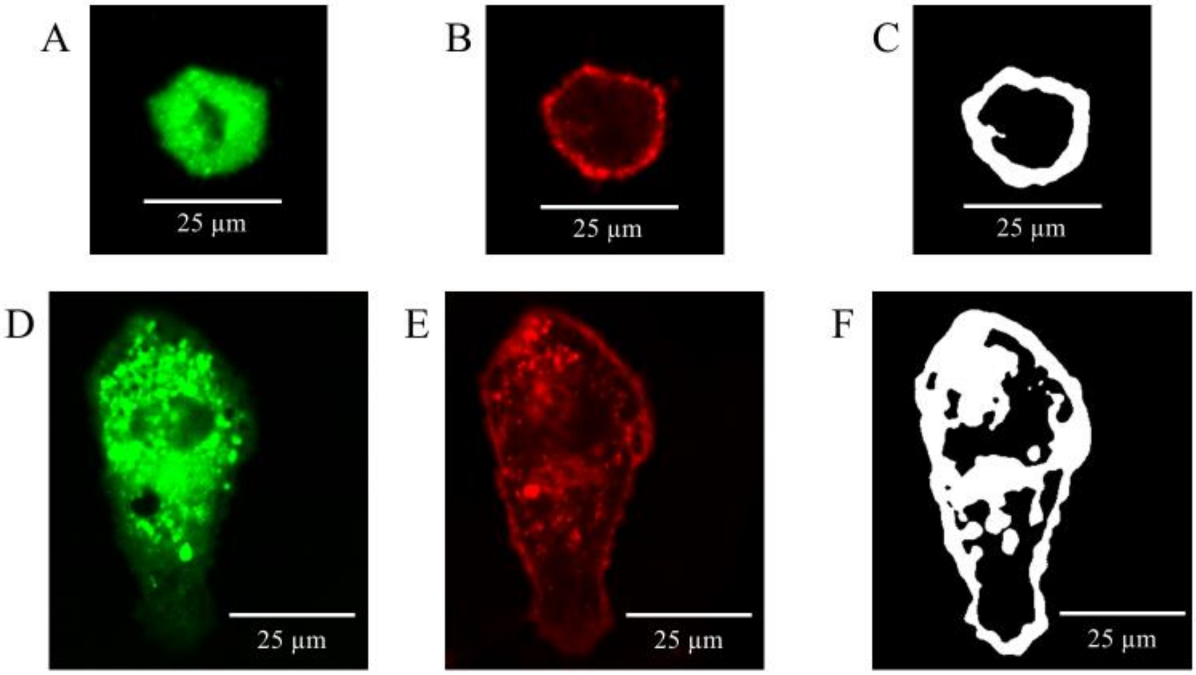

Figure 4.5: Confocal microscopy images of FCVJ fluorescence (A, D), CellMask Orange fluorescence (B, E), and the binary masks used for image analysis (C, F).

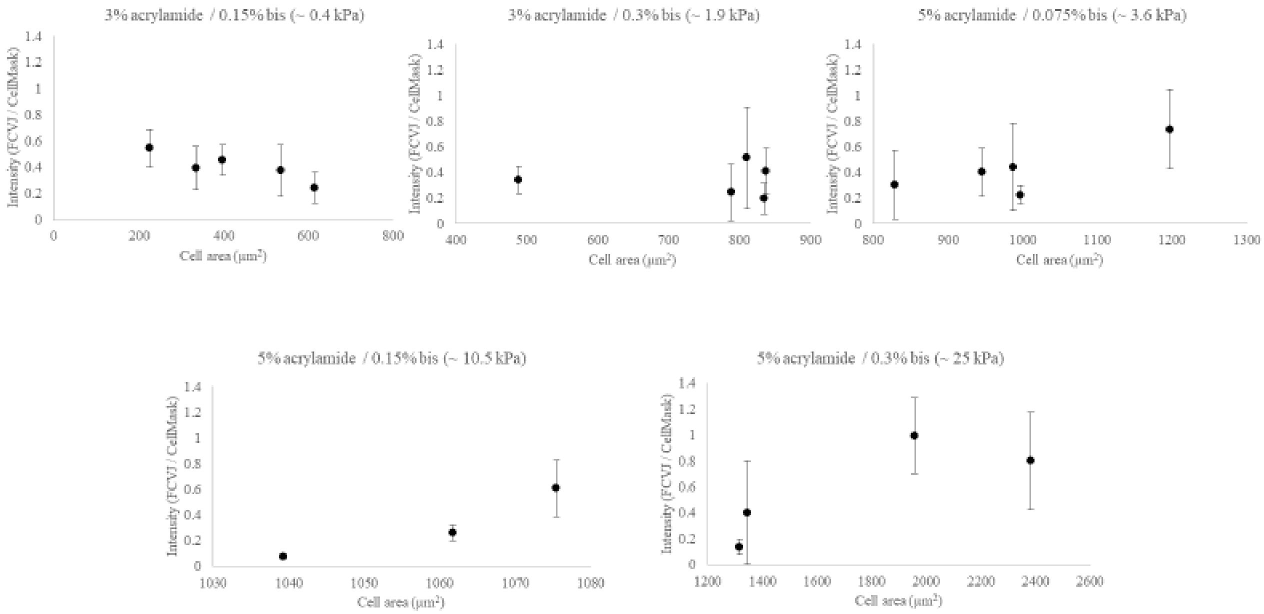

Figure 4.6: Average ratiometric fluorescence intensity plotted as a function of MRC-5 fibroblast cell area and split into subplots by substrate to make it easier to visualize the variability in fluorescence among cells growing on the same substrate. Each point represents an individual cell and is a mean ratiometric intensity of eight different regions of interest along the cell plasma membrane.

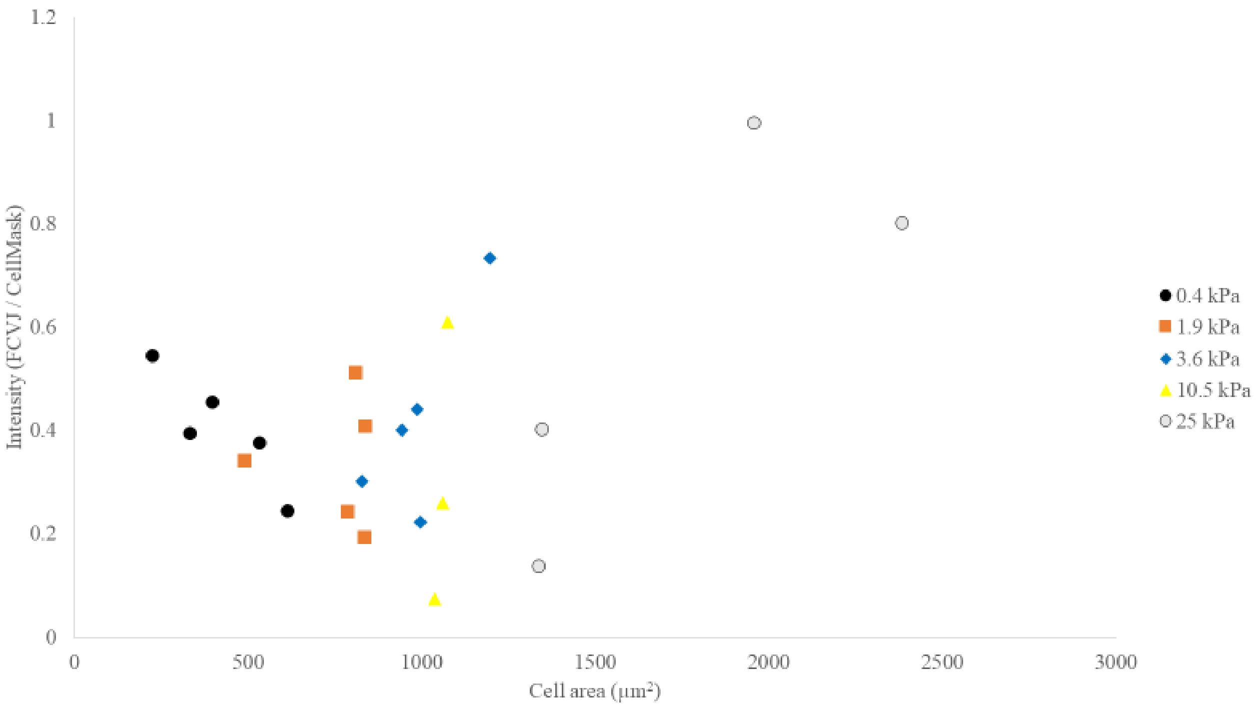

Figure 4.7: Average ratiometric fluorescence intensity plotted as a function of MRC-5 fibroblast cell area. Each point represents an individual cell and is a mean ratiometric intensity of eight different regions of interest along the cell plasma membrane. Five PA gels were used as substrates. Each PA gel substrate is represented by a unique data symbol and their mean Young's modulus, as measured by AFM, is reported in the Legend.

CHAPTER 5

A SERIES OF MINIMAL MODIFICATIONS TO THE NIKON PCM 2000 CONFOCAL MICROSCOPE SYSTEM FOR IMAGING UV- AND VISIBLE-WAVELENGTH EXCITABLE DYES[4]

---

[4] White, C. M., Haidekker, M. A., and Kisaalita, W. S. To be submitted to Measurement Science and Technology

5.1 Abstract

Confocal microscopy has become an essential tool for examining biological processes in vivo and in vitro. Here, we describe a series of simple modifications to repurpose an old confocal system from our lab. The confocal laser scanner module of a Nikon PCM 2000 confocal system was minimally modified (addition of two dichroic mirrors) and did not affect the confocal functionality. Lasers emitting at 375 nm and 405 nm were fiber-coupled to the scanner module. The resulting modifications offer several advantages: three-axis adjustment, modular design for interchangeable mirrors, affordable/cost saving. In addition, it is possible to revert the confocal system back to its original state. Using these modifications, we demonstrated the proof of concept with green fluorescent beads excited at 405 nm and red pollen grains excited at 543 nm.

5.2 Introduction

Confocal microscopy is a non-invasive optical imaging method commonly used for imaging fluorescence of an object, such as biological tissue. The principle of confocality lies in the placement of a pinhole in the optical path that eliminates out-of-focus signals, improving optical resolution and contrast. Although outperformed in many ways by two-photon microscopy for in vivo applications, confocal microscopy can still be valuable for in vivo imaging [1, 2] and is commonly used by researchers to study biological processes in vitro [3-5]. Unfortunately, new confocal systems are expensive pieces of equipment, often out of reach for many research groups. Many institutions operate core facilities that are available for an hourly fee, but these costs could discourage experimentation.

Confocal systems are readily available as relatively affordable surplus items that fulfill most research needs. Often these pieces of equipment can be found in surplus departments managed by universities or hospitals. One example involves our research laboratory’s Nikon

PCM 2000 confocal system, a perfectly good piece of equipment that was purchased and used extensively 20 years ago.

One recent research interest involves using a family of fluorescent molecules known for their relationship of microviscosity with emission quantum yield, termed molecular rotors, as a tool for studying plasma membrane viscosity of human cell lines. In particular, our pursuit to develop molecular rotors that have a non-sensitive reference unit to provide a calibration emission band and remove confounding factors associated with steady-state instrumentation [6] left us in a predicament. The numerous confocal microscope systems available at our university's microscope core were not equipped with a laser line that could sufficiently excite our reference fluorophore, 7-methoxycoumarin-3-carboxylic acid, and our attempts at using 2-photon excitation proved unsuccessful. As an alternative to redesigning the fluorophore pairing, the objective was to design and implement simple modifications to the Nikon PCM 2000 that allows for future imaging of cells stained with ratiometric molecular rotors. Another goal of the present work was to design the modifications such that the confocal system could be returned to its original state. The capacity to make fine adjustments to mirror placement, the easy exchange of dichroic mirrors and laser lines to meet multiple needs, and the ability to revert the system back to the original state makes this a universal approach to modification in turn encouraging experimentation.

5.3 Materials and Methods

Original Optical Configuration

The Nikon PCM 2000 scanner module is based on the principle of single-pinhole confocal microscopy as shown in Figure 1. In brief, visible continuous wavelength laser excitation enters the scanner module and is reflected through the confocal pinhole towards the x-y scanning mirrors by the first set of dichroic mirrors (DM). The sample is scanned, and the emitted light re-enters the scanner module where it is de-scanned and spatially filtered via the confocal pinhole. The emission signal passes through DM1 and is then spectrally separated by DM2 into two channels, each of which is fiber coupled to a photomultiplier tube (PMT).

Approach to Modification

The original fiber input plate and the input beam path of the scanner module were used. A 16.0 mW 375 nm ultra violet (UV) laser (Model No. LDCU8/8361, Power Technology Incorporated, Alexander, AR) and a 95 mW 405 nm diode laser (Model LMP405-95E, Newport, Irvine, CA) were aligned to a fixed focus laser collimator coupled with a SMA terminated multimode UV-visible fiber (Item # M132L01, Thorlabs, Newton, NJ). The other end of the fiber was terminated with a multimode FC/PC ceramic ferrule connector, which coupled with the scanner module.

In order to transmit the new excitation signal to the sample and the emission signals from the fluorophores of interest, the dichroic mirrors needed to be replaced (Figure 2A - E). The original focusing, collimating and re-collimating lenses, the reflecting and scanning mirrors, and the focusing lenses leading to the PMTs were used without further modification. A 565 nm longpass filter provided with the confocal system was used in the PMT2 light path. A bandpass filter (493/80 nm) available in our lab was used in the PMT1 light path. Since the diameter of this filter was larger than the filter holders provided with the confocal system, a new filter holder was 3D printed (Figure 2F).

There were two approaches to the modifications necessary to incorporate new dichroic mirrors:

1) The dichroic mirror ‘sliders’ were recreated with new dichroic mirrors attached (Figure 2A - C)

2) An ‘open scanner’ approach where an assembly of stages is used to insert the dichroic mirror into the fluorescence light path (Figure 2D and E)

To recreate the dichroic mirror slider (approach 1), the scanner module was opened, and the key features of the dichroic mirror slider were measured (Figure 2A - C). The key features were deemed to be the beveled edge of the slider, the width and thickness of the slider, and the cutouts in the slider that facilitate reflection of the excitation laser and transmission of the emission signal. The slider replicate was machined out of aluminum at the UGA college of engineering machine shop (Figure 2B and C). The dichroic mirrors were carefully glued to the sliders using small amounts of silicone glue applied to the four corners of the mirror.

The ‘open scanner’ (approach 2) concept involved creating a large base piece that allowed us to couple a translation stage and kinematic mount to the scanner module via M3 holes that became available when the scanner module lid was removed (Figure 2D and E). The base piece was 3D printed from carbon fiber reinforced nylon using a Stratasys Fortus 450MC printer (Stratasys, Eden Prairie, MN). A single axis translation stage (Thorlabs) allows manual adjustment to the positioning of the mirror and was mounted to the base piece. A kinematic platform mount (KM100B/M, Thorlabs) was attached to the translation stage to provide ± 4° tip and tilt control (Figure 2E). A L-bracket was designed to couple the mirror holder and the kinematic platform mount and was machined out of aluminum. A mirror holder piece that included small pillars with slots to allow for an easy exchange of the dichroic mirror, was 3D printed and adhered to the L-bracket using a small drop of epoxy (Figure 2D).

Two dichroic mirrors were used to replace DM1. A 493nm/593nm dichroic mirror filter (SKU: 102315973, Salvo Technologies Inc., FL) at 45° allowed both UV (375 nm) and visible light (543 nm from the Green Helium Neon (GHeNe) laser supplied with the PCM 2000) to be used interchangeably. The other was a 405nm/540nm DBDR dichroic mirror filter (F460-561DBDR-001, Omega Optical Inc., Brattleboro, VT) allowing both the 405 nm diode and 543 nm GHeNe to be used interchangeably. These dichroic mirrors transmitted the emission of our fluorophores of interest (peaks at 400 nm, 490 nm, and 567 nm). To split the emission signals between the two PMTs, a 545 nm long-pass dichroic (P549DRLPEXTR-001, Omega Optical Inc., Brattleboro, VT) was used in the place of DM2.

5.4 Results and Discussion

Alignment

After reassembling the scanner module with our dichroic mirror slider replicate (approach 1), we compared the critical reflection of the excitation laser through the confocal pinhole to the scanning mirrors. With the large confocal pinhole (10 µm diameter) in place, we observed an eclipse effect due to the laser beam hitting the support post of the first scanner mirror (Figure 3A and B). Selecting the smaller confocal pinhole (5 µm diameter) resulted in a complete blockage of the laser transmission (image not shown). One of our main goals for this project was to minimize the number of modifications, and the purpose of recreating the dichroic mirror slider was to use the existing slider assembly to hold the custom piece in the exact place as the original. However, it was impossible for us to test the accuracy of our custom piece unless we added the custom mirrors. Nikon’s solution to attaching the dichroic mirrors to the mirror slider was simply gluing the mirrors to the back of the slider (Figure 2C). Because the positioning of the mirrors relative to the rest of the slider assembly was critical, we decided our only option was to follow suit and glue our custom mirror to the back of the custom slider. Only after gluing our mirror to the slider could we observe the slight differences in how our custom slider fit into the slider assembly compared to the original, which was evident with the misalignment of the laser light through the pinholes (Figure 3A and B). This leads to an expensive trial and error approach of purchasing mirrors in bulk and machining multiple sliders in an attempt to improve the fit. One might suggest recreating the entire slider assembly, which would increase costs and might result in similar issues with the alignment of new parts. Therefore, we decided to pursue an approach that includes kinematic mounts in order to achieve laser alignment with the confocal pinhole system.

Due to the inability to adjust the alignment of our custom parts we decided to take an approach that used kinematic mounts (Figure 2E), which allowed for multi-axis freedom of motion. Furthermore, a mirror holder was designed and 3D printed to make DM1 interchangeable (Figure 2D). Fortunately, we were able to recover the 405nm/540nm DBDR dichroic filter glued to the custom slider without damaging the surface coating. This provided us the opportunity to have interchangeable dichroic filters for the use of all three laser lines (375 nm, 405 nm, 543 nm).

To test the alignment of modification approach #2, we again used the 543 nm GHeNe and a paper target to validate the ability to align the laser through both the large (image not shown) and small (Figure 3C) pinholes. Switching to the 405 nm laser, the paper target showed strong fluorescence and acceptable alignment with the pinhole. However, there appeared to be a significant power loss at the 45° mirror positioned after the pinhole and before the scanning mirrors when the 375 nm UV laser was used. The fluorescence from the paper target was barely detectable with the small pinhole was in place, which suggests this 45° mirror is not appropriate for reflecting UV light.

Application demonstrating imaging capability

To demonstrate the flexibility of our modification approach, we used a pollen grain sample (Figure 4A) and green fluorescent beads (Figure 4B) as model samples. The pollen grain samples are sufficiently excited by the 543 nm laser. A 60x oil immersion lens and small pinhole were used, which demonstrates the signal transmission through both DM1 and DM2. The 405 nm was then used to image green fluorescent beads, again using the 60x lens and small pinhole. A higher signal-to-noise ratio is evident for the green channel compared to the red channel. This could be due to the fluorescent bead emission not matching the dichroic mirror transmission profile. These results demonstrate a proof-of-concept for a cost-effective way to image novel dyes that are not typically targeted by equipment manufacturers.

5.5 Conclusions

In this technical report, we describe modifications of a commercial confocal microscope system that render it capable of imaging various visible light emissions via the integration of new laser sources and appropriate dichroic mirror filters. We have used typical commercially available UV laser diodes as well as a GHeNe laser that was supplied with the confocal system for the excitation output, but other affordable laser products can also be used. We have imaged green fluorescent beads and red pollen grains as a proof-of-concept. This series of modifications provides new capabilities for this affordable confocal system or similar systems commonly found in surplus inventories. This setup may be improved by performing further modification to replace the 45° mirror with one that can reflect a wider spectrum of light, including UV.

5.6 References

1. Bohn, S., et al., Cellular in vivo 3D imaging of the cornea by confocal laser scanning microscopy. Biomedical optics express, 2018. 9(6): p. 2511-2525.

2. Patel, D.V., J. Zhang, and C.N. McGhee, In vivo confocal microscopy of the inflamed anterior segment: A review of clinical and research applications. Clinical & Experimental Ophthalmology, 2019. 47(3): p. 334-345.

3. Kosmalska, A.J., et al., Physical principles of membrane remodelling during cell mechanoadaptation. Nature communications, 2015. 6: p. 7292.

4. Xie, K., Y. Yang, and H. Jiang, Controlling cellular volume via mechanical and physical properties of substrate. Biophysical journal, 2018. 114(3): p. 675-687.

5. Wullkopf, L., et al., Cancer cells' ability to mechanically adjust to extracellular matrix stiffness correlates with their invasive potential. Molecular biology of the cell, 2018. 29(20): p. 2378-2385.

6. Haidekker, M.A. and E.A. Theodorakis, Ratiometric mechanosensitive fluorescent dyes: Design and applications. J Mater Chem C Mater, 2016. 4(14): p. 2707-2718.

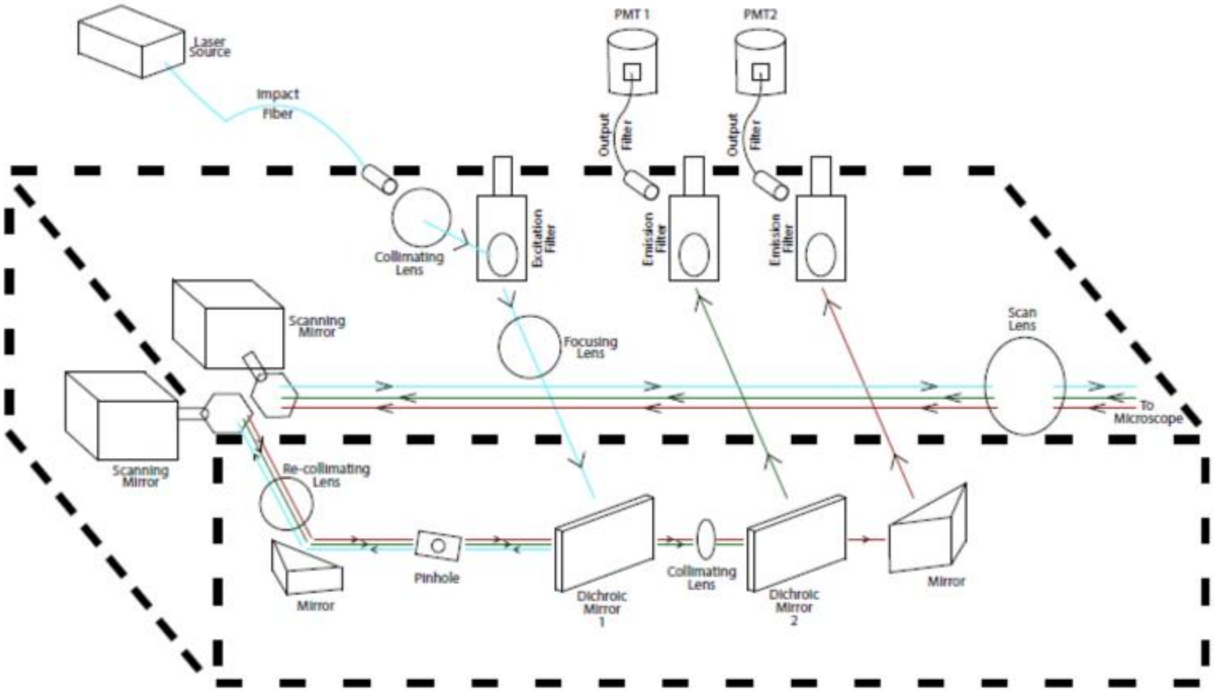

Figure 5.1: Schematic of Nikon PCM2000 confocal scanner module. Modifications to the scanner module will aim to replace normal dichroic mirrors 1 and 2 with custom mirrors.

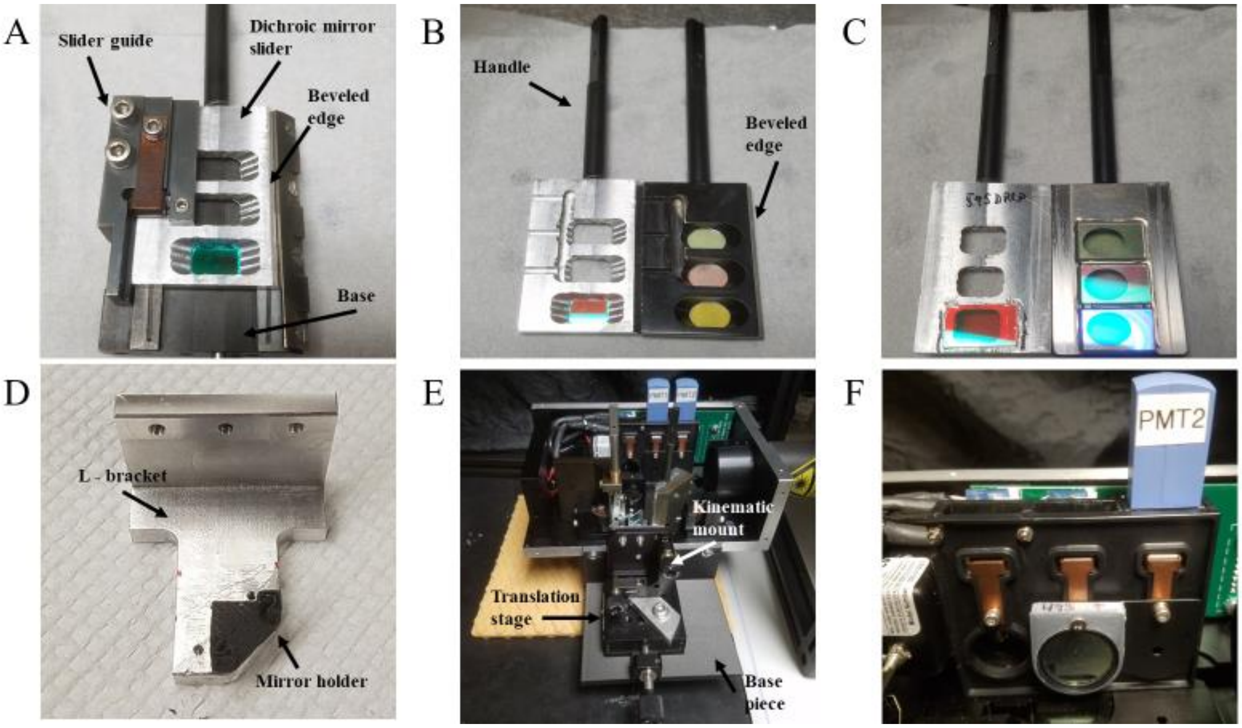

Figure 5.2: Modification approach #1 (A – C) involves replication of the dichroic mirror slider. The dichroic mirror assembly (A) includes the base which mounts to the scanner module, the slider to which the dichroic mirrors are glued, the slider guide which, along with the base, guides the movement of the slider and includes a roller pin that locks the slider into position, and the handle which is screwed into the top of the slider. Comparison of the original slider and custom slider frontside (B) showing the critical beveled edge feature of the slider and the backside (C) showing the glued dichroic mirrors. Modification approach #2 (D and E) involves an open scanner module which allows for coupling of an assembly of mounts and stages that provide 3-axis adjustment. The L-bracket (D) with the 3D printed mirror holder is attached to the kinematic platform mount and translation stage which are held in place by the base piece (E). A 3D printed emission filter holder (F) screws into place and allows us to use spare filters that are more appropriate for our fluorophore emission.

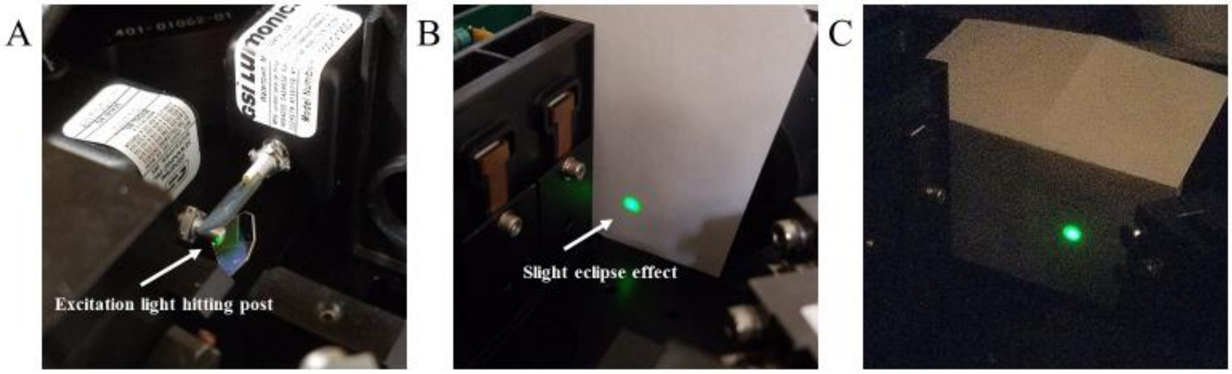

Figure 5.3: Alignment test of the dichroic mirror filter using the 543 nm helium neon laser and a paper target for modification approach #1 (A and B) and approach #2 (C). (A) and (B) show acceptable transmission of the excitation signal with the large (10 µm diameter) confocal pinhole with a slight eclipse effect. Misalignment with the smaller (5 µm diameter) confocal pinhole (image not shown) emphasizes the need for control over dichroic mirror positioning. With approach #2, the placement dichroic mirror filter can be adjusted to achieve total alignment with the large (image not shown) and the small pinhole (C).

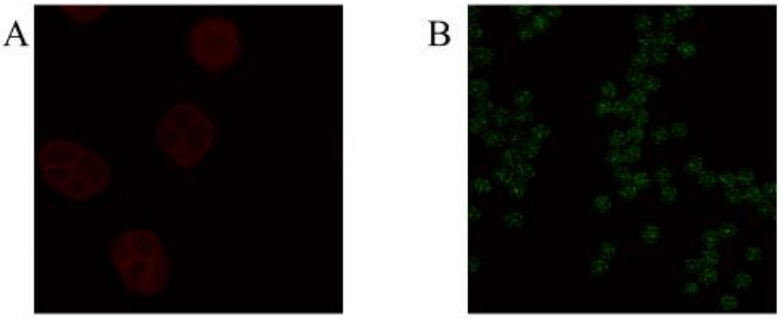

Figure 5.4: Images of model samples provides a proof-of-concept for modification approach #2. (A) Using the 543 nm helium neon laser and custom dichroic filters, a pollen grain sample can be imaged. (B) Using the 405 nm diode laser, an image of green fluorescent beads can be obtained, but with a rather high signal to noise ratio.

CHAPTER 6

STEADY-STATE CONFOCAL MICROSCOPY: LOW-COST ALTERNATIVE TO FLORESCENCE LIFETIME IMAGING OF CELL MICROVISCOSITY WITH MOLECULAR ROTOR PROBES[5]

---

[5] White, C. M., Haidekker, M. A., and Kisaalita, W. S. To be submitted to ACS Biomaterials Science and Engineering

6.1 Abstract

Optical modification of old (surplus) confocal scanning laser microscopes is a viable quantum yield-based low-cost alternative to more costly fluorescence lifetime measurement instrumentation for imaging of cell microviscosity using molecular rotors, which are a family of environment-sensitive probes.

6.2 Introduction

The cell membrane is one of the most ubiquitous components in biology, which not only acts as a barrier that separates the interior of a cell from its extracellular space but also strongly influences many functions and communication processes. Numerous diseases have been associated with alterations in membrane properties. Cancer cells, to name one example, can be characterized by cholesterol depletion, fluidity reduction, and an increase in phospholipid order [1]. This article describes promising methods for quantitative and spatial imaging of microviscosity within the plasma membrane of live cells.

One method involves fluorescence detection of a family of small molecules, termed molecular rotors, which relies on the relation between probe rotation in different membrane phases and fluorescence quantum yield. Molecular rotors that form twisted intramolecular charge transfer (TICT) complexes, are promising for studying cell state because of their ability to report microviscosity in real time and can be used with simple steady state confocal microscope systems available at most research institutes and readily available as surplus items. However, intensity-based measurements are influenced by dye concentration, which makes applications in heterogenous systems like the cell membrane impossible. A ratiometric approach, where an environment-insensitive fluorophore is covalently linked to an environment-sensitive molecular rotor has been demonstrated [2, 3] and has the potential to overcomes these issues in cell studies.

An alternative approach to intensity-based measurements involves measurements of fluorophore lifetimes, which have also been related to environmental microviscosity [4, 5]. In this article, we discuss the advantages and challenges of using quantum yield-dependent ratiometric molecular rotors compared to lifetime probes molecular rotor BODIPY and solvatochromic probe LAURDAN. Both approaches to measuring environmental microviscosity have potential to achieve the same result. Therefore, which approach is best for a new researcher might come down to availability of measurement resources or the budget available to invest in instrumentation.

6.3 Quantum yield-based molecular rotors and steady-state confocal microscopy

The principles of molecular rotors that form twisted intramolecular charge transfer (TICT) charge complexes upon photoexcitation have been extensively studied. To acquire a detailed understanding, we refer the reader elsewhere [6, 7]. Several chemical classes of molecular rotors exist [6], which can be divided into two categories. For the purposes of this discussion, we focus on single-band emission molecular rotors because they have been shown to be insensitive to the polarity of their environment [8, 9]. In brief, these molecular rotors respond to photoexcitation with an intramolecular charge transfer from an electron donor unit to an electron acceptor unit. From this planar locally excited state, there are two competing deexcitation pathways: emission of a green-shifted photon or the adoption of a non-planar (twisted) state with a lower excited-state energy. This twisting occurs within a time span that is much shorter than the excited lifetime. Relaxation from this TICT conformation occurs without photon emission. The LE quantum yield ϕ_F depends on the local microviscosity η following the Förster - Hoffmann equation [10]

$$\phi_F = \phi_0 * \left(\frac{\eta}{\sigma}\right)^x \qquad 1$$

where Φ_0 is the dye's intrinsic quantum yield, σ is a dye-specific constant, and x depends on both the dye and solvent. Doolittle [11] experimentally provided the relationship between viscosity and the free volume of macromolecule systems, which includes the lipid bilayer, while Loutfy [12] related molecular free volume to intramolecular rotation. Alterations in membrane properties results in a change in free volume and thus a change in apparent viscosity. In fact, fluidity (the inverse of viscosity) has been used in the fluid mosaic model of the cell membrane [13-15] to explain many of the physiological responses of the cell membrane. In this sense, apparent viscosity (and, related, free volume) serves as a suitable proxy for the freedom of motion of individual phospholipids, membrane-bound proteins, and whole membrane partitions such as lipid rafts.

Molecular rotors that form TICT complexes lend themselves to the notion of viscosity imaging because they require relatively simple steady-state instrumentation, they report changes in real time, and their spatial resolution is only limited by the optical system. However, viscosity measurements that rely on fluorescence quantum yield are inherently influenced by probe concentration. Although useful for studying viscosity in bulk homogenous solutions, the concentration uncertainty makes them unsuitable for heterogenous systems like a live cell.

This was the motivation behind the development of self-calibrating dual dyes that are composed of an internal reference dye bound to a molecular rotor [2, 3]. The equation

$$I_{Rotor} = I_{ex} * G * c * \phi_F \tag{2}$$

where I_{Rotor} is the peak emission intensity of a molecular rotor, I_{ex} is the intensity of the excitation light, c is the dye concentration, and G is an instrument gain factor, proportionally relates the fluorescence intensity of a TICT rotor to quantum yield. Equation 2 is valid for the emission of a viscosity-independent reference dye (I_{Ref}) and a viscosity-independent quantum yield (ϕ_{Ref}), and the resulting ratio of the rotor and reference emissions can be simplified to Equation 3

$$\frac{I_{Rotor}}{I_{Ref}} = \frac{(G * c * I_{ex}) * \phi_F}{(G * c * I_{ex}) * \phi_{Ref}} = \frac{\phi_0}{\phi_{Ref}} * \left(\frac{\eta}{\sigma}\right)^x \quad 3$$

assuming a known and constant reference dye quantum yield ϕ_{Ref}, the ratiometric intensity gives access to the molecular rotor's quantum yield, which is otherwise only obtainable with expensive fluorescence lifetime measurement equipment. In addition, the ratiometric intensity allows direct computation of viscosity where x, σ, and ϕ_0 can be considered calibration constants and obtained from model solvents. The result is a direct measurement of local viscosity, which can be reported in viscosity units (mPa * s) [2].

The most successful example of ratiometric TICT molecular rotors use coumarin derivative motifs [2, 3, 16] as a covalently linked reference dye which exhibits no viscosity sensitivity. Coumarin pairing has several advantages - coumarin has a quantum yield near unity which makes it an efficient donor for FRET, sufficiently large spectral overlap, and favorable dipole-dipole orientation. Two versions of these ratiometric TICT rotors have been previously tested with cell culture [16]: a hydrophilic dye with a piperidine subunit appeared to stain the cytosol while a more lipophilic dye with a dihexylamine subunit appeared to have a preference for intracellular compartments and a moderate co-localization with the membrane dye DiI-C18.

For cell membrane measurements, the preference for cytosol and organelle staining described by Dakanali and colleagues [16] is not ideal. Considering the advantages of using a ratiometric TICT rotor, we propose the following potential solutions. The first involves using a plasma membrane-specific dye, such as the CellMask series of dyes, in tandem with a ratiometric TICT rotor. Through a series of image processing steps, a binary mask can be obtained from the CellMask image and applied to the ratiometric dye images to isolate the fluorescent signal from the plasma membrane. The other potential solution involves replacing the dihexylamine subunit with a modified carbon chain that includes a double positive charge, which has shown improved plasma membrane staining that was more resilient against endocytosis [17]. In this case, the FRET efficiency and viscosity sensitivity of the new ratiometric TICT rotor would need to be reevaluated to see if this modification changed the behavior of the dye.

Another consideration is excitation of the reference coumarin motif with steady state confocal instrumentation. Although UV excitable DNA fluorophores like DAPI and Hoechst are widely used, they can be sufficiently excited with a 405 nm steady state laser. The Stokes shift for coumarin, however, is much shorter (Figure 1), making it impossible to image with most commercially available confocal systems as they do not come equipped with a true ultraviolet (UV, ~350 - 375 nm) laser.

For the handy researcher or engineer, resources are available [18, 19] that can provide guidance on how to successfully modify existing confocal microscope systems. These examples provide a proof-of-concept for optical modifications that enable UV excitation while maintaining the visible light capabilities of the system. Old confocal systems can often be found as surplus items through universities and research hospitals at a fraction of the cost for new instrumentation. This approach provides an opportunity to tailor individual optical components to suit your combination of fluorophores.

Here, we reviewed current literature to address the advantages and challenges of using TICT molecular rotors and steady-state instrumentation to measure cell microviscosity. It is clear that additional research and development into membrane compatibility is needed. Furthermore, to date only a limited number of blue-green reference and rotor fluorophore combinations have been reported [2, 3, 16]. The blue shifted excitation and emission spectra of these TICT rotors, which includes excitation in the range of true UV (350 - 375 nm) and emission bands in the range of 400 - 500 nm makes them less useful for in vivo applications. With these limitations in mind, we briefly introduce two fluorescence lifetime probes that have been widely used for cell membrane studies as an alternative approach to measuring cell membrane properties.

6.4 Lifetime-based probes and fluorescence lifetime imaging microscopy (FLIM)

Considering the challenges associated with the current knowledge on ratiometric TICT molecular rotors, alternatives must be considered. Not only are molecular rotors useful for quantum yield-based sensing of microviscosity, their fluorescence lifetime dependence on microviscosity has also been studied [4]. Fluorescence quantum yield ϕ_F is related to fluorescence lifetime τ_F by the equation

$$\phi_F = \frac{\tau_F}{\tau_N} \qquad 4$$

where τ_N is the natural lifetime of the fluorophore in the absence of nonradiative deexcitation. Therefore, it is theoretically possible to relate the fluorescence lifetime of FCVJ to the microviscosity of the cell membrane. The advantage of using lifetime measurements over quantum yield is that the lifetime does not change as a function of local concentration. Lifetime measurements allow for sequential calculation of microviscosity and quantum yield [4, 5]. Unfortunately, the lifetime of many TICT molecular rotors, including FCVJ, is extremely short (from 10 to 100 ps [20]) making it impractical to use for lifetime imaging applications.

The solvatochromic probe LAURDAN [21-23] and a class of molecular rotors based on the boron dipyrromethene (BODIPY) fluorophore [4, 5, 17] have been used extensively for studying the cell membrane and could serve as alternatives to ratiometric TICT molecular rotors. Relating to membrane studies, the LAURDAN spectrum has the advantage of being sensitive to not just membrane fluidity but composition as well. The LAURDAN spectrum tends to be green shifted if the membrane contains shorter or unsaturated aliphatic compounds, or if the dye is located in a liquid disordered phase of the lipid bilayer. Dipolar relaxation has also been demonstrated to green shift the spectrum. Therefore, separating the influence of lipid composition from membrane fluidity has proven difficult, and obtaining just the spectral or lifetime information alone is not enough. However, recent work has demonstrated a novel multidimensional phasor approach to visualizing spectral and lifetime measurements obtained at the same plane of a cell [23]. Using this approach, Sameni and colleagues revealed alterations in plasma membrane fluidity can be used as a hallmark for the neurodegenerative disorder Huntington disease [24].

The BODIPY-based molecular rotors extensively used by Kuimova and colleagues [4, 5, 17] are attractive probes for cell membrane studies because their fluorescence lifetime is long enough that they have been successfully implemented in fluorescence lifetime imaging microscopy (FLIM). The advantage of BODIPY probes is their relative ease of synthesis and their monoexponential decay function, which makes their decay kinetics easy to interpret. A BODIPY derivative reported in Lopez-Duarte et al. avoided the endocytosis associated with other BODIPY derivatives by including a double positive charge on its hydrocarbon tail [17]. BODIPY-based probes have recently been used to measure viscosity of *Escherichia coli* plasma membranes [25], plasma membrane viscosity of dissociate hippocampal neurons [26], and the three-dimensional (3D) tumor environment [27, 28].

LAURDAN and BODIPY are considered lifetime probes and therefore rely on the availability of lifetime instrumentation. Fluorescence lifetime imaging microscopy (FLIM) allows for spatially resolved imaging of fluorescence lifetime information to be recorded. FLIM can be used with readily available continuous wave lasers for frequency-domain measurements (although this requires complex data processing) or two-photon excitation microscopy for time-domain lifetime measurements. However, time-domain measurements require precise timing and pulsed multiphoton excitation from femtosecond lasers. In general, the acquisition of fluorescence lifetime information depends on many factors, including but not limited to the rate at which photons can be obtained from a sample, how efficiently your technique can determine fluorescence decay parameters from the recorded photons, the number of pixels available, and the resolutions (axial and lateral) obtained. Taken together, these factors make lifetime experiments complex when compare to steady state instruments. Fluorescence lifetime probes have proven useful for many cellular applications but could be difficult to implement unless FLIM instrumentation is readily available.

From a biological perspective, it is important to continue to push forward the development of technologies for accurately detecting cell membrane properties. In recent years, optical techniques have proven advantageous because of their excellent temporal and spatial resolutions. Not only do these spectroscopic techniques rely on the synthesis, characterization, and selection of fluorescent molecules, the approach for imaging and measuring is critical for success.

6.5 Concluding Remarks

Fluorescent probes such as LAURDAN and BODIPY are popular lifetime probes because of their compatibility with the plasma membrane and their ability to be used with multiphoton excitation microscopy, which potentially allows them to be used in 3D in vitro and in vivo studies. However, they rely on expensive lifetime equipment - costing in the range of hundreds of thousands of dollars. For a typical individual investigator in a university setting, lifetime imaging instrumentation may not be available, which makes the possibility of using these probes well out of reach. TICT molecular rotors, and more recently ratiometric TICT molecular rotors, which report viscosity in a quantum yield-dependent manner, are an attractive alternative because they can be used with simple steady-state instrumentation. Modifications to available or surplus steady-state confocal systems to incorporate UV excitation, or exploring different fluorophore pairings for new ratiometric TICT molecular rotors, could be a more realistic and low-cost approach to achieving one’s research goals.

6.6 References

1. Erazo-Oliveras, A., et al., Functional link between plasma membrane spatiotemporal dynamics, cancer biology, and dietary membrane-altering agents. Cancer and Metastasis Reviews, 2018. 37(2-3): p. 519-544.
2. Yoon, H.J., et al., Synthesis and evaluation of self-calibrating ratiometric viscosity sensors. Org Biomol Chem, 2011. 9(9): p. 3530-40.
3. Nipper, M.E., et al., Detection of liposome membrane viscosity perturbations with ratiometric molecular rotors. Biochimie, 2011. 93(6): p. 988-994.
4. Kuimova, M.K., et al., Molecular rotor measures viscosity of live cells via fluorescence lifetime imaging. Journal of the American Chemical Society, 2008. 130(21): p. 6672-6673.
5. Levitt, J.A., et al., Membrane-bound molecular rotors measure viscosity in live cells via fluorescence lifetime imaging. The Journal of Physical Chemistry C, 2009. 113(27): p. 11634-11642.
6. Haidekker, M.A., et al., Dyes with segmental mobility: molecular rotors, in Advanced Fluorescence Reporters in Chemistry and Biology I. 2010, Springer. p. 267-308.
7. Haidekker, M.A. and E.A. Theodorakis, Ratiometric mechanosensitive fluorescent dyes: Design and applications. J Mater Chem C Mater, 2016. 4(14): p. 2707-2718.
8. Haidekker, M.A., et al., Effects of solvent polarity and solvent viscosity on the fluorescent properties of molecular rotors and related probes. Bioorg Chem, 2005. 33(6): p. 415-25.
9. Kung, C.E. and J.K. Reed, Microviscosity measurements of phospholipid bilayers using fluorescent dyes that undergo torsional relaxation. Biochemistry, 1986. 25(20): p. 6114-6121.

10. Förster, T. and G. Hoffmann, Die viskositätsabhängigkeit der fluoreszenzquantenausbeuten einiger farbstoffsysteme. Zeitschrift für Physikalische Chemie, 1971. 75(1_2): p. 63-76.

11. Doolittle, A.K., Studies in Newtonian flow. III. The dependence of the viscosity of liquids on molecular weight and free space (in homologous series). Journal of Applied Physics, 1952. 23(2): p. 236-239.

12. Loutfy, R.O. and B.A. Arnold, Effect of viscosity and temperature on torsional relaxation of molecular rotors. The Journal of Physical Chemistry, 1982. 86(21): p. 4205-4211.

13. Singer, S. and G.L. Nicolson, The fluid mosaic model of the structure of cell membranes. Membranes and Viruses in Immunopathology; Day, SB, Good, RA, Eds, 1972: p. 7-47.

14. Vereb, G., et al., Dynamic, yet structured: the cell membrane three decades after the Singer–Nicolson model. Proceedings of the National Academy of Sciences, 2003. 100(14): p. 8053-8058.

15. Engelman, D.M., Membranes are more mosaic than fluid. Nature, 2005. 438(7068): p. 578-580.

16. Dakanali, M., et al., Self-calibrating viscosity probes: design and subcellular localization. Bioorg Med Chem, 2012. 20(14): p. 4443-50.

17. López-Duarte, I., et al., A molecular rotor for measuring viscosity in plasma membranes of live cells. Chemical Communications, 2014. 50(40): p. 5282-5284.

18. Bliton, C., J. Lechleiter, and D. Clapham, Optical modifications enabling simultaneous confocal imaging with dyes excited by ultraviolet-and visible-wavelength light. Journal of Microscopy, 1993. 169(1): p. 15-26.

19. Bliton, A.C. and J.D. Lechleiter, Optical considerations at ultraviolet wavelengths in confocal microscopy, in Handbook of biological confocal microscopy. 1995, Springer. p. 431-444.

20. Levitt, J.A., et al., Fluorescence anisotropy of molecular rotors. ChemPhysChem, 2011. 12(3): p. 662-672.

21. Parasassi, T., et al., Membrane aging during cell growth ascertained by Laurdan generalized polarization. Experimental cell research, 1992. 202(2): p. 432-439.

22. Harris, F.M., K.B. Best, and J.D. Bell, Use of laurdan fluorescence intensity and polarization to distinguish between changes in membrane fluidity and phospholipid order. Biochimica et Biophysica Acta (BBA)-Biomembranes, 2002. 1565(1): p. 123-128.

23. Malacrida, L., D.M. Jameson, and E. Gratton, A multidimensional phasor approach reveals LAURDAN photophysics in NIH-3T3 cell membranes. Scientific reports, 2017. 7(1): p. 9215.

24. Sameni, S., et al., Alteration in fluidity of cell plasma membrane in Huntington disease revealed by spectral phasor analysis. Scientific reports, 2018. 8(1): p. 734.

25. Mika, J.T., et al., Measuring the viscosity of the Escherichia coli plasma membrane using molecular rotors. Biophysical journal, 2016. 111(7): p. 1528-1540.

26. Kubánková, M., et al., Microscopic Viscosity of Neuronal Plasma Membranes Measured Using Fluorescent Molecular Rotors: Effects of Oxidative Stress and Neuroprotection. ACS Applied Materials & Interfaces, 2019. 11(40): p. 36307-36315.

27. Shirmanova, M.V., et al., Live cell imaging of viscosity in 3d tumour cell models, in Multi-Parametric Live Cell Microscopy of 3D Tissue Models. 2017, Springer. p. 143-153.

28. Lyubov'E, S., et al., Imaging tumor microscopic viscosity in vivo using molecular rotors. Scientific reports, 2017. 7(1): p. 1-11.

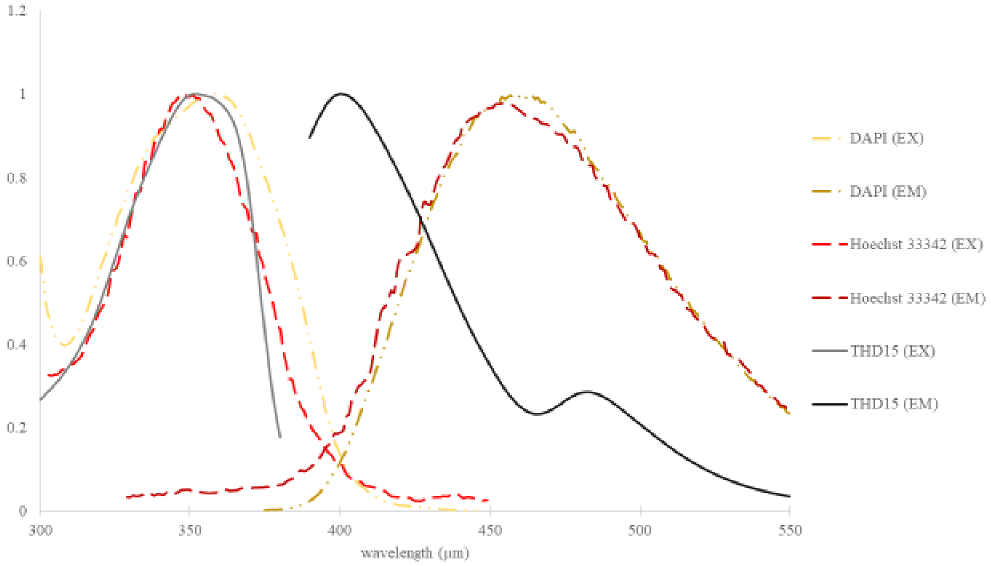

Figure 6.1: Fluorescence excitation and emission spectra for nuclear stain DAPI, Hoechst 33342, and the ratiometric TICT molecular rotor compound 24 [16]. Although DAPI, Hoechst 33342, and the coumarin motif used as a reference fluorophore have similar excitation spectra, the coumarin Stokes shift is much smaller.

CHAPTER 7

CONCLUDING REMARKS AND FUTURE PERSPECTIVES

The overall aim of this study was to establish the efficacy of fluorescent molecular rotors as a tool for characterizing the cell plasma membrane. The biological question we wished to explore, as a proof-of-concept for cell membrane applications of molecular rotors, was whether there was a detectable change in membrane viscosity as a part of the cellular response to substrate stiffness in 2D and 3D culture settings. As a first step, we optimized the 2D (chemically equivalent (fibronectin-coated) acrylamide gels with different compliances) and 3D (patterned Polystyrene with fibronectin-coated, micron-scale wells) culture platforms needed to study the influence of substrate stiffness. Using MRC-5 fibroblasts, we confirmed both culture platforms could support cell culture adhesion and growth and were optically suitable for fluorescence microscopy applications.

The next step was to validate the capacity of MRC-5 fibroblasts to sense and adapt to substrate stiffness via mechanotransduction. An increase in cell area and cell stiffness was correlated to an increase in acrylamide gel substrate rigidity, both hallmarks of mechanotransduction. Fibroblasts were stained with molecular rotor FCVJ and imaged using fluorescent confocal microscopy. Due to strong intracellular fluorescence and signs of endocytosis we could not assume equal concentration among cell samples, and consequently, drawing a strong conclusion from intensity measurements between cells growing on the same gel substrate and cells growing on gel substrate with different Young’s moduli was impossible.

We turned our attention to a group of molecular rotors that were covalently linked to a fluorophore with viscosity-independent quantum yield. The reference fluorophore signal can be used to determine concentration while the molecular rotor signal can be used to determine viscosity, making them ratiometric probes. The close proximity of the two fluorophores makes them a resonance energy transfer (RET) pair, which allows both fluorophores to be excited by a single UV excitation source. The confocal system used to image FCVJ fluorescence was not equipped with a suitable UV laser, so we explored multiphoton excitation as a possible alternative. Fluorescence was detectable from the rotor at a multiphoton excitation wavelength of 775 nm. However, fluorescence was not detectable from the coumarin motif used as the reference and donor fluorophore of the RET pair. Using a solution of coumarin without the rotor revealed the fluorophore has the same multiphoton excitation peak as the molecular rotor (775 nm). We concluded that an energy barrier exists, probably due to the two fluorophores forming a RET pair and having similar multiphoton excitation maxima, that prevents both from being excited using multiphoton excitation methods.

Consequently, we designed and executed a series of modifications to a Nikon PMC2000 confocal system available in our laboratory for the purpose of imaging UV-excitable ratiometric molecular rotors. Our second design iteration provided multi-axis adjustment of a custom-purchase dichroic mirror, splitting the excitation beam from the emission signal and resulting in an alignment of the excitation beam with the critical confocal pinhole system. An additional custom-purchase dichroic mirror was used to split the emission signal between the two photomultiplier tubes, which forms the basis for fluorescence image acquisition. This approach to modification provides the investigator the freedom to change the dichroic mirror pairing to suit their specific needs. It also allows for different fiber-coupled laser systems to be used as an excitation source. We successfully used a 405 nm UV and 543 nm green helium-neon lasers to image model specimen as a proof-of-concept. However, upon fiber-coupling of a 365 nm UV laser, required to excite the ratiometric molecular rotor reference fluorophore coumarin, we noticed a significant power loss at the 45° reflection mirror located between the pinhole system and the scanning mirrors.

Without an excitation source suitable for imaging coumarin, the dual-emission ratiometric molecular rotors provided no additional benefit when compared to single-emission molecular rotor FCVJ. One ratiometric molecular rotor was synthesized with a dihexylamine subunit in an attempt to make it more lipophilic. To test the preferential localization of this rotor, we stained a fibroblast cell sample with the molecular rotor and plasma membrane specific CellMask Orange. We directly excited the rotor with a 405 nm laser source and compared the staining profiles of the two fluorophores. Despite the addition of a more fatty dihexylamine subunit, the rotor still showed preferential localization in the membrane or other hydrophobic domains of organelles.

Future work should include continued research and development on ratiometric molecular rotors to address the issues relating to membrane specificity and UV excitation. Continuation of the Nikon PCM 2000 modifications is one route. As a first step, 45° mirrors capable of reflecting a large spectrum of UV and visible light could be used to replace the original 45° mirror positioned between the pinhole and scanning mirrors. However, relating to the original desire to use ratiometric molecular rotors for 3D viscosity imaging, UV excitation is not ideal because it does not penetrate 3D tissues. Another route would be a different approach to ratiometric reference/rotor fluorophore pairing with the aim to achieve multiphoton excitation. Multiphoton excitation is advantageous over single photon UV excitation for 3D and in vivo fluorescence imaging. Taking an altogether different approach and investing in lifetime viscosity probes and instrumentation is an expensive, but not impossible, alternative. Lifetime rotors such as LAURDAN are well documented and extremely membrane compatible. Depending on available resources, one of the above routes will be needed before the 2D gel study can be repeated and the 3D viscosity imaging study can be undertaken. Lastly, it was our ambition to explore the potential for viscosity imaging to be used as a tool combined with membrane properties as a ‘marker’ for differences in cell function and state. As an example, two breast cancer cell lines, MCF-7 and MDA-MB-231, have different metastatic potentials and are commonly used as in vitro cell models for breast cancer. We envision membrane properties being a useful ‘marker’ for metastasis. As another example, tissue-derived stem cells have shown promise for regenerative medicine therapies, but first they must be identified from other cell types. The notion of viscosity imaging has the potential to become a useful tool for sorting heterogenous cell samples.

APPENDIX A

SUPPLEMENTARY DATA FOR CHAPTER 4

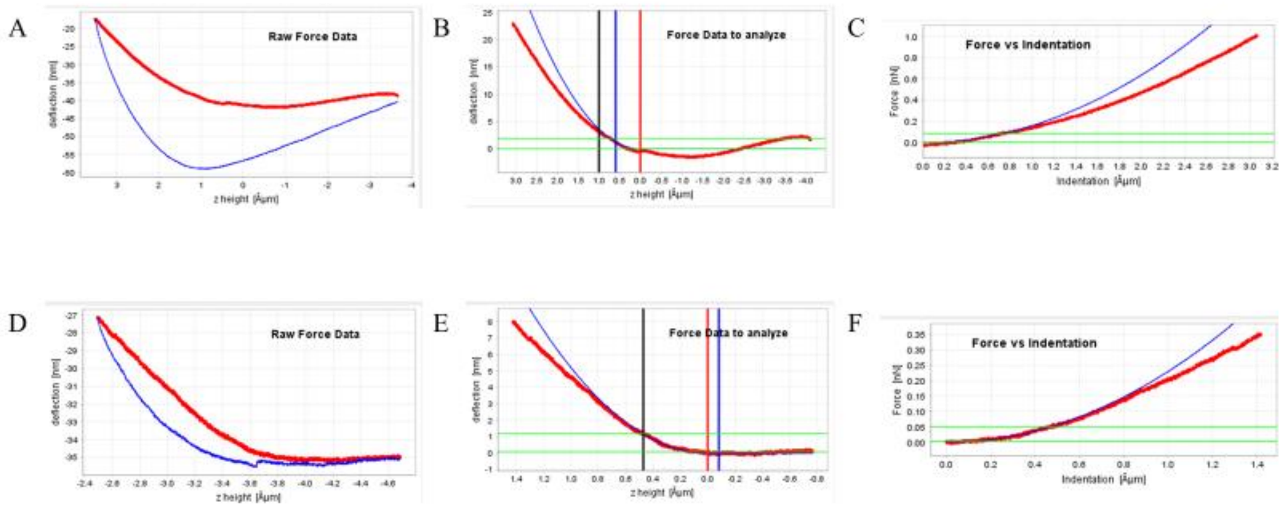

Supplementary Figure 4.1: Typical AFM force-indentation curves for fibroblasts grown on soft polyacrylamide substrates (A - C) and stiff polyacrylamide substrates (D - E). The raw approach (red curve) and retract (blue curve) force data is shown (A and D). The approach curves were used for analysis to avoid any adhesion effects between the AFM tip and the glycocalyx that might be present in the retract curve. (B and E) Force curves are analyzed in a region of interest determined by the delta1 and delta2 values (green lines). Using the Hertz model, a contact point is determined and a theoretical curve (blue curve) is fit to the data (red curve). The best first guess for the contact point is determined based on the deflection increasing past a threshold value, but this guess will be systematically wrong. The application then makes iterative guesses to determine the most likely contact point. The force versus indentation is calculated and plotted (C and F) from which the modulus is calculated.

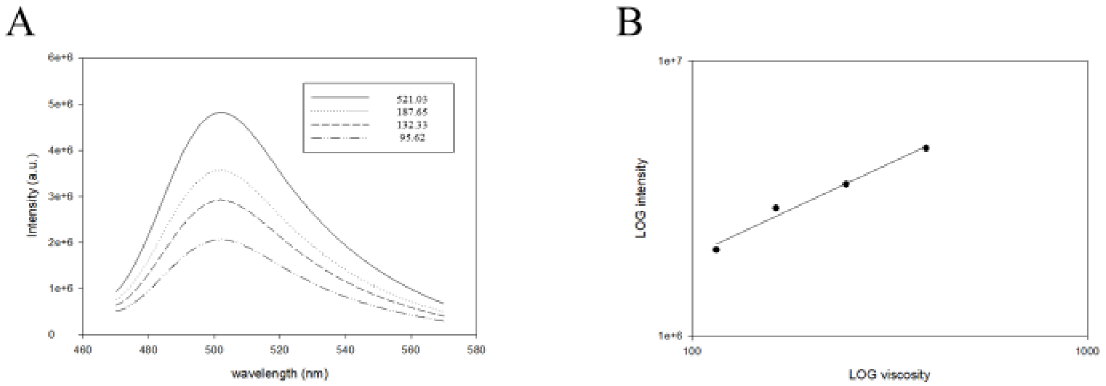

Supplementary Figure 4.2: Fluorescence emission spectra (A) and viscosity sensitivity plot (B) of FCVJ in glycerol : methanol mixtures (viscosity is reported in mPa * s [1]).

Figure References

1. Ghotli, R.A., et al., Selected physical properties of binary mixtures of crude glycerol and methanol at various temperatures. Journal of Industrial and Engineering Chemistry, 2015. 21: p. 1039-1043.

APPENDIX B

OTHER PUBLICATIONS

EVALUATION OF CELLULAR ADHESION AND ORGANIZATION IN DIFFERENT MICROPOROUS POLYMERIC SCAFFOLDS[6]

Abstract

The lack of prediction accuracy during drug development and screening risks complications during human trials, such as drug-induced liver injury (DILI), and has led to a demand for robust, human cell-based, in vitro assays for drug discovery. Microporous polymer-based scaffolds offer an alternative to the gold standard flat tissue culture plastic (2D TCPS) and other 3D cell culture platforms as the porous material entraps cells, making it advantageous for automated liquid handlers and high-throughput screening (HTS). In this study, we optimized the surface treatment, pore size, and choice of scaffold material with respect to cellular adhesion, tissue organization, and expression of complex physiologically relevant (CPR) outcomes such as the presence of bile canaliculi-like structures. Poly-L Lysine (PLL) and fibronectin (FN) coatings have been shown to encourage cell attachment to the underlying substrate. Treatment of the scaffold surface with NaOH followed with a coating of FN improved cell attachment and penetration into pores. Of the two pore sizes we investigated (A: 104 ± 4 µm; B: 175 ± 6 µm), the larger pore size better promoted cell penetration while limiting tissue growth from reaching

---

[6] Asthana, A.*, White, C. M.*, Douglass, M., & Kisaalita, W. S. (2018). Evaluation of cellular adhesion and organization in different microporous polymeric scaffolds. *Biotechnology progress*, *34*(2), 505-514. *Indicates authors contributed equally to this work.

Reprinted here with permission of publisher the hypoxia threshold. Finally, polystyrene (PS) proved to be conducive to cell growth, penetration into the scaffold, and yielded CPR outcomes while being a cost-effective choice for HTS applications. These observations provide a foundation for optimizing microporous polymer-based scaffolds suitable for drug discovery.

SECRETOME-BASED PREDICTION OF THREE-DIMENSIONAL HEPATIC MICROTISSUE PHYSIOLOGICAL RELEVANCE[7]

Abstract

Early biomarkers for indication of the complex physiological relevance (CPR) of a three-dimensional (3D) tissue model are needed. CPR is detected late in culture and requires different analytical techniques. Albumin production, CYP3A4 expression, and formation of bile canaliculi structures are commonly used to compare in vitro hepatic cells to their in vivo counterpart. A universal biomarker independent of cell type would bring this to a common detection platform. We make the case that these hepatic characteristics are not sufficient to differentiate traditional (2D) cell culture from the more complex 3D culture. We explored cytokine secretion profile (secretome) for its potential as a 3D early culture biomarker. PDGF-AB/BB and VEGF were found to be upregulated in 3D compared to 2D cultures at early time points (day 3 and 4). These observations provide a foundation upon which in vivo validation of cytokines can lead to physiologically relevant 3D in vitro cell culture.

---

[7] Reprinted with permission from (Asthana, A[*]., White, C. M.[*], Ndyabawe, K., Douglass, M., & Kisaalita, W. S. (2019). Secretome-Based Prediction of Three-Dimensional Hepatic Microtissue Physiological Relevance. *ACS Biomaterials Science & Engineering*. *Indicates authors contributed equally to this work). Copyright (2019) American Chemical Society.

ENHANCED TRANSIENT GENE EXPRESSION (TGE) WITH SCALABLE 3D POLYMERIC SCAFFOLDS[8]

Abstract

Transient gene expression (TGE) just takes 8-10 days as compared to production of stable cell lines, which takes months. This is especially important when a large number of candidate proteins have to be evaluated for their potential as therapeutics. However, the specific protein productivity associated with TGE is significantly lower than stable cell lines. Therefore, the main objective of this study was to increase the specific productivity during transient gene expression in mammalian cells by developing a scaffold, which is suitable for culturing cells as microtissues and provides all the essential microenvironmental factors required for their optimal growth and function. The specific productivity of human embryonic kidney cells (293H), transiently transfected with pNGVL-EGFP plasmid was found to be 5.2-fold higher when cultured in 3D scaffolds than those growing in 2D. This provides a suitable platform for expressing amounts of protein, enough for biomedical research, diagnostics and pre-clinical trials in smaller reactors.

---

[8] Asthana, A., White, C. M., and Kisaalita, W. S. To be submitted to In Vitro Cellular and Developmental Biology - Animal (In Vitro Animal)

APPENDIX C

PROTOCOLS AND METHODS

POLYACRYLAMIDE GEL RECIPE FOR CELL CULTURE

Materials and Reagents:

Glutaraldehyde (25% Solution)

Ammonium Persulfate (APS) (Sigma A3678)

N,N’-Methylenebis(acrylamide) (Sigma 146072)

N,N,N’,N’-Tetramethylethylenediamine (TEMED) (Sigma T9281)

(3-Aminopropyl)trimethoxysilane (3-APTMS) (Sigma 281788)

Sulfo-SANPAH (sulfosuccinimidyl 6-(4’-azido-2’-nitrophenylamino)hexanoate) (Thermo Scientific 22589 or Thermo Scientific A35395)

HEPES Buffer Solution, 1M (gibco by Life Technologies REF 15630-080)

Phosphate Buffered Saline, 1X

Fibronectin, from Bovine plasma (Sigma F1141-1MG)

Rain-X Original Water Repellent

22 mm x 22 mm no. 1.5 glass coverslips (stored in 100% ethanol)

24 mm x 50 mm no. 1.5H glass coverslips

Glass slides

KimWipes

Parafilm

Petri dishes

Equipment:

Vacuum desiccator

UV light (FisherBiotech UV Hand Lamp - 365/254 nm, 115 V, 60 Hz, 0.20 Amps (model FBUVLS-80) or similar product)

Plastic coverslip rack

Forceps

Reagent Setup:

<u>0.5% 3-APTMS in ddH_2O:</u> In 100 mL glass beaker, dilute > 97% stock solution with ddH_2O to a final concentration of 0.5% 3-APTMS in ddH_2O. This should be made fresh each time. This solution can rapidly degrade polycarbonate and polystyrene, especially in concentrated stocks. Concentrated solutions are best handled with glass pipettes and/or measuring vessels. Steps with 3-APTMS should be performed in fume hood. Dispose of 3-APTMS waste in accordance to local safety and waste management guidelines.

<u>0.5% Glutaraldehyde in ddH_2O:</u> In 100 mL glass beaker, dilute 25% (wt/vol) stock solution with ddH_2O to a final concentration of 0.5% glutaraldehyde in ddH_2O. Steps with glutaraldehyde should be performed in fume hood. Dispose of glutaraldehyde waste in accordance to local safety and waste management guidelines.

<u>HEPES, 20 mM, pH 8.5:</u> Dilute 4 mL of 1 M stock HEPES in 196 mL ddH_2O. Add NaOH pellets to bring pH to 8.5 (start with one NaOH pellet). Filter sterilize buffer and store at 4°C for several months.

<u>Bis-acrylamide (2% (wt/vol)):</u> Bis-acrylamide solution can be stored at 4°C for up to 6 months. To make 40 mL of 2% (wt/vol) bis-acrylamide, add 800 mg powder to 40 mL ddH_2O.

APS (10% (wt/vol)): APS should be prepared fresh (Step 9), but it may be used for 72 hours if stored at 4°C or 1 month at -20°C. Freeze-thawing cycles should be avoided. A volume of 1 mL of 10% APS is sufficient for several coverslips. To make 10 mL of 10% (wt/vol) APS, add 1 g powder to 10 mL ddH_2O. Aliquot into smaller tubes and store at -20°C.

Sulfo-SANPAH: !CRITICAL! The reagent is temperature, oxidation, and light sensitive. Thus, always store it as suggested by the supplier and use fresh solutions each time. For large unit size vial (50 mg Thermo Scientific 22589) allow reagent to equilibrate at room temperature then aliquot into amber glass vials in appropriate amounts (1 – 5 mg each). You can backfill amber glass vials with inert gas to prevent moisture exposure. Be sure to work in the dark to prevent exposure of the reagent to light. Store aliquots at -20°C.

Procedure:

Coverslip activation (~ 3 hr)

Step 1: Dry the coverslips by carefully flaming off ethanol.

Step 2: Place the coverslips in a plastic coverslip rack, being careful not to crack the glass.

Step 3: Soak the coverslips in 0.5% 3-APTMS (see Reagent Setup) at room temperature for 30 minutes. Occasional (about every 10 minutes) gentle agitation of the rack in solution will prevent bubble accumulation and ensure even activation.

NOTE: Bubbles cause insufficient coverslip activation, and usually form between the glass coverslips and the plastic rack. If gentle agitation is not enough to prevent bubble accumulation, use forceps to gently remove bubbles from the glass surface.

Step 4: Wash the coverslips by immersing the rack in three changes of ddH_2O. When submerging the rack, be careful not to disturb the coverslips in the rack. They tend to stick together when wet.

Step 5: Following the final wash, gently blot off the bottom of the rack/coverslips with a Kimwipe and dry in an oven (~ 30 minutes, 50°C).

Step 6; Cool the rack/coverslips to room temperature. While cooling, prepare 0.5% glutaraldehyde in ddH_2O (see Reagent Setup).

Step 7: Soak the coverslips in 0.5% glutaraldehyde for 30 minutes at room temperature, again gently agitating to prevent bubble accumulation.

Step 8: Wash the coverslips in three changes of ddH_2O, then allow them to air dry at room temperature on a bench or in the fume hood. Store in a desiccator until needed to prevent deactivation of glass coverslips.

*Pause Point: Activated coverslips can be stored in a rack in a desiccator for up to 2 months.

Polyacrylamide substrate preparation (~ 1 hr)

Step 9: Prepare fresh 10% APS solution (see Reagent Setup).

Step 10: Polish multiple glass slides with Kimwipes and Rain-X solution to make the surface hydrophobic. Polishing both sides is easiest. Rinse well with water and allow them to air-dry. How many slides you polish should depend on the number of gels you are trying to make in a single go.

Step 11: In a 15 mL conical tube, mix acrylamide, bis-acrylamide, and 1X PBS to produce the desired gel stiffness (see Table 1). When choosing the amount of polyacrylamide mixture to prepare, 5 mL will be more than enough for several (6 – 10) coverslips. If you intend on making more coverslips than this, it is advisable to divide the solution into two ~ 2.5 mL portions in separate 15 mL tubes before adding TEMED and APS. The solutions must be made fresh from individual reagents each time.

Step 12: Mix thoroughly by vortexing for 60 seconds.

Step 13: Degas the acrylamide/bis-acrylamide mixture in a vacuum desiccator for 10 minutes (or until the bubbles are gone). Although the relatively high concentrations of APS and TEMED in this protocol make degassing unnecessary, the presence of oxygen is known to create an inhibition period. The most homogenous gels are obtained with the fastest polymerization, so degassing is advised.

Step 14: While the acrylamide/bis-acrylamide mixture is being degassed, place the polished, hydrophobic glass slides out on your bench (I do this step in the fume hood) and place one treated glass coverslip on the edge of the slide to make the next steps as easy as possible.

Step 15: Working quickly, for each 5 mL of acrylamide/bis-acrylamide mixture add 20 µL of TEMED and mix briefly by gentle inversion (~10 inversions). Next, for each 5 mL of acrylamide/bis-acrylamide mixture add 30 µL of APS and mix briefly by gentle inversion (~ 10 inversions).

Step 16: Distribute a 30 µL drop of the mixture onto one of the polished, hydrophobic glass slides. Gently place an activated coverslip onto the drop, ensuring that the drop spreads evenly with no bubbles. Repeat this process for each set of slide/coverslips. NOTE: The polyacrylamide in small-volume solutions will polymerize very rapidly; therefore, the number of coverslips that can be setup in a single go will be limited. When working alone, I do no more than six coverslips at a time. My approach is to distribute a drop of the mixture on two of the polished, hydrophobic glass slides then place the coverslips onto each drop, then repeat for the remaining slide/coverslips. I found this better than distributing all six drops (or however many coverslip gels you want to make) at the same time before placing the coverslips. As mentioned, the solution polymerizes rapidly in small volumes, so by the time I made it to drop # 4, 5, 6, etc. they had already started to polymerize, and the solution wouldn’t spread evenly. If you have a second person available to help, I advise one person to distribute the drops of mixture onto the hydrophobic glass slides, while the other person follows behind with forceps and places the activated coverslips onto the drops of mixture.

Step 17: Allow the acrylamide/bis-acrylamide mixture to polymerize at room temperature (~ 20 minutes). You can monitor the polymerization process by occasionally checking the remaining mixture in the 15 mL tube.

Step 18: After polymerization is complete, flood the surface of the slides and coverslips with 1X PBS.

Step 19: Remove the coverslips from the slides. This can be achieved by either gently lifting up on the coverslip or by first applying gentle lateral pressure to the edge of the coverslip with forceps. Submerge the polyacrylamide side up in fresh 1X PBS in another Petri dish. Repeat for all coverslips (like gels can be placed together in fresh 1X PBS, gel side up). Label the dish with the gel stiffness and/or recipe mixture.

Step 20: Rinse well (three or four exchanges) with 1X PBS to remove unpolymerized acrylamide. Store in 1X PBS.

NOTE: Keep in mind that very soft gels (< 1 kPa) are fragile and should be handled with care during manipulations. Even with appropriate care, soft gels will often display some ruffling at the edges of the coverslip, which is normal.

*Pause Point: Coverslips/gels can be stored in 1X PBS at 4°C for at least 1 week.

<u>Functionalizing the polyacrylamide gel (~ 2 hrs, followed by incubation with ECM solution)</u>

NOTE: From this point on, work in a biosafety cabinet (BSC) to maintain sterility. Take necessary steps to ensure you are working with sterile materials and equipment.

Step 21: Place a piece of Parafilm onto a 100 mm diameter Petri dish bottom. Depending on the number of gels you want to functionalize, multiple Petri dishes can be used. Additionally, place a piece of Parafilm onto a large, 400 mm diameter Petri dish bottom. Expose to UV for 30 minutes to 1 hour to ensure sterility.

Step 22: Polyacrylamide gel sterilization was carried out by exposing the gels to UV light for 10 minutes.

Step 23: Prepare a solution containing an appropriate concentration of ECM molecule, usually 100 µg mL^{-1} in PBS or 20 mM HEPES (pH 8.5). If not used immediately, keep ECM solution at 4°C or on ice. NOTE: I made my Fibronectin solution in 20 mM HEPES (pH 8.5) during Step 31. Whether you use 20 mM HEPES (pH 8.5) or 1X PBS will depend on the ECM molecule.

Step 24: During the sterilization Steps 21 and 22, remove a vial containing an appropriate amount of sulfo-SANPAH from the freezer and allow to equilibrate to room temperature. Be sure sulfo-SANPAH powder is protected from light. DO NOT open sulfo-SANPAH vial until it has reached room temperature to avoid moisture condensation onto the product.

Dissolve sulfo-SANPAH in DMSO to a concentration of 20 mg/mL (40.6 mM). Replace cap and vortex to mix thoroughly. Add appropriate amount of room temperature 20 mM HEPES (pH 8.5) to bring final sulfo-SANPAH concentration to 1 mg/mL (2.03 mM). Vortex to mix. Be sure to keep sulfo-SANPAH solution protected from light.

NOTE: The NHS-ester moiety of sulfo-SANPAH hydrolyzes rapidly and becomes non-reactive. Therefore, it is important that you work quickly during the next steps. If found it most effective to activate all of the acrylamide gels at the same time as opposed to one at a time (cf. Steps 25, 26, and 27).

Step 25: Using forceps, take a gel coverslip and rinse the gel surface with 20 mM HEPES (pH 8.5). Wick off excess buffer with a KimWipe. Do not allow the gel to dry. Place the coverslip on the 100 mm diameter Petri dish/Parafilm sheet (Step 21), gel side facing up. The Parafilm will help prevent the coverslip from sliding during handling and will prevent wicking of the sulfo-SANPAH solution away from the gel surface.

Step 26: Add 200 µL of sulfo-SANPAH to the gel surface.

Step 27: Repeat Steps 25 and 26 for additional gel coverslips.

Step 28: Place UV lamp above gels with sulfo-SANPAH, about 8 cm away from the bulb, for 8 minutes. Sulfo-SANPAH will darken during UV exposure.

Step 29: Rinse gel coverslips in 20 mM HEPES (pH 8.5) (~10 mL per coverslip), then remove excess buffer with KimWipe. Replace coverslips on a Petri dish/Parafilm sheet.

Step 30: Repeat Steps 26 - 28.

Step 31: During the second UV activation step, if you haven’t already, prepare your ECM solution. Ensure the solution is mixed well.

Step 32: Following the second UV activation step, rinse gel coverslips twice in 20 mM HEPES (pH 8.5). The second HEPES solution should have minimal amounts of color from the sulfo-SANPAH. Add another wash step if necessary.

Step 33: Using forceps, place gel coverslips onto Parafilm-lined 400 mm Petri dish, gel side facing up. Distribute 100 - 125 µL of ECM solution onto each gel (enough to sufficiently cover the gel surface).

Step 34: Allow ECM to couple with polyacrylamide for 6 hours at 4°C. Wrapping the Petri dish with Parafilm or incubation in a humidified chamber (Petri dish or other closed container with a damp Kimwipe) will help prevent evaporation of the ECM solution. NOTE: I keep the Petri dish with the polyacrylamide gels on a plate rocker at 4°C to ensure even coating of the gel surface.

Step 35: Using forceps, remove gel coverslips from the Petri dish and place gel side up into sterile PBS in separate plates. Rinse extensively with sterile PBS (three changes of buffer).

Cell deposition on ECM-polyacrylamide gels (~ 2.5 hrs)

Step 36: Before using for cell culture, PBS should be replaced with warm (37°C) cell culture medium. Allow the gels to equilibrate inside an incubator at 37°C for 1 hour before seeding with cells.

Step 37: Wash adherent cells with sterile, warm (37°C) PBS^{--} for 5 minutes.

Step 38: To detach cells, add an appropriate volume of trypsin-EDTA or accutase. Place cells in incubator (37°C) for 10 minutes. To avoid clumping do not agitate the cells by hitting or shaking the dish/flask.

Step 39: Add 6 to 8 mL of cell culture medium to deactivate trypsin-EDTA and centrifuge in a 50 mL centrifuge tube at 200g for 5 minutes. Cell pellet should form at the bottom of the tube.

Step 40: Remove supernatant without disturbing the cell pellet. Add appropriate amount of medium and gently pipette to resuspend the cells. A subcultivation ratio of 1:4 was routine for a 100 mm cell culture dish.

Step 41: A 26,640 cell/mL suspension in cell culture medium should be prepared for the gels.

Step 42: Remove gel coverslips from the cell culture medium and wick excess buffer with a KimWipe. Place gel coverslips gel side facing up onto a UV-sterilized Petri dish/Parafilm sheet. Add 300 µL of cell solution (5,000 cells per gel) directly to the gel surface. The Parafilm sheet will prevent wicking of the cell solution from the gel surface. Repeat for additional gel coverslips.

Step 43: Place gels with cells in incubator (37°C) for 3 hours to allow cell adhesion to the gel surface. Check adhesion at the 3-hour mark. Top off each plate with cell culture medium.

Acrylamide	Bis-acrylamide	1X PBS--	TEMED / APS	Total Volume	Young's modulus
5% / 625 µL	0.3% / 750 µL	3.625 mL	20 µL / 30 µL	5 mL	~ 25 kPa
5% / 625 µL	0.15% / 375 µL	4 mL	20 µL / 30 µL	5 mL	~ 10.5 kPa
5% / 625 µL	0.075% / 187.5 µL	4.1875 mL	20 µL / 30 µL	5 mL	~ 3.6 kPa
3% / 375 µL	0.3% / 750 µL	3.875 mL	20 µL / 30 µL	5 mL	~ 1.9 kPa
3% / 375 µL	0.15% / 375 µL	4.25 mL	20 µL / 30 µL	5 mL	~ 0.4 kPa

Table 1: Acrylamide mixtures and an approximate Young's modulus, measure by atomic force microscopy

PROTOCOL FOR CREATING MICROWELLS IN 6-WELL PLATE FORMAT FOR CELL CULTURE VIA PHOTOLITHOGRAPHY, SOFT LITHOGRAPHY, AND HOT EMBOSSING

Materials and Reagents:

SU-8 2150

SU-8 2002

PDMS (Sylgard 184; Dow Corning Co.)

Silanizing reagent (Chlorotrimethylsilane, 98%; Alfa Aesar A13651)

Polystyrene sheet (evergreen scale models sheet styrene; 0.4mm thick)

Binder/paper clips (black, medium size)

Glass slides

Phosphate buffer saline, 1X (PBS)

Fibronectin, from Bovine plasma (Sigma F1141, 1MG)

Cell culture medium

Equipment:

Oven

Plasma Cleaner PDC-32G (HARRICK PLASMA) or similar product

Vacuum desiccator

Procedure:

Pattern Design

Many computer-aided design (CAD) software programs are available to design your desired pattern (Autodesk AutoCAD, DesignCAD, Adobe Freehand, Illustrator).

Fabrication of Mask

High-resolution printing provides a simple and convenient method for fabricating photomasks on transparent film.

CAD/ART services are commonly used to create high-quality masks (I’ve used the CAD/ART services from outputcity.com before and have been happy with their product).

Be sure to work with a service representative while designing your mask. Some services will not guarantee accuracy of features smaller than 20 µm.

For higher resolutions down to 1 µm (or even submicron), chrome photomasks are typically required, but will also be more expensive.

Fabrication of SU-8 master (photolithography)

At UGA, photolithography is conducted in the clean room located in Riverbend Research South. (NOTE: An extensive training period is required before access to the clean room is granted)

Listed below is a general approach to creating a PDMS master via photolithography. The details of these steps will vary and need to be optimized with respect to your design and the available equipment.

- SU-8 photoresist spincoated on a silicon wafer to the desired film thickness
- SU-8 photoresist pre-baked
- Transparent photomask with desired pattern staged and SU-8 photoresist exposed to UV light
- Post-baking
- Developed in propylene glycol monomethyl ether acetate

Silanization of SU-8/Silicon Master

This process will passivate the surface of the SU-8/Silicon wafer master mold to aid the release of PDMS and prevent the PDMS from sticking to the master. This step is required for a newly fabricated master. Silanized master molds can be used to make multiple copies of PDMS molds (at least 10 copies) without additional surface treatment.

Step 1: Remove any debris from the SU-8/Silicon master using pressurized Nitrogen.

Step 2: Inside a **chemical fume hood**, add two drops (using plastic pipette) of the silanizing reagent (e.g., Chlorotrimethylsilane) onto the Silicon wafer but away from the SU-8 features.

Step 3: Cover your Silicon wafer (I had the wafer in a 400 mm diameter Petri dish) and place it in a vacuum desiccator to force the silanes to form a monolayer on the surface of the master. Keep under vacuum for 30 minutes.

Step 4 (optional): If excessive silane is present, place the wafer on a hotplate set at 150°C for 10 minutes to evaporate the excess silane.

Fabrication of PDMS Master (soft lithography)

Step 1: Pre-heat oven to 65°C

Step 2: PDMS to a weight ratio of 10:1 base to curing agent (e.g., 10 g base + 1 g curing agent)

Step 3: Mix vigorously with spatula so that numerous bubbles can be seen in the mixture

Step 4: Place PDMS mixture in vacuum desiccator to degas (approx. 10 minutes)

Step 5: Cast PDMS mixture onto SU-8/Silicon master to desired thickness (my masters came out 8 - 10 mm thick). To prevent the PDMS from running everywhere, I took the bottom of a 100 mm Petri dish, cut a hole, and poured the PDMS prepolymer through the hole. The 100 mm Petri dish was weighed down with a block (or any other small weight available) to prevent the PDMS prepolymer from running out of the 100 mm Petri dish.

Step 6: Degas again to ensure no air bubbles remain trapped at the interface between the SU-8 and the PDMS prepolymer.

Step 7: Place in oven and bake for 2 hours. The curing process is faster with higher temperature.

Step 8: With remaining PDMS mixture and a punch in one hand, cast PDMS in a 35 mm Petri dish around the punch. The idea is to create a 35 mm diameter PDMS ring. Place in oven with the other PDMS mold and bake for 2 hours.

Step 8: After curing is complete, allow the PDMS to cool to room temperature before carefully peeling away the PDMS.

Step 9: With the PDMS "negative" master mold and the PDMS ring in hand, apply PDMS to the bottom of the ring and place it on top of the PDMS mold. Make sure you attach the ring to the same face as the PDMS "negative" features.

Step 10: Bake at 65°C for 2 hours

Step 11: Trim the excess PDMS from the base of your new PDMS Master.

<u>PDMS - PDMS molding</u>

Step 1: Using the Plasma Cleaner PDC-32G set on the Medium setting, expose PDMS master to oxygen plasma for 20 seconds. Remove from the Plasma Cleaner and place in Petri dish. (The purpose of this process is to give hydroxyl groups to PDMS, then the amines in the silane will bond to the PDMS more readily)

Step 2: Working quickly, add 50 µL chlorotrimethylsilane (using a plastic pipette) to the PDMS master, cover, and place under vacuum for 10 minutes.

Step 3: Once the chlorotrimethylsilane has evaporated, place PDMS master in oven at 65°C for 1 hour.

Step 4: Mix the PDMS prepolymer to a base : curing agent ratio of 5:1.

Step 5: Pour the PDMS prepolymer into the PDMS master mold and place under vacuum for 10 minutes to degas the PDMS prepolymer. This will ensure all air bubbles are eliminated from the interface between the PDMS mold and the PDMS prepolymer.

Step 6: Cure the PDMS prepolymer at 65°C for 1 hour. The curing time at this step is cut in half because it was found that this is the best amount of time to ensure partial curing of the PDMS prepolymer but also minimize the spontaneous adhesive interaction between the liquid PDMS prepolymer and the PDMS master mold.

Step 7: After curing the liquid PDMS prepolymer for 1 hour, remove from the oven and carefully peel the two PDMS piece apart. Place the newly formed PDMS stamp back in the oven for an additional 1 hour at 65°C to complete the polymerization.

Hot embossing Polystyrene with PDMS stamp

Step 1: Preheat oven to 115°C

Step 2: Cut your Polystyrene sheet (evergreen scale models sheet styrene; 0.4 mm thick) to size

Step 2: Sandwich PDMS stamp and Polystyrene sheet between glass slides using binder clips. Be sure the features on the PDMS stamp are facing the Polystyrene sheet.

Step 3: Bake for 15 minutes at 115°C

Step 4: Remove from oven and allow to cool to room temperature before removing binder clips.

Microwell 6-well plate format

Step 1: Preheat oven to 260°C (melting point for Polystyrene 210 - 249°C) and place metal punch in oven

Step 2: Preheat hot plate to 80°C (glass transition temperature for Polystyrene is 100°C)

NOTE: The goal of Steps 1 and 2 is to heat the punch to a very high temperature and the hot plate to a temperature just below the glass transition temperature.

Step 3: When the punch is heated sufficiently, place the 6-well plate on the hot plate to warm, about 1 minute

Step 4: With heat-resistant oven gloves, remove the metal punch from the oven and apply pressure in the center of one of the 6-well plate. The punch should easily press through the Polystyrene plate.

NOTE: The metal punch will cool quickly. I only punch one well at a time and reheat the punch in-between each well.

Step 5: After punching a hole in each well of your 6-well plate and embossing your microwell pattern into PS sheets, place one PS sheet in each well and align the sheet over the punched hole. We will “chemically weld” the PS sheet to the PS 6-well plate using a solvent (i.e., chloroform).

Step 6: Using a glass pipette and working in a chemical fume hood, carefully apply a few chloroform drops around the PS sheet so the chloroform “welds” the edges of the PS sheet to the underlying PS 6-well plate. Be careful not to drop any chloroform directly onto your PS sheet, as this will ruin your embossed microwell features. Apply pressure to the PS sheet to ensure no air bubble form at the PS sheet/6-well plate interface.

Step 7: Allow a few hours for the chloroform to evaporate. Repeat Step 6 as many times as necessary to completely weld the PS sheet/6-well plate interface.

Step 8: Once the chemical welding process for all 6 wells is complete, mix PDMS base and curing agent to a 10:1 ratio. Degas the mixture to remove air bubbles.

Step 9: For this step, we will create a 10 mm diameter well in PDMS. Using a tube, punch, or anything else that can stand upright and has the desired diameter, place upright on top of the PS sheet and pour PDMS prepolymer around the tube to a thickness of 12 mm.

Step 10: Cure PDMS prepolymer at 65°C for 2 hours.

Step 11: Carefully remove tube and peel away any PDMS that might have leaked under the tube. You should be left with a 10 mm diameter well in PDMS within each 6-well plate.

Preparation for cell culture

Step 1: IPA sterilization (30 minutes)

Step 2: UV sterilization in biosafety cabinet overnight

Step 3: Functionalize PS microwells with fibronectin solution (7.5 µg in 250 µL PBS) overnight at 4°C

Step 4: Rinse with 1 mL PBS (x2)

Step 5: Add 1 mL cell culture medium and allow to incubate at 37°C for 1 hour

Step 6: Add desired number of cells suspended in 1 mL cell culture medium

Step 7: Centrifuge for 5 minutes at 200g to force cells down into microwells

Step 8: Allow 3 - 6 hours for cells to attach, then top off with cell culture medium